IPC 2025

6th International Symposium & Workshops POLYMERIC composites

2-4 OCTOBER/EKİM 2025

6th INTERNATIONAL POLYMERIC COMPOSITES SYMPOSIUM AND WORKSHOPS

VI. ULUSLARARASI POLİMERİK KOMPOZİTLER SEMPOZYUMU VE ÇALIŞTAYLARI

IPC 2025
PROCEEDINGS BOOK
BİLDİRİLER KİTABI

TMMOB
KİMYA MÜHENDİSLERİ ODASI
UCTEA CHAMBER OF CHEMICAL ENGINEERS

KOMPOZİT SANAYİCİLERİ DERNEĞİ
TURKISH COMPOSITES MANUFACTURERS ASSOCIATION

İZMİR-TÜRKİYE
www.polymericcomposites.org

This book is published by
UCTEA Chamber of Chemical Engineers

Bu kitap
TMMOB Kimya Mühendisleri Odası
tarafından yayınlanmıştır.

2-4 October 2025

2-4 Ekim 2025

Preparation / Hazırlama
Hüsnü Onur ERTÜRK
Kamil YEŞİL

Editors / Editörler
Dr. Yahya Kara
Prof. Dr. Metin Tanoğlu
Prof. Dr. Özgür Seydibeyoğlu

UCTEA Chamber of Chemical Engineers Aegean Branch TMMOB
TMMOB Kimya Mühendisleri Odası Ege Bölge Şubesi

ACKNOWLEDGMENT

We would like to extend our deepest gratitude to all those who contributed to the successful organization and realization of IPC 2025.

First and foremost, we express our sincere appreciation to **Prof. Dr. Gürel Nişli**, who chaired the first five editions of our symposium with great dedication and played a leading role in institutionalizing this event.

We are also grateful to **Mr. İbrahim Köse**, our symposium coordinator, for his crucial role in ensuring the smooth progress of the organization; to our esteemed co-chairs, **Prof. Dr. Metin Tanoğlu** and **Prof. Dr. Özgür Seydibeyoğlu**, for their invaluable contributions to the scientific foundation of the symposium and for serving as editors of this book; to **Dr. Yahya Kara** for his devoted efforts within the organizing committee and editorial team; and to **Prof. Dr. Mustafa Demircioğlu** for his valuable support throughout the process.

We also express our sincere gratitude to the Turkish Composites Manufacturers Association, which, with its cooperation and support, stood by us in the realization of the sixth edition of this symposium of great importance to our country and the Turkish industry, and to its representative and our executive committee member **Mr. Serhat Karabağ**. Special thanks also go to our Aegean Branch Executive Committee members **Ms. Sezen Çıngır** and **Mr. Cem Aynalı** for their contributions to the implementation of the event, to all supporting institutions, sponsoring companies, and to all members of the Executive, Organizing, and Scientific Committees who are integral parts of the symposium.

Finally, we would like to give special thanks to **Onur Aşkaroğlu, Hüsnü Onur Ertürk, and Sümeyra Göçemen** for their devoted work in managing the symposium secretariat.

UCTEA Chamber of Chemical Engineers

TEŞEKKÜR

IPC 2025'in başarıyla düzenlenip gerçekleştirilmesinde emeği geçen tüm değerli katkı sahiplerine en içten teşekkürlerimizi sunarız.

Öncelikle, başkanlığını büyük bir özveriyle üstlenerek etkinliğimizin kurumsallaşmasına öncülük eden **Prof. Dr. Gürel Nişli**'ye şükranlarımızı sunarız.

Sempozyumun koordinasyonunu üstlenerek sürecin sağlıklı ilerlemesinde büyük rol oynayan **Sayın İbrahim Köse**'ye, sempozyumun bilimsel altyapısının oluşturulmasına katkıda bulunan ve bu kitabın editörlüğünü üstlenen değerli sempozyum eş başkanlarımız **Prof. Dr. Metin Tanoğlu** ve **Prof. Dr. Özgür Seydibeyoğlu**'na, yürütme kurulu ve kitap editörlüğündeki özverili çalışmaları için **Dr. Yahya Kara**'ya, ayrıca süreç boyunca sağladığı değerli destekleri için **Prof. Dr. Mustafa Demircioğlu**'na teşekkür ederiz.

Ülkemiz ve Türk sanayisi için büyük önem taşıyan bu sempozyumun altıncısının gerçekleştirilmesinde iş birliği ve destekleriyle yanımızda olan **Kompozit Sanayicileri Derneği'**ne ve temsilcisi, yürütme kurulu üyemiz sayın **Serhat Karabağ**'a, ayrıca etkinliğin hayata geçirilmesinde görev alan Ege Bölge Şube Yürütme Kurulu Üyelerimiz sayın **Sezen Çıngır** ve sayın **Cem Aynalı**'ya , katkıda bulunan tüm destekleyici kurumlara, sponsor firmalara ve sempozyumun tüm bileşenleri olan Yürütme, Düzenleme ve Bilim Kurulu üyelerine gönülden teşekkür ederiz.
Son olarak, sempozyum sekretaryasını büyük bir özveriyle yürüten **Onur Aşkaroğlu, Hüsnü Onur Ertürk ve Sümeyra Göçemen**'e özel teşekkürlerimizi sunarız.

TMMOB Kimya Mühendisleri Odası

FOREWORD

The 6th International Polymeric Composites Symposium and Workshops (IPC 2025) was held on 2–4 October 2025 at the İzmir Tepekule Congress and Exhibition Center. We are delighted to have contributed to this significant event, which showcased the latest innovations in the production, development, and industrial applications of composite materials.

As one of the largest organizations in its field in our country, the symposium received a substantial number of abstract submissions and participation applications from numerous national and international universities, research centers, public institutions, and private organizations.

Organized this year under the main theme "***Future in Composite Materials: Sustainable, High-Performance, and Digitally-Driven Applications***," IPC 2025 provided a unique platform for following recent scientific and technological advancements in the field of composites, strengthening collaboration between academia and industry, exchanging ideas with leading experts, showcasing innovative products, and creating new opportunities for cooperation.

We are also pleased to present the Abstracts Book of IPC 2025 and would like to express our sincere gratitude to all contributors, particularly the authors, reviewers, and members of the editorial board for their valuable efforts and support.

In addition to the Proceedings Book, selected papers were published in the ***Springer Proceedings in Materials series under the title Future in Composite Materials: Sustainable, High-Performance, Digitally-Driven Applications***, adding further value and international visibility to the symposium.

Finally, we would like to extend our heartfelt thanks to all members of the Organizing Committee, Scientific Committee and all supporting members whose dedication, commitment, and continuous efforts made this event possible.

Sincerely, on behalf of the IPC 2025 Executive Committee…

Symposium Chairs and Book Editors

Prof. Dr. Metin Tanoğlu
Izmir Institute of Technology

Prof. Dr. Özgür Seydibeyoğlu
Izmir Katip Çelebi University

Dr. Yahya Kara (Book Editor)
Luxembourg Institute of Science and Technology

İbrahim Köse
Symposium Coordinator

ÖNSÖZ

6. Uluslararası Polimerik Kompozitler Sempozyumu ve Çalıştayları (IPC 2025) 2 - 4 Ekim 2025 tarihleri arasında İzmir Tepekule Kongre ve Sergi Merkezi'nde gerçekleşmiştir.

Kompozit malzemelerin üretimi, geliştirilmesi ve endüstriyel uygulamalarındaki yenilikleri sergilemek üzere katkı vermiş olmakdan büyük mutluluk duyuyoruz.

Ülkemizde alanındaki en büyük organizasyonlardan biri olan sempozyumda ulusal ve uluslararası birçok üniversite, araştırma merkezi, resmi ve özel kuruluşlardan önemli sayıda Bildiri Özeti ve Katılım Başvurusu almış olmaktan memnun olduk.

Bu yıl "***Kompozit Malzemelerde Gelecek: Sürdürülebilir, Yüksek Performanslı ve Dijital Odaklı Uygulamalar***" ana teması ile gerçekleşen olan IPC 2025; kompozit alanında bilimsel ve teknolojik gelişmeleri takip edebilmek, akademi ve sanayi arasındaki bağı güçlendirmek, alanında uzmanlar ile fikir alışverişinde bulunmak, kompozit alanında ürünleri sergilemek ve iş birliği fırsatlarını geliştirmek için eşsiz bir platform sunmuştur.

IPC 2025 kapsamında Bildiri Özetleri Kitabını yayınlamaktanda memnuniyetimizi bildirir, emeği geçen başta bildiri sahibi yazarlar, değerlendirici hakemler ve yayın kurul üyeleri olmak üzere teşekkürlerimizi sunarız.

Bildiriler Kitabına ilave olarak seçilmiş bildirilerin Springer Proceedings in Materials serisinde `**Future in Composite Materials: Sustainable, High-Performance, Digitally-Driven Applications**` başlıklı bir kitap olarak da yayınlanması ayrı bir değer oluşturmuştur.

Bu etkinliğin hayata geçirilmesi için emeğini esirgemeyen, özveri ve gayretle desteğini her zaman sunan başta Düzenleme Kurulu olmak üzere tüm Sempozyum Kurul Üyelerine ve çalışma ekiplerine gönülden teşekkür ederiz.

Saygılarımızla

IPC 2025 Düzenleme Kurulu adına…

Sempozyum Başkanları ve Kitap Editörleri

Prof. Dr. Metin Tanoğlu
İzmir Yüksek Teknoloji Enstitüsü

Prof. Dr. Özgür Seydibeyoğlu
İzmir Katip Çelebi Üniversitesi

Dr. Yahya Kara (Kitap Editörü)
Lüksemburg Bilim ve Teknoloji Enstitüsü

İbrahim Köse
Sempozyum Koordinatörü

SUPPORTING INSTITUTIONS / *DESTEK VEREN KURULUŞLAR*

Official Institutions / *Resmi Kuruluşlar*

Aegean Region of Industry / Ege Bölge Sanayi Odası

Izmir Chamber of Commerce / İzmir Ticaret Odası

Izmir Katip Çelebi University / Katip Çelebi Üniversitesi

Izmir Institute of Technology / İzmir Yüksek Teknoloji Enstitüsü

Ege University / Ege Üniversitesi

Union Of Chambers Of Turkish Engineers and Architects / TMMOB

Uctea Chamber Of Mechanical Engineers / Makina Mühendisleri Odası

ESİAD Aegean Industry and Business Association / Ege Sanayi İş İnsanları Derneği

ENSİA Energy Industrialists and Business Association / Enerji Sanayicileri ve İş İnsanları Derneği

BUTEKOM Bursa Technology and Coordination R&D Center /Bursa Teknoloji Koordinasyon ve AR&GE Merkezi

HUKD Aerospace Cluster Association / Havacılık ve Uzay Kümelenmesi Derneği

COMMERCIAL SPONSORS / *TİCARİ SPONSORLAR*

Company Name /*Firma Adı*	Sponsorship Type / *Sponsorluk Türü*
Polkima Grup Şirketler Polyester Kimya ve Makina San. ve Tic. A.Ş. Polmar Kompozit A.Ş.	Gold Sponsor / *Altın Sponsor*
Poliya Poliester San. ve Tic. A.Ş.	Gold Sponsor / *Altın Sponsor*
Akpa Kimya San. ve Tic. A.Ş.	Silver Sponsor / *Gümüş Sponsor*
Boytek Reçine Boya ve Kimya San. Tic. A.Ş.	Silver Sponsor / *Gümüş Sponsor*
Fiberr Fiber Reinforced Resins A.Ş.	Silver Sponsor / *Gümüş Sponsor*
Polütek Polyester Poliüretan Ltd. Şti.	Silver Sponsor / *Gümüş Sponsor*
Turkuaz Polyester Reçine Kimya San. Tic. A.Ş.	Silver Sponsor / *Gümüş Sponsor*
Duratek Koruyucu Malzemeler San. ve Tic. A.Ş	Bronze Sponsor / *Bronz Sponsor*
Kosse Kompozit Pazarlama ve Müh. San. Tic. Ltd. Şti.	Bag Sponsorship / *Çanta Sponsorluğu*
Literatur Kimya Elek. İnş. Taah. Turz. ve Oto İth. İhr. San. Tic. Ltd. Şti.	Name Badge Sponsorship / *Yaka Kartı Sponsorluğu*
Omnis Kompozit San. Ve Tic. Ltd. Sti.	Bronze Sponsor / *Bronz Sponsor*
Polmod Makine Model Kalıp Plastik Ürünler San. Tic. A.Ş.	Invited Speaker Sponsorship / *Çağrılı Konuşmacı Sponsorluğu*
Senko Sanayi Ürünleri Ltd. Şti.	Bronze Sponsor / *Bronz Sponsor*

Tezkom Kompozit Teknolojileri San. ve Tic. A.Ş.	Bronze Sponsor / *Bronz Sponsor*
Yücel Kompozit Malzemeleri Pazarlama ve Ticaret A.Ş.	Bronze Sponsor / *Bronz Sponsor*
Anamed Analitik ve Medikal Sistemler A.Ş.	Abstract Booklet Sponsorship / *Özet Kitapçığı Sponsorluğu*
Bilge Çiftliği Gıda Ürünleri San. ve Tic Ltd. Şti.	Coffee Break Sponsor / *Çay-Kahve Arası Sponsorluğu*
Nanopol Kimya Kompozit ve Boya San. Tic. Ltd. Şti.	Notebook and Pen Sponsorship / *Bloknot ve Kalem Sponsorluğu*
Pul-tech FRP Kompozit Yapı Teknolojileri İmalat Sanayi ve Ticaret A.Ş.	Abstract Booklet Sponsorship / *Özet Kitapçığı Sponsorluğu*
Tila Composite Representation Domestic and Foreign Trade Ltd. Şti.	Invited Speaker Sponsorship / *Çağrılı Konuşmacı Sponsorluğu*

EXECUTIVE COMMITTEE / *YÜRÜTME KURULU*

İbrahim Köse, Chemist	Kosse Composite Marketing - General Coordinator
Metin Tanoğlu, Prof. Dr.	Izmir Institute of Technology – Symposium Co-Chair
Özgür Seydibeyoğlu, Prof. Dr	Izmir Katip Celebi University – Symposium Co-Chair
Sezen Çıngır, Chemical Engineer	UCTEA Chamber of Chemical Engineers – Executive Committee Member
Serhat Karabağ, Civil Engineer	Turkish Composites Manufacturers Association – Executive Committee Member
Yahya Kara, Dr.	Luxembourg Institute of Science and Technology – Executive Committee Member
Cem Aynalı, Chemical Engineer	UCTEA Chamber of Chemical Engineers – Executive Committee Member

SECRETARIAT / *SEKRETERYA*

Onur Aşkaroğlu	UCTEA Chamber of Chemical Engineers
Sümeyra Göçemen	Kosse Composite Marketing
Hüsnü Onur Ertürk	Izmir Katip Celebi University

INVITED SPEAKERS / DAVETLİ KONUŞMACILAR

Salim Belouettar, Dr.	Luxembourg Institute of Science and Technology
Marino Quaresimin, Prof. Dr.	University of Padova
Micheal Wisnom, Prof. Dr.	University of Bristol
Jozsef Gabor Kovacs, Assoc. Prof.	Budapest University of Technology and Economics
Mete Bakır, Dr.	Turkish Aerospace Industries

ORGANIZING COMMITTEE / *DÜZENLEME KURULU*

Ahmet Ünal, Prof. Dr.	Yıldız Technical University
Ali Birtan Erdoğan	ERCO- ECE Paint Chemistry Industry and Trade Inc.
Alper Kalaycı	ENSİA (Energy Industrialists & Businessmen Association) - Chairman of the Board
Alperen Doğru, Dr.	Ege University
Aref Cevahir, Dr.	Izmir Institute of Technology.
Aslı Ilgaz	Metyx Composites - Telateks Inc.
Ayhan Ezdeşir	Petkim Petrochemical Holding Inc.
Aylin Ziylan, Prof. Dr.	Dokuz Eylül University
Ayşen Ömer	Herkim Polymer Chemistry Industry and Trade Inc.
Banu Bilge	Fibrosan CTP Industry and Trade Inc.
Beril Darcan	Boytek Resin Paint and Chemistry Industry Trade Inc.

Beyhan Erdoğan	DYO Paint Factories Industry and Trade Inc.
Burak Darcan	Tila Composite Representation Domestic and Foreign Trade Ltd. Co.
Cem Gürkan	Poliya Polyester Industry and Trade Ltd. Co.
Cihangir Cebeci	Fiberr Fiber Reinforced Resins Inc.
Devrim Özaydın	Sabancı University
Erkan Ersöz	Ege University
Erkan Günindi	Olgun Çelik Industry and Trade Inc.
Göksenin Çömlekçi	Türkiye Şişe ve Cam Factories Inc.
İbrahim Akyürek	UCTEA Chamber of Chemical Engineers
Kadir Uçar	ESAS Aegean Defense Industry Aviation and Space Clustering Association
Levent Arslan	KOSGEB İzmir Provincial Directorate
Levent Aydın, Assoc. Prof.	Izmir Katip Çelebi University
M. Cengiz Altan, Prof. Dr.	University of Oklahoma - United States of America
Mehmet Güneş	TUBITAK Marmara Research Center
Mehmet Karahan, Prof. Dr.	Bursa Uludag University
Mehmet Sarıkanat, Assoc. Prof.	Ege University
Mertcan Aslıtürk	Polkima Polyester Chemistry and Machinery Industry and Trade Inc.
Mustafa Demircioğlu, Prof. Dr.	Ege University
Nurseli Uyanık, Prof. Dr.	Istanbul Technical University
Özgür Sönmez	Literatür Chemistry Electrical Construction Contracting Tourism and Automotive Import Export Industry Trade Ltd. Co.
Semih Yiğit	Ostim Defense and Aviation Cluster
Sevim Özgül, Dr.	Bahçeşehir University

Şekib Avdagiç	Istanbul Chamber of Commerce
Ummuhan Topal	DowAksa Advanced Composite Materials Industry Ltd. Co.
Ülkü Yılmazer, Prof. Dr.	Middle East Technical University
Volkan Eskizeybek	18 March University
Yalçın Yılmazkaya	HUKD Aviation and Space Clustering Association
Zeynep Yılmaz Serçinoğlu Dr.	Marmara University

SCIENTIFIC ADVISORY COMMITTEE/ BİLİMSEL ve TEKNİK DANIŞMA KURULU

Ali Gizli, Dr.	DYO Paint Factories Industry and Trade Inc.
Alperen Doğru, Dr.	Ege University
Barış Çağlar, Dr.	Delft University of Technology - Netherlands
Bedriye Üçpınar Durmaz, Dr.	Ege University
Burcu Saner Okan, Assoc. Prof.	Sabancı University
Cem Gök, Prof. Dr.	Bakırcay University
Cemal Basaran, Prof. Dr.	University at Buffalo - United States of America
Cevdet Kaynak, Prof. Dr.	Middle East Technical University
Çağrı Ayrancı, Prof. Dr	University of Alberta - Canada
Devrim Balköse, Prof. Dr.	Izmir Institute of Technology
Dipa Roy,Prof. Dr.	The University of Edinburgh - Scotland
Elif Alyamaç Seydibeyoğlu, Assoc. Prof.	Ege University
Erdem Yücel	Fibrosan CTP Industry and Trade Inc.

Ersan Kalafatoğlu, Prof. Dr.	Marmara University
Ferrie Van Hattum , Prof.Dr.	Saxion University of Applied Sciences - Netherlands
Figen Aynalı, Dr.	Chamber of Chemical Engineers
Funda Tıhmınlıoğlu,Prof. Dr.	Izmir Institute of Technology
Hasan Ömer	Herkim Polymer Chemistry Industry and Trade Inc.
He Haijun, Dr.	College of Textile Science and Engineering, Jiangnan University - China
Holger Seidlitz, Prof. Dr.	Brandenburg University of Technology Cottbus - Germany
Hülya Cebeci,Assoc. Prof.	Istanbul Technical University
İbrahim Köse	Kosse Composite Marketing
İsmail Darcan	Boytek Resin Paint and Chemistry Industry Trade Inc.
Jozsef Gabor Kovacs, Assoc. Prof.	The Budapest University of Technology and Economics - Hungary
Kristiina Oksman, Prof. Dr.	Luleå University of Technology - Sweden
M. Cengiz Altan, Prof. Dr.	The University of Oklahoma - United States of America
Maya John, Dr.	Council for Scientific and Industrial Research (CSIR) - South Africa
Mehmet Sarıkanat, Assoc. Prof.	Ege University
Mehmet Yıldız, Prof. Dr.	Sabancı University
Metin Tanoğlu, Prof. Dr.	Izmir Institute of Technology
Mustafa M. Demir, Prof. Dr.	Izmir Institute of Technology
Nikhil Verghese, Dr.	Sabic - United States of America
Nilay Gizli, Assoc. Prof.	Ege University

Özgür Seydibeyoğlu, Prof. Dr.	Izmir Katip Celebi University
Sadık Aslıtürk	Polkima Polyester Chemistry and Machinery Industry and Trade Inc.
Salim Belouettar, Dr.	Luxembourg Institute of Science and Technology - Luxembourg
Selim Küsefoğlu, Prof. Dr.	Bogazici University
Serkan Dehneliler	Turkish Aerospace Industries (TUSAŞ)
Sevim Özgül, Dr.	Bahcesehir University
Shahid Ur Rahman	Beşler Glassfiber Industry and Trade Inc.
Steve Nutt, Prof. Dr.	University of Southern California - United States of America
Tülay Bal Demirci, Prof. Dr.	Istanbul University - Cerrahpaşa University
Ülkü Yılmazer, Prof. Dr.	Middle East Technical University
Ümit Halis ERDOĞAN, Prof. Dr.	Dokuz Eylul University
Veli Deniz, Prof. Dr.	UCTEA Chamber of Chemical Engineers
Volkan Acar, Dr.	Atatürk University
Yusuf Menceloğlu, Prof. Dr.	Sabancı University
Engin Aktaş, Prof. Dr	Izmir Institute of Technology
Rasim İpek, Prof. Dr.	Ege University

HONORARY COMMITTEE/ ONUR KURULU

Gürel Nişli, Prof. Dr.	Ege University, UCTEA Chamber of Chemical Engineers
İsmail Darcan	Boytek Resin Paint and Chemical Industry Trade Inc.
Hasan Ömer	Herkim Polymer Chemical Industry and Trade Inc.
Fikret Tacar	Tacar Boat
Fersen Kınayyiğit	Glass Fiber Industry Inc.

TABLE OF CONTENTS

Table of Proceedings

PROCEEDINGS

PVC-Based Composite Materials Reinforced with Natural Hemp Fibers

Eren Karakuş[1[0009-0002-6432-1666]], Şükrü Al[1[0009-0008-6067-9584]], Canan Uraz[1[0000-0002-9072-1420]], Nazmiye Yoldaş[2[0000-0001-8162-1092]], Didem Kale[2[0000-0003-1096-6733]], Yunus Emre Dağıstanlı[2[0009-0003-0777-3719]]

[1] Department of Chemical Engineering, Ege University, 35100 Bornova/Izmir, Türkiye
[2] Menemen Plastic Organized Industrial Zone, EGE-PROFİL, 35660 Menemen/Izmir, Türkiye

erenkarakus63@gmail.com

Abstract. Polyvinyl chloride (PVC) is a widely used thermoplastic in products such as piping, window frames, and insulation materials. Despite its versatility, PVC depends on fossil fuels, contributes to greenhouse gas emissions, and has low biodegradability. Incorporating natural fibers into PVC can mitigate these issues while enhancing mechanical performance. Hemp fiber, known for its high tensile strength and Young's modulus, degrades above 200 °C, making PVC—processed at lower temperatures—suitable for composite production. A key limitation of hemp fiber is its hydrophilic nature, which reduces compatibility with hydrophobic PVC. Chemical treatments can improve fiber–matrix adhesion by reducing hydrophilicity. In this study, alkali treatment was applied using NaOH solutions (0–12 wt%) at a 40:1 liquor ratio, 30 °C for 4 h, followed by neutralization with dilute acetic acid, rinsing, and drying. FTIR analysis determined 8.5% NaOH as optimal for maximum hydroxyl group reduction, while SEM-EDS analysis showed significant changes in surface morphology. The treated hemp fibers were incorporated into PVC at weight ratios of 1%, 2%, 3% 4%, 5% and 6%, and processed in a plastograph at 180 °C for 10 min. Tensile impact tests revealed that 3% hemp fiber content achieved approximately 41.5% higher strength compared to pure PVC. These results indicate that optimized alkali treatment and appropriate fiber loading can enhance the mechanical properties of PVC composites while potentially reducing their environmental impact.

Keywords: Hemp fiber, Alkaline treatment, Fiber- polymer compatibility.

Introduction

Polyvinyl chloride (PVC), synthesized from vinyl chloride monomers, is the third most produced thermoplastic after polyethylene and polypropylene. Naturally rigid and brittle, it attains flexibility and wider industrial applicability through the addition of plasticizers. [1].

PVC is a thermoplastic characterized by low thermal stability, which restricts its utilization in industries operating at elevated temperatures. In its neat form, PVC exhibits brittleness and lack of flexibility, resulting in limited commercial applicability. Consequently, prior to practical application, PVC must be compounded with appropriate additives to enhance its performance and stability [2].

PVC is prone to degradation at high temperatures, releasing hydrochloric acid. To prevent this, stabilizers are added, which neutralize the acid and slow oxidation [3]. Tin-based stabilizers are especially effective, improving the thermal stability of both rigid and flexible PVC, preserving color, and enhancing resistance to heat, oxygen, and UV radiation [4].

Temperature limits biodegradable composite production because natural fibers cannot tolerate high processing heat. PVC, widely used in automotive, housing, and construction, is increasingly combined with natural fibers due to lower environmental impact, reduced waste, and advantages like low cost, light weight, and good insulation. Its low processing temperature makes PVC suitable for blending with natural fibers to produce partially biodegradable composites [5]. This combination is viewed as promising because using PVC with eco-friendly natural fibers reduces environmental impact. The growing global interest in natural fiber-based composites is attributed to their biodegradability, renewability, recyclability, abundant availability, competitive mechanical properties, reduced energy consumption, and minimum waste disposal problems [6]. Incorporating natural fibers into thermoplastic composites has been shown to enhance the elastic modulus of the material, although it may lead to a reduction in impact strength [7]. These factors collectively support the suitability of PVC as a matrix material for developing biodegradable natural fiber composites.

Hemp fiber is regarded as one of the most promising natural fibers for making PVC composites due to its favorable mechanical and functional properties. Industrial hemp fibers have gained worldwide attention as a sustainable material thanks to their high strength, durability, thermal and acoustic insulation properties, and resistance to ultraviolet radiation [8]. These features make hemp fiber an attractive reinforcement for blending with PVC in composite production. Although PVC has a relatively low processing temperature that makes it thermally compatible with hemp fibers, enabling their co-processing without thermal degradation, chemical compatibility between the hydrophilic fiber surface and the hydrophobic PVC matrix remains limited.

PVC is among the thermoplastics suitable for use with hemp fiber due to its melting temperature being below the thermal degradation threshold of the fiber. Additionally, hemp fibers exhibit the highest Young's modulus values among natural fibers, identifying them as the strongest cellulose-based fibers. Structurally, hemp fibers consist of multicellular bundles where primary bast fibers are bound together by pectin or lignin. These fibers typically range in length from 5 to 55 mm and have an average thickness of approximately 20 μm [9]. They are also known for their excellent tensile strength. Another critical

advantage of hemp fibers is their high aspect ratio, which significantly contributes to their effectiveness as reinforcement materials in composite applications [10].

Hemp fiber has a tensile strength of 550–900 MPa, higher than jute and kenaf, and similar to high-performance flax. Its 70 GPa elastic modulus ranks among the highest for natural fibers, showing excellent stiffness and load-bearing capacity. With an elongation at break of 1.6–4.0%, it is more flexible than flax and kenaf but far less than coir. This mix of high strength, high stiffness, and moderate flexibility makes hemp fiber an appealing reinforcement for polymer composites, offering both mechanical performance and dimensional stability [9].

Natural fibers are inherently hydrophilic, have weak resistance to moisture, and are incompatible with the hydrophobic PVC matrix [11]. This incompatibility of natural fibers results in a weak fiber/matrix interface, leading to a reduction in the mechanical bonding of composites. The reinforcement of hydrophilic natural fibers in a PVC matrix leads to a heterogeneous system with lower properties due to weak fiber-matrix adhesion.

Due to the hydroxyl (-OH) groups present in the cellulose and lignin structure of natural fibers, these fibers have great potential for chemical treatment. The reaction of the -OH group can alter the surface energy and polarity of natural fibers [12]. The chemical treatment or surface modification of fibers improves fiber-matrix adhesion, which is critical for the further development of composites.

Fiber modification techniques involve various chemical and biological treatments to enhance fiber-matrix compatibility and improve mechanical properties [13]. Among these techniques, alkali treatment was chosen due to its simplicity and cost-effectiveness compared to other chemical treatments, such as silane or acetylation. Additionally, alkali treatment has been reported to have lower energy consumption and waste production than some alternative chemical modification techniques [14].

Equation 1 below represents the reaction of natural fiber with sodium hydroxide alkaline agent [14].

$$Fiber - OH + NaOH \rightarrow Fiber - O - Na + H_2O \qquad (1)$$

Materials and Methods

This section provides detailed information about the materials and methods used in the study. The surface modification process applied to hemp fibers, the subsequent analyses, and the production of the blend polymer are explained in detail.

Materials

Industrial hemp fibers were obtained from the Hemp Research Institute of 19 Mayıs University. The chemicals used in the surface modification process, NaOH and acetic acid, were supplied by Ege Laborsis Dış Tic. Ltd. Şti. PVC compounds were supplied from the EGE PROFİL Tic. ve San. Anonim Şti.

Methods

This study consists of five main steps: Optical Microscopy Measurements, Surface Modification of Fibers, Verification Analyses of Surface Modification, Blending Test with Plastograph and Physical Analyses of the Final Product.

In the surface modification step, alkaline treatment, one of the most commonly used natural fiber treatment methods, was applied. To confirm the changes in OH content of the fibrils that occurred after the treatment, various analyses were conducted, including FTIR, SEM, and XRD.

Finally, the PVC-Hemp blend polymer was produced using the plastograph method, and the Tensile impact strength analysis of the obtained PVC-Hemp profile were performed.

The process for this study is presented in a diagram (see Fig. 1).

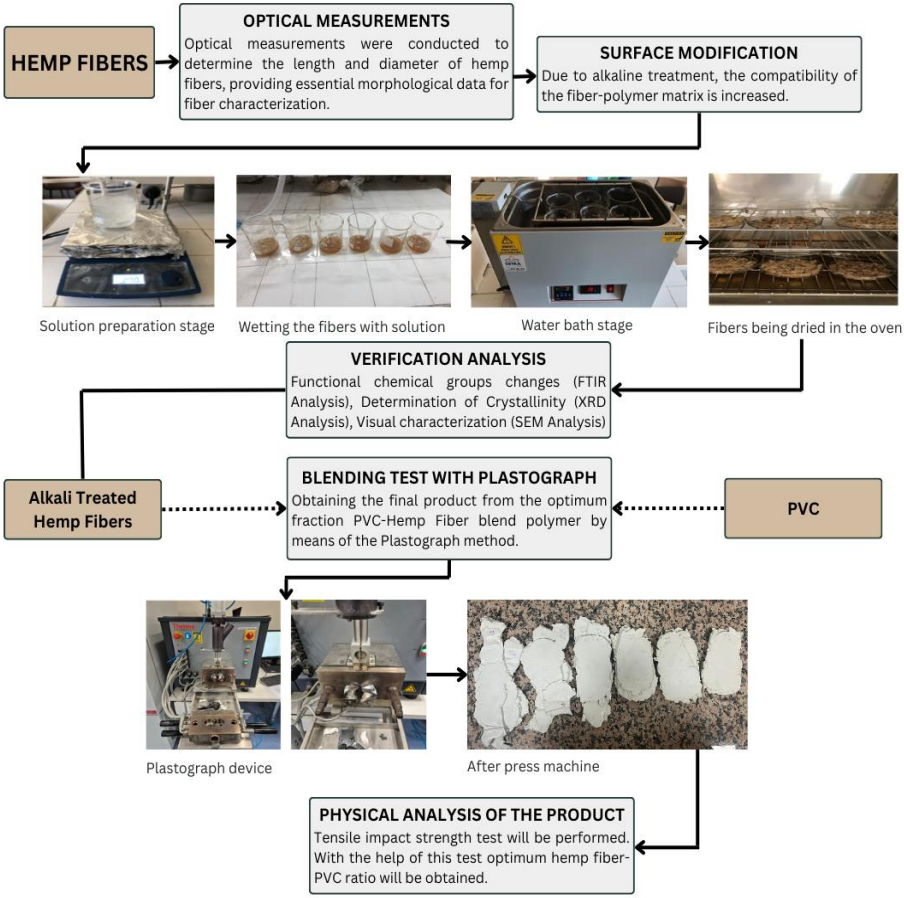

Fig. 1. Flow diagram of the study

Optical Microscopy Measurements of Hemp Fibers. In this study, the length and diameter of hemp fibers were measured using an optical microscope to obtain detailed morphological data. A total of approximately 75 individual measurements were conducted to ensure statistical reliability. The measurements were performed using a SOIF BK5000 optical microscope equipped with the MSHOT MicroShot v1.2 Image Processing System for precise image capture and analysis.

Surface Modification of Hemp Fibers. Hemp fibers were subjected to a mechanical separation process (combing) before chemical modification to enhance their interaction with the treatment solution. This process aimed to separate the fibers into finer strands, thereby increasing the surface area and improving the penetration and uniform distribution of the modifying agents. The prepared fibers were weighed precisely at 7.5 g using an analytical balance. NaOH-distilled water solutions were prepared at different concentrations (2%, 4%, 6%, 7.5%, 8%, 8.5%, 10%, and 12%). The fibers were then immersed in the prepared solution at a 40:1 liquor ratio. The soaked fibers were kept in a water bath set at 30°C for 4 hours. After the soaking process, the fibers were removed. To neutralize the excess sodium hydroxide, they were washed with a 1% acetic acid-distilled water solution and then rinsed with pure water [15]. After the rinsing process, the fibers were dried at room temperature for 48 hours and then in an oven at 100°C for 6 hours, completing the modification process [16].

Verification Analysis. Various analyses were conducted to observe the effects of the chemical treatments and determine the optimum sodium hydroxide concentration.

Fourier Transform Infrared Spectroscopy (FT-IR) Analysis. One of the greatest advantages of the infrared spectroscopy is that virtually any sample in any state may be analyzed. FTIR is a highly effective technique for analyzing the changes in hydrogen bonding caused by various defects. [17]. FT-IR spectroscopy method is broadly employed for cellulose researches, due that it offers an easy method for having direct information on chemical changes faced during some chemical treatments [18]. The functional groups of untreated, 2%, 4%,6%, 7.5%, 8%, 8.5%, 10% and 12% alkali treated hemp bast fibers were characterized by FTIR analysis on a FTIR spectrometer.

Scanning Electron Microscope (SEM) Analysis. It is an essential technique for characterizing the surface topography of natural fibers and assessing the impact of different pretreatments, such as alkaline treatment, as well as other functionalization processes applied to fiber surfaces [19]. In this study, SEM analysis was performed to evaluate the morphological changes in hemp bast fibers after chemical modification. The fiber surfaces were examined to determine structural alterations, surface roughness, and the degree of fibrillation induced by the treatment.

X-Ray Diffraction (XRD) Analysis. Crystallinity is a key parameter in cellulose, influencing the structural accessibility, physical properties, and mechanical performance of fibers [18]. Each crystalline phase diffracts X-rays in a characteristic manner, depending on its unique atomic arrangement, which allows the evaluation of structural modifications in natural

fibers. X-ray diffraction (XRD) is widely used to analyze the crystalline structure of fibers, providing insights into the effects of chemical treatments on their structural integrity [20].

In this study, XRD measurements were performed to investigate the impact of alkaline treatment on the crystallinity of hemp bast fibers. The crystallinity index before and after modification was determined to assess the degree of structural transformation.

Blending test with Plastograph

Plastograph Method. As a result of the reinforcement of hemp fibers with different fractions to PVC, the product was obtained with the "Plastograph" method in order to determine the optimum fraction and temperature that will best develop the mechanical properties. For this purpose, PVC-hemp fiber composite material was added at 1%, 2% 3%, 4%, 5% and 6% by mass. As a result of the obtained products, the applicability of hemp fibers with PVC was examined and the optimum working temperature of the composite in different fractions was determined. The product coming out of the plastograph was cooled by giving a certain shape while hot and its physical tests were performed.

Physical Analysis of the Product. 0% (pure PVC), 1%, 2%, 3%, 4%, 5%, and 6% (by mass) hemp fiber-PVC composites were tested for tensile impact strength to assess how fiber content influences mechanical performance and to identify the optimum reinforcement ratio.

Results and Discussions

Optical Measurement of Hemp Fibers

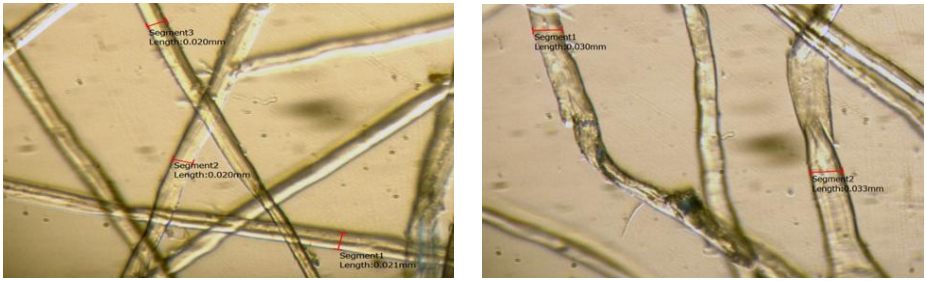

Fig. 2. Diameter measurement of untreated hemp fibers

According to the results, the fiber diameters exhibited a relatively narrow distribution, with most values ranging between 15 µm and 40 µm. The calculated mean diameter was approximately 22 µm, which is consistent with previously reported ranges for bast fibers used in composite materials. The diameter measurements indicates that the majority of the fibers fall within the 20–25 µm range, suggesting a fairly uniform size profile (see Fig. 2-3).

Fig. 3. Histogram of hemp fiber diameter distribution

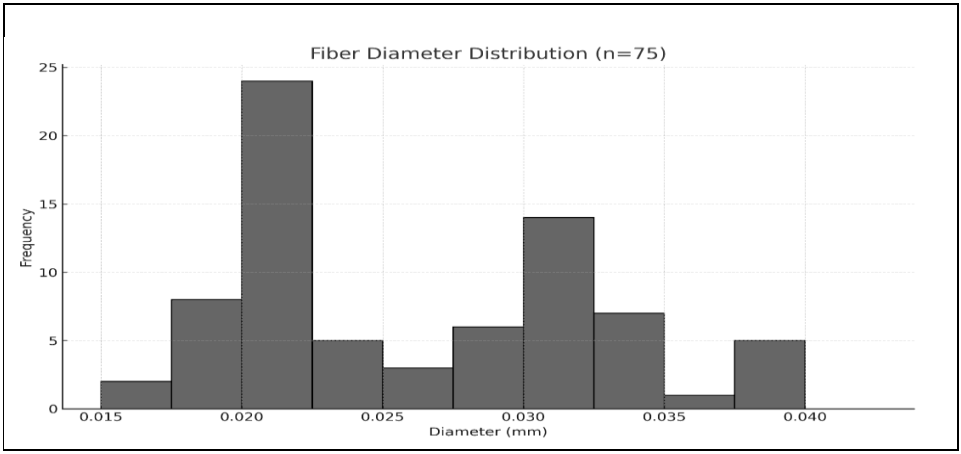

FTIR analysis of hemp fibers

FTIR analysis showed that the broad band at ~3400 cm^{-1} corresponds to O–H stretching in cellulose, hemicellulose, pectin, and water [21]. Untreated fibers showed the strongest absorption, while NaOH treatment (up to 8%) increased transmittance, indicating removal of hemicellulose and pectin and reduced hydrophilicity (see Fig. 4).

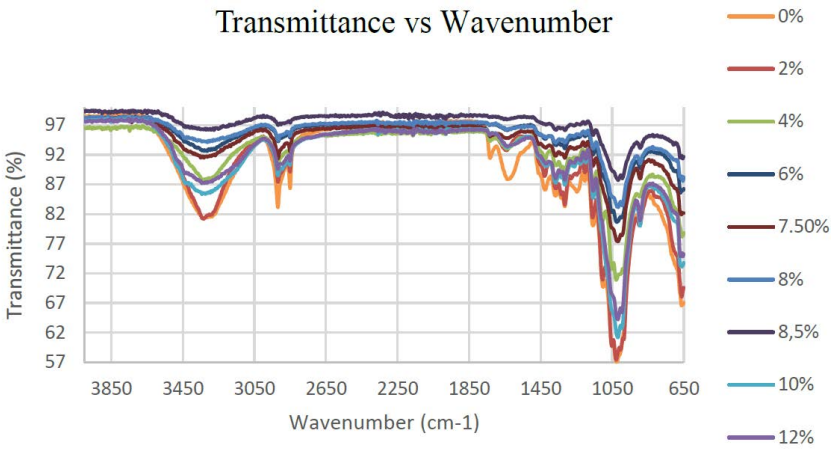

Fig. 4. FTIR analysis after alkali treatment

The FTIR band at ~1000 cm^{-1}, attributed to C–O stretching in hemicellulose, pectin, and cellulose, showed marked changes after alkali treatment [21]. Transmittance increased with NaOH concentration up to 8%, indicating effective removal of hemicellulose and pectin while maintaining cellulose, thereby enhancing crystallinity and PVC compatibility (see Fig. 4). At higher levels (10–12%), a slight decrease suggested cellulose damage. FTIR analysis identified 8% NaOH as the optimal concentration for reducing OH groups, with a refined analysis confirming 8.5% as the most effective level.

Scanning Electron Microscopy Analysis (SEM EDS)

The fiber samples were coated with a thin layer of gold/palladium to ensure conductivity prior to imaging and examined using a Scanning Electron Microscope (SEM) in Secondary Electron (SE) mode. During the measurements, an accelerating voltage of 7.50 kV, a spot size of 9.0, a probe current of approximately 0.20 nA, a working distance (WD) of 8.6–9.3 mm, and a magnification of 10,000× were used.

Figure 5(b) shows the hemp fiber surface appears rough, with visible longitudinal grooves and separated fibrils, indicating effective removal of non-cellulosic components such as hemicellulose, lignin, and waxes through alkali treatment. This fibrillated and porous structure enhances surface area and mechanical interlocking, making the fiber more suitable for composite reinforcement. In contrast, Fig. 5(a) shows a smoother, more compact fiber surface, characteristic of untreated hemp. The presence of a continuous outer layer suggests that non-cellulosic substances remain, limiting interfacial bonding with hydrophobic polymer matrices.

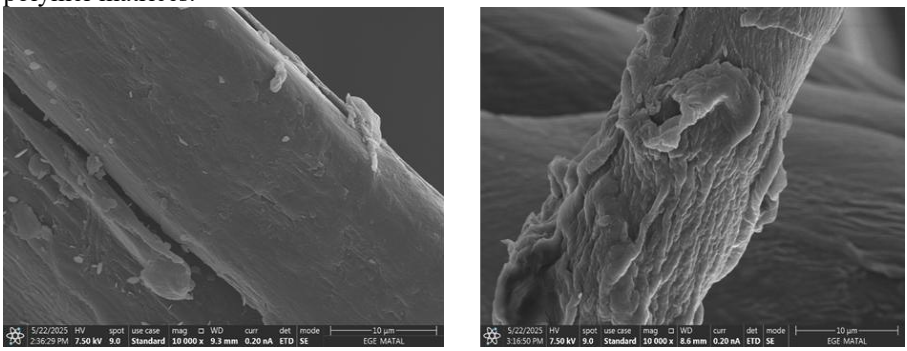

Fig. 5. Longitudinal view of untreated (a) and 8.5% treated (b) hemp fiber at 10 µm scale

X-Ray Diffraction (XRD) Analysis

X-ray diffraction (XRD) analysis was performed to evaluate changes in hemp fiber crystallinity after alkali treatment. Using the Segal method, the crystallinity index (CrI) increased from 59.24% in untreated fibers to 73.26% in fibers treated with 8.5% NaOH (see Fig.6). This improvement is attributed to the removal of hemicellulose, lignin, and other amorphous components, yielding a more crystalline cellulose structure.

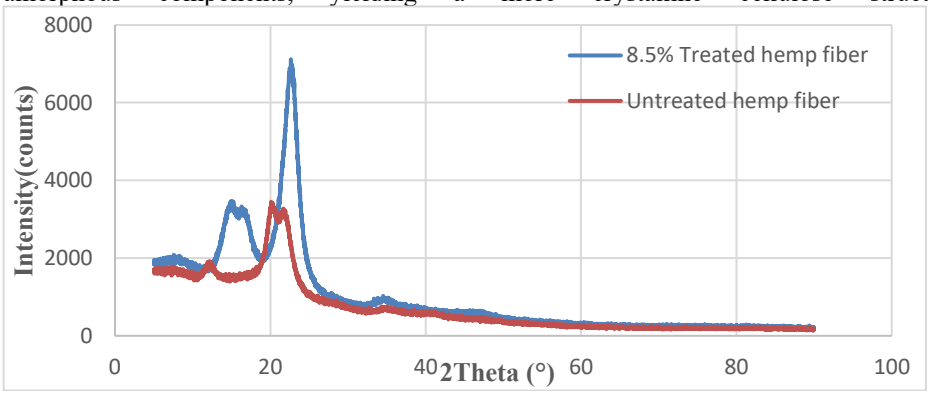

Fig. 6. X-ray diffraction analysis of alkali-treated and untreated hemp fibers

Physical Analysis of the Product

Table 1 shows the experimental test results. The tensile impact strength of pure PVC was 49.6 kJ/m², while the addition of 1% and 2% hemp fiber increased it to 63.7 and 67.4 kJ/m², respectively. Notably, at 3% fiber content, the highest strength was achieved with a 41.5% improvement. A reduction in tensile strength was observed when the fiber content exceeded 3%. This indicates that at fiber contents up to 3% the fiber–matrix interaction remains effective, whereas contents above 3% lead to fiber agglomeration and weak interfacial bonding, which ultimately deteriorate the mechanical properties. For this test, the products were given the shape shown in Fig. 7.

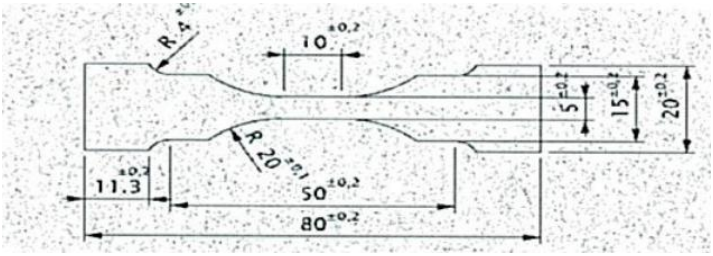

Fig. 7. Standard shape of sample for Tensile impact strength test

Table 1. Tensile Impact Strength Comparison of PVC Composites Reinforced with Different Hemp Fiber Weight Fractions

Sample	Hemp Fiber content (weight percent)	Tensile impact strength (kJ/m²)	Relative change (compared to pure PVC)
Reference Sample	0%	49.6	Base
Sample 1	1%	63.7	28.4%
Sample 2	2%	67.4	35.9%
Sample 3	3%	70.2	41.5%
Sample 4	4%	49.0	-1.21%
Sample 5	5%	36.9	-25.6%
Sample 6	6%	35.2	-29.0%

Conclusions

In this study, alkali treatment at different NaOH concentrations was applied to improve the interfacial compatibility between hemp fibers and PVC. Validation analyses confirmed the effectiveness of the treatment, and the most suitable concentration for fiber modification was determined to be 8.5%. Subsequently, PVC–hemp fiber composites with varying fiber mass fractions (0, 1, 2, 3, 4, 5, and 6 wt%) were prepared using the plastograph method to identify the optimum composition providing the best mechanical performance. During processing, it was observed that increasing fiber content and extended gelation time in the plastograph led to more pronounced yellowing of the composites, which can be attributed to the inherent color of hemp fibers. Moreover, higher fiber loadings resulted in increased surface roughness, thereby reducing the smoothness of the final product. Fiber agglomeration was also identified as a critical factor causing deterioration in mechanical properties across the formulations. Among the tested composites, the tensile impact strength results revealed that 3 wt% hemp fiber addition represents the optimum reinforcement level, achieving the best balance between fiber–matrix compatibility and mechanical performance.

References

[1] SpecialChem, https://www.specialchem.com/plastics/guide/polyvinyl-chloride-pvc-plastic, last accessed 2025/05/03.

[2] Elgharbawy, A.S.: Poly Vinyl Chloride additives and applications – a review. Journal of Risk Analysis and Crisis Response 12(3), 143–144 (2022).

[3] Thacker, G.A.: Heat stabilizers: How to select the right grade for PVC? In: *SpecialChem Polymer Additives Guide*, https://www.specialchem.com/polymer-additives/guide/pvc-heat-stabilizers-selection, last accessed 2025/05/14

[4] Bisley International, https://bisleyinternational.com/what-additives-are-added-to-pvc/, last accessed 2025/04/24.

[5] H, A., Sabu, T.: Poly (Vinyl Chloride) Based Composites and Nanocomposites. Springer, Cham, pp. 102-103 (2024).

[6] Ramesh, M.: Kenaf (Hibiscus cannabinus L.) fibre based bio-materials: a review on processing and properties. Prog. Mater. Sci. 78–79, 3-4 (2016).

[7] Khalil, H.A., Tehrani, M., Davoudpour, Y., Bhat, A., Jawaid, M., Hassan, A.: Natural fiber reinforced poly(vinyl chloride) composites: a review. J. Reinf. Plast. Compos. 32(5), 330–331 (2013). https://doi.org/10.1177/0731684412458553

[8] Awwad, E., Mabsout, M., Hamad, B., Farran, M. T., Khatib, H.: Studies on fiber-reinforced concrete using industrial hemp fibers. Construction and Building Materials 35, 710–717 (2012).

[9] Deshmukh, G.S.: Advancement in hemp fibre polymer composites: a comprehensive review. J. Polym. Eng. 42(7), 576–577 (2022). https://doi.org/10.1515/polyeng-2022-0033
[10] Promhuad, K., Srisa, A., San, H., Laorenza, Y., Wongphan, P., Sodsai, J., et al.: Applications of hemp polymers and extracts in food, textile and packaging: a review. Polymers 14, 4274 (2022). https://doi.org/10.3390/polym14204274
[11] Jawaid, M., Khalil, A.: Cellulosic/synthetic fibre reinforced polymer hybrid composites: a review. *Carbohydr. Polym.* 86(1), p.6 (2011). https://doi.org/10.1016/j.carbpol.2011.04.043
[12] Lee, Hao, C., Khalina, A., Lee, Hua, S.: Importance of Interfacial Adhesion Condition on Characterization of Plant-Fiber-Reinforced Polymer Composites: A Review. *Polymers*, 13(3), 438. p.6 (2021). https://doi.org/10.3390/polym13030438
[13] Thyavihalli G., Y.G., Mavinkere R., S., Parameswaranpillai, J., Sien., S.: Natural fibers as sustainable and renewable resource for development of eco-friendly composites: A comprehensive review. *Front. Mater.* **6**, 226, p.8 (2019). https://doi.org/10.3389/fmats.2019.00226
[14] Koohestani, B., Darban, A.K., Mokhtari, P., Yilmaz, E., Darezereshki, E.: Comparison of different natural fiber treatments: A literature review. *Int. J. Environ. Sci. Technol.* **16(1)**, 634–635 (2018). https://doi.org/10.1007/s13762-018-1890-9
[15] Mwaikambo, L.Y., Ansell, M.P.: The effect of chemical treatment on the properties of hemp, sisal, jute and kapok for composite reinforcement. *Die Angew. Makromol. Chem.* 272(1), p. 5 (1999).
[16] Ray, D., Sarkar, B.K., Rana, A.K., Bose, N.R.: Effect of alkali treated jute fibres on composite properties. *Bull. Mater. Sci.* 24(2), p.130 (2001). https://doi.org/10.1007/bf02710089
[17] Fan, M., Dai, D., Huang, B.: Fourier Transform infrared spectroscopy for natural fibres. In: *InTech eBooks, p.47* (2012). https://doi.org/10.5772/35482
[18] Gümüşkaya, E., Usta, M.: Dependence of chemical and crystalline structure of alkali sulfite pulp on pulping temperature and time. *Carbohydr. Polym.* **65(4)**, 462–463 (2006). https://doi.org/10.1016/j.carbpol.2006.02.004
[19] Shahzad, A., Teacă, C.-A., Tanasă, F.: Natural fibers and surface treatment methods. In: Elsevier eBooks. pp. 19-31 (2022). https://doi.org/10.1016/b978-0-12-821863-1.00001-6
[20] Yaylalı, D., Uraz, C., Gümüşkaya, E.: Evaluating the performance of hemp bast fibers in the production of packaging paper with different waste paper blends. *Drewno Journal*, **65(209),** p:28, Poland, (2022). https://doi.org/10.12841/wood.1644-3985.400.02.
[21] UniTech Link: FTIR Analysis. https://unitechlink.com/ftir-analysis/, last accessed 2025/06/13.

Lap-Shear Strengths Of Glass, Basalt And Hybrid Composites

Hürrem Canıtez[1][0000-0002-6272-435X – ORCID ID], Hülya Karaçeper[1][0009-0008-6939-1122 - ORCID ID]

[1] Material Research & Validation Department, Sazcılar Automotive, 16140 Bursa, Türkiye

hurrem.canitez@sazcilar.com.tr

Abstract. Composite materials are widely used in lightweight structural applications due to their high strength-to-weight ratio. In this study, glass fiber reinforced (GFRP), basalt fiber reinforced (BFRP), and glass–basalt hybrid (GBFRP) thermoset composites were produced via vacuum infusion under identical conditions. Adhesively bonded joints were prepared in composite–composite and composite–stainless steel configurations using a constant bondline thickness, and their lap-shear strength was evaluated according to EN 1465. The results showed that BFRP–BFRP joints exhibited the highest shear strength, while GFRP–GFRP joints displayed the lowest values. In composite–metal joints, BFRP–SST achieved the highest strength, whereas GFRP–SST and GBFRP–SST showed similar performance. Fracture surface analysis based on ASTM D5573 revealed predominantly fiber tear–type failures, indicating adhesive-dominated joint behavior. The findings demonstrate that basalt fiber reinforcement enhances lap-shear performance by improving load transfer and resistance to near-surface damage in adhesively bonded joints.

Keywords: Glass, Basalt, Hybrid, Metals, lap-shear

1. Introduction

Polyester, epoxy, or vinyl ester resins with reinforcements like glass, carbon, or aramid fibers are frequently used in polymer matrix composites. Natural fibers are becoming more popular because glass fiber is inexpensive but difficult to recycle. Made from minerals, basalt fiber is non-toxic, safe for the environment, and has good adhesion to metals, epoxy, and adhesives. Automotive, construction, energy, petrochemical, wind turbine, and sports applications can all benefit from its thermal and acoustic insulation, as well as its resistance to alkalis, acids, and corrosion [1,2]. The viability of substituting basalt fiber for glass fiber in fiber-reinforced polymer composites made by vacuum bagging was examined by Lopresto et al. (2011). In comparison to glass fiber-reinforced composites, their mechanical test results showed that basalt fiber-reinforced composites had better tensile, flexural, and

compressive properties. This suggests that basalt fiber is a sustainable and mechanically competitive substitute for glass fiber reinforcement [3]. Soares et al. (2016) examined the tensile, compressive, shear, and flexural characteristics of polyester composites reinforced with basalt fibers made using the RTM technique. The findings demonstrated that, in comparison to traditional reinforcements, basalt fiber offers a balanced combination of stiffness and mechanical performance, with the Young's modulus of basalt fiber-reinforced composites falling between that of glass and carbon fiber composites [4]. By altering the surface of aluminium alloy sheets (EN AW-5754), Karapepas et al. (2019) examined the shear performance of thermoplastic hybrid laminates reinforced with basalt fiber. Their findings demonstrated that brief sodium hydroxide pickling and mechanical blasting together greatly increased tensile shear strength, highlighting the crucial function that metal surface activation plays in adhesive bonding. The study also demonstrated the potential of basalt-reinforced hybrid laminates for high-shear applications by highlighting how consolidation parameters and basalt fiber sizing affect shear performance [5]. The impact of low and sub-zero temperature ageing on the lap-shear strength of epoxy-bonded EN AW 2024 aluminium joints evaluated in accordance with DIN EN 1465 was examined by Rudawska et al. (2019). The findings showed that joint strength is greatly influenced by both adhesive formulation and service temperature, with several epoxy systems showing varied performance patterns based on the ageing temperature. The study demonstrated how environmental factors can significantly change the mechanical behaviour of adhesive junctions, highlighting how crucial it is to choose the right glue for endurance in a range of heat situations [6]. The direct adhesive bonding performance of thermoset-based SMC composites to AlSi-coated high-strength steel without prior surface treatment was examined by Wehler et al. (2020). The study showed that proper base resin selection was the only way to achieve adequate adhesion by isolating pure shear loading using an edge shear test. Because of better mechanical interlocking and resin infiltration into the porous AlSi covering, epoxy-based SMC systems showed noticeably higher shear strength than unsaturated polyester systems. The reported shear strength was consistently associated with fracture surface observations and surface energy measurements, underscoring the crucial significance of resin chemistry in metal–composite hybrid junctions [7]. The beneficial impact of basalt fiber integration on adhesive joint performance has also been shown in Locikova et al (2024) study. According to EN 302-1, the shear strength of beech wood lap joints bonded with a one-component polyurethane glue packed with basalt fiber was examined in one investigation. The findings demonstrated that, in comparison to the unfilled glue, the addition of basalt fibers greatly increased the bonded joints' shear strength. Additionally, using glue modified with basalt fiber increased the likelihood of substrate failure in the wood instead of interfacial failure, suggesting improved adhesion and load transfer at the bonding interface. These results demonstrate the potential of basalt fibers as

an efficient additive in adhesive systems to enhance lap-shear performance, as well as as a reinforcement in composite laminates [8]. The lap-shear performance of polybenzoxazine-based composites bonded by adhesive and hybrid (adhesive + rivet) bonding procedures was examined by Wolter et al. (2020). Vacuum infusion was used to create basalt and carbon fiber reinforced composites, which were then assessed for tensile, interlaminar shear, and lap-shear strength. The findings demonstrated that while hybrid bonded joints had greater energy absorption and fail-safe behaviour, adhesive bonding offered sufficient adhesion and cohesive strength for both fiber systems. There was no discernible impact of substrate thickness on lap-shear strength. Carbon fiber reinforced joints showed better lap-shear strength than basalt fiber reinforced joints, which is consistent with their higher interlaminar shear strength. Delamination of the outer laminate layer caused by peel loads was the predominant failure mode [9].

2. Materials and Methods

Glass fiber-reinforced, basalt fiber-reinforced, and glass–basalt hybrid laminates were the three types of composites that were produced. The vacuum infusion method and post-curing were used to produce each one. Layers of glass and basalt fiber alternately made up the hybrid composites. Following vacuum bagging and moulding preparation, resin containing MEKP catalyst was infused under a controlled vacuum until it was completely wet-out. It was then allowed to cure at ambient temperature before being post-cured in an oven. It has a 3 mm thickness. The adherend surfaces were prepared before adhesive bonding to guarantee consistent and dependable joint quality. Both composite and stainless steel adherends' bonding surfaces were mechanically cleaned and after that cleaned with a solvent to eliminate surface impurities like dust, oil. Prior to applying adhesive, samples were allowed to dry at room temperature. All preparation procedures were carried out by hand, and no extra chemical or plasma surface treatments were used. MMA type glue was used for the bonding of composites to stainless steel and composites to other composites. The adhesive joints' tensile lap-shear strength was performed in compliance with EN 1465. The standard specimen geometry was followed in the preparation of single-lap joint specimens with a nominal overlap length of 12.5 ± 0.25 mm and a width of 25 mm. Composite–composite and composite–stainless steel joints were realized under the same circumstances. Before bonding, the adherend surfaces were cleaned to eliminate impurities and guarantee consistent bonding conditions. Care was taken to achieve a consistent adhesive layer thickness, and the adhesive was applied in accordance with the manufacturer's instructions. Adherent was applied 0,2 mm thickness with using apparatus. Following curing, the specimens were tested at a constant crosshead speed of 2 mm/min using a universal testing apparatus. At least five specimens were tested for each configuration, and the maximum recorded load was divided by the nominal overlap area to determine the lap-shear strength. Following lap-shear testing, the specimens' fracture

surfaces were visually inspected, and ASTM D 5573 was used to categorise the failure modes. Produced groups and explanations mentioned in Table 1.

Table 1. List of lap-shear test groups

Abbreviations	Explanations
GFRP-GFRP	Glass Fiber-Glass Fiber Adhesion
BFRP-BFRP	Basalt Fiber-Basalt Fiber Adhesion
GBFRP-GBFRP	Hybrid-Hybrid Adhesion
GFRP-SST	Glass Fiber-Stainless Steel Adhesion
BFRP-SST	Basalt Fiber-Stainless Steel Adhesion
GBFRP-SST	Hybrid-Stainless Steel Adhesion

3. Results and Discussions

Lap-shear strength of adhesively bonded joints for both composite–composite and composite–stainless steel configurations shows in the Figures 1 and 2. The BFRP–BFRP group had the highest average lap-shear strength for composite–composite joints (21.97 ± 1.85 MPa), followed by GBFRP–GBFRP (17.64 ± 1.45 MPa) and GFRP–GFRP (15.43 ± 1.60 MPa). This pattern shows that under shear loading, basalt-based laminates clearly outperform hybrid laminates, which have an intermediate response. The same result was noted in joints made of composite and stainless steel: While GFRP–SST (21.00 ± 1.00 MPa) and GBFRP–SST (21.38 ± 1.15 MPa) were near to each other within the experimental scatter, BFRP–SST attained the maximum strength (25.92 ± 1.20 MPa). Due to the increased stiffness of the steel adherend and the consequent decrease in joint compliance and rotation during loading, composite–metal joints often demonstrated higher absolute strength than composite–composite joints. The adherend type (FRP vs. SST) and the reinforcement architecture (glass, basalt, or hybrid) are the main causes of the observed differences because all laminates were created by vacuum infusion using the same thermoset matrix and bonded using the same adhesive and controlled bondline thickness. Because of load eccentricity, single-lap shear joints create non-uniform shear stresses and extra peel/bending stresses, particularly around the overlap edges. This is an important consideration for interpreting these results. Consequently, joint rotation, overlap stress concentration, and the near-surface integrity of the adherends all affect the apparent lap-shear strength in addition to the cohesive strength of the adhesive. The adhesive layer thickness in the current study was kept at about 0.2 mm, and both overlap geometry and bondline thickness were standardised using a special bonding fixture. Although the bonding procedures were done by hand, these fixtures were used especially to reduce variability

from adhesive application, overlap alignment, and thickness control. The steady patterns across both joint types suggest a systematic material influence rather than random fluctuation, however minor variances inherent in manual processing may still contribute to scatter.

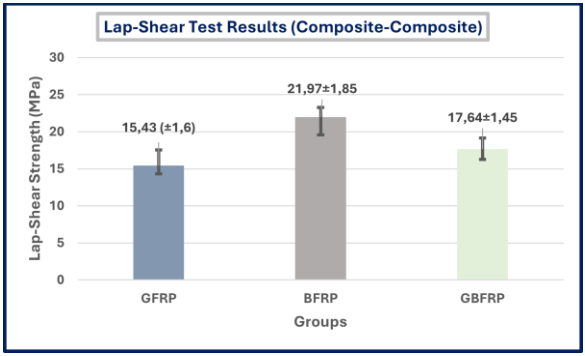

Fig. 1. Lap-shear test results of composite-composite samples

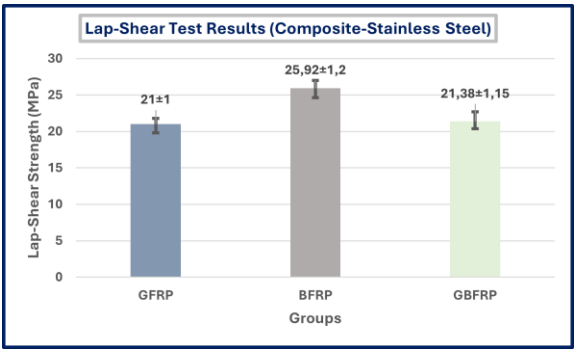

Fig. 2. Lap-shear test results of composite-stainless steel samples

Fracture surface observations (Figure 3) were assessed and failure modes were categorised in accordance with ASTM D5573 (Table 2) in order to explore the mechanism dictating "why basalt–basalt joints perform better." Fiber Tear Failure (FTF) and Light Fiber Tear Failure (LFTF) were the most common failure descriptions in all categories. Crucially, fiber-tear-type failures show that the fracture involves damage or rip within the composite surface plies or near-surface laminate region next to the bondline, rather than a

straightforward adhesive debond at the interface. In the terminology of adhesive joints, this is usually understood as proof that the adhesive–adherend interaction is strong enough that the joint tends to fail not by clean interfacial debonding but by tearing the composite substrate or by mixed fracture with substrate damage. GFRP–GFRP was categorised as FTF, whilst BFRP–BFRP and GBFRP–GBFRP were mostly categorised as LFTF. GFRP–SST and BFRP–SST were primarily FTF for composite–metal junctions, while GBFRP–SST was primarily LFTF. This pattern is consistent with an adhesive-dominated lap-shear response, in which the kind of reinforcement indirectly affects the joint through the near-surface damage resistance of the adherend and the way peel stresses encourage top-ply cracking/delamination at the overlap edges. It is expected that basalt-based laminates, which show better tensile/flexural performance in mechanical data published in the literature, will offer better resistance to local ply cracking and delamination initiation, allowing the bondline to support greater loads before substrate-assisted failure occurs. Due to its mixed contribution to near-surface damage resistance and intermediate stiffness/strength, the hybrid structure exhibits intermediate behaviour in composite–composite bonding.

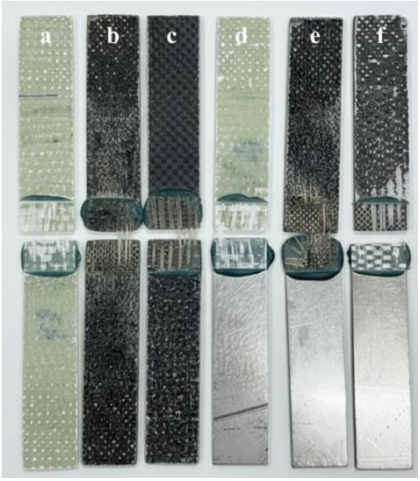

Figure 3. Representative fracture surfaces of lap-shear specimens for (a) GFRP–GFRP, (b) BFRP–BFRP, (c) GBFRP–GBFRP, (d) GFRP–SST, (e) BFRP–SST, and (f) GBFRP–SST joints after testing.

Table 2. Failure mode classification of lap-shear specimens according to ASTM D 5573

Groups	Predominant Failure Mode
GFRP-GFRP	FTF
BFRP-BFRP	LFTF
GBFRP-GBFRP	LFTF
GFRP-SST	FTF
BFRP-SST	FTF
GBFRP-SST	LFTF

Lastly, when comparing absolute strength numbers to literature, the adhesive system selection should be taken into account. Epoxy-based structural adhesives, which frequently offer more cohesive strength and stiffness than MMA-type adhesives, are used in several lap-shear experiments on FRP joints. Since an MMA adhesive was utilised in this work, the absolute lap-shear strengths may be lower than those of epoxy-bonded systems documented in the literature, especially if the adhesive's cohesive qualities become a limiting issue. However, the comparison ranking is still significant since all groups used the same MMA adhesive, thermoset matrix, and controlled bondline thickness. In other words, the study's contribution is a controlled evaluation of how reinforcement type (GFRP vs. BFRP vs. GBFRP) influences joint performance in real-world MMA-bonded composite–composite and composite–metal assemblies rather than the absolute maximum strength achievable with an optimised epoxy system.

4. Conclusions

The lap-shear performance of adhesively bonded joints produced from vacuum-infused composite laminates was methodically examined in this work for both composite–composite and composite–stainless steel configurations. The same thermoset matrix system was used in the production of glass fiber reinforced (GFRP), basalt fiber reinforced (BFRP), and glass-basalt hybrid (GBFRP) laminates. These laminates were bonded with the same MMA-based structural adhesive and linked with a regulated adhesive layer thickness. The impact of reinforcing type on adhesive-dominated joint behaviour could be directly and carefully compared thanks to this method. According to the results of the lap-shear test, GBFRP joints performed in between BFRP and GFRP systems, whereas BFRP joints consistently showed the maximum shear strength in both composite–composite and composite–metal configurations. Because of the increased stiffness of the metallic adherend, which improves load transfer and reduces joint compliance, composite–stainless steel joints showed higher absolute shear strength than composite–composite joints. The

very similar performance of GFRP–SST and GBFRP–SST joints indicates that, in composite–metal bonding, the adhesive–metal interface and joint geometry are more important than the type of reinforcement alone, especially when hand bonding techniques are used. The observed patterns were explained mechanistically by fracture surface observations and ASTM D5573 failure mode categorisation. The prevalence of fiber tear-type failures (FTF and LFTF) suggests that the bonded region, not early debonding at the adhesive–adherend interface, was the primary cause of failure. The improved resistance of basalt-based joints to near-surface damage and ply ripping under combined shear and peel pressures is consistent with their higher lap-shear strength, which enables the adhesive layer to withstand greater loads prior to joint failure. Although epoxy-based adhesives are more frequently described in the lap-shear literature and typically show higher cohesive strength, it should be emphasised that an MMA-based glue was employed in this work. The consistent use of the same adhesive throughout all test groups guarantees that the comparison conclusions regarding reinforcing type remain valid, even though this choice may reduce the absolute strength values compared to epoxy-bonded structures. To further assess the impact of adhesive chemistry on joint performance and compare the outcomes with higher-strength adhesive systems, future research could replicate the current experimental framework using a structural adhesive based on epoxy.

References

[1] Singha, K. (2012). A short review on basalt fiber. International Journal of Textile Science, 1(4), 19-28.

[2] Jamshaid, H., & Mishra, R. (2016). A green material from rock: basalt fiber–a review. The Journal of The Textile Institute, 107(7), 923-937.

[3] Lopresto, V., Leone, C., & De Iorio, I. (2011). Mechanical characterisation of basalt fibre reinforced plastic. Composites Part B: Engineering, 42(4), 717-723.

[4] Soares, B., Preto, R., Sousa, L., & Reis, L. (2016). Mechanical behavior of basalt fibers in a basalt-UP composite. Procedia Structural Integrity, 1, 82-89.

[5] Karapepas, C., Trautmann, M., Todt, A., Al-Obaidi, A., Nendel, S., Kräusel, V., & Wagner, G. (2019). Development of tailored hybrid laminates: Manufacturing of basalt fibre reinforced thermoplastic orthoses with aluminum thin sheets. Key Engineering Materials, 809, 245-252.

[6] Rudawska, A., Sikora, J. W., Müller, M., & Valášek, P. (2020). The effect of environmental ageing at lower and sub-zero temperatures on the adhesive joint strength. *International Journal of Adhesion and Adhesives*, *97*, 102487.

[7] Wehler, S., Moritz, P., Fischer, F., & Gude, M. (2021). On the strength of joints of metal-plastic composites of hot-formed steel with an AlSi coating and a thermosetting fiber reinforced compression material. *Proceedings of the Institution of Mechanical Engineers, Part D: Journal of Automobile Engineering*, *235*(5), 1183-1190.

[8] Laciková, P., Vaněrek, J., Bět'ák, A., Böhm, M. (2024). Improving the tensile shear strength of lap joints of beech wood by adding basalt fibers to polyurethane adhesive. *AIP Conf. Proc. 3094, 120006.*

[9] Woltera, N., Bebera V.C, Bredea, M., Koschek, K. (2020). Adhesively- and hybrid- bonded joining of basalt and carbon fibre reinforced polybenzoxazine-based composites. *Composite Structures 236, 111800.*

Investigation Of The Impact of Ceramic Fiber Addition on The Friction Performance of Brake Pad Compositions

Buse Can[1[0009-0004-9589-0786]], Merve Kalaycı[1[0000-0002-8693-3703]], Osman Dalar[1[0000-0002-5400-6139]]

[1] Beser Brakes, Izmir, 35050 Izmir, Turkiye

Buse.demirel@beser.com.tr, Merve.kalayci@beser.com.tr, Osman.dalar@beser.com.tr

Abstract: Brake pads are multi-component composite systems operating under high tem perature and friction, ensuring safe vehicle deceleration. Their performance de pends on the chemical, thermal, and mechanical properties of binder resins, rein forcing fibers, friction modifiers, and fillers. Increasing sustainability demands

and the need for high-temperature durability have positioned alumina–silica ce ramic fibers as a promising reinforcement due to their low toxicity and superior thermomechanical stability.

This study systematically investigates the influence of alumina–silica ceramic fiber addition on the tribological, mechanical, and chemical behavior of brake pads. Although previous research has examined ceramic fibers in composite fric tion materials, data specifically addressing heavy-duty brake pads remain limited. Therefore, this work provides an original contribution by evaluating ceramic fi ber performance under the high-load and high-temperature conditions typical of heavy-duty applications.

Composite pads containing 10% ceramic fiber were produced via hot-pressing and compared with a reference formulation through chemical (density, ash, mois ture, acetone extraction), mechanical (shear strength, compressibility), tribologi cal (Chase and dynamometer), and thermal (TGA) analyses. Results showed that ceramic fiber significantly improved mechanical properties, increasing internal shear strength by more than 50% per ISO 6312. Chase tests indicated stable fric tion behavior in the 0.480–0.530 range, corresponding to the G/G classification. Dynamometer results demonstrated reduced wear, enhanced fade resistance, and faster recovery for ceramic-fiber-reinforced samples.

Overall, alumina–silica ceramic fiber reinforcement provides stable friction per formance, improved mechanical strength, and high thermal stability, making it an effective and sustainable material for advanced heavy-duty brake pad designs.

Keywords: Friction coefficient, Brake pad, friction stability.

1 Introduction

Brake pads are one of the fundamental components of vehicle safety systems and, par ticularly in heavy-duty applications, are exposed to a highly complex tribological envi ronment due to the high temperatures and variable loads generated during braking [1,2]. Rapid temperature increases that may exceed several hundred degrees within a short time, fluctuations in surface pressure, and sudden changes in sliding speed at the pad– disc interface necessitate that friction materials maintain mechanical and thermal stabi lity under such harsh conditions [2]. Therefore, brake pads are designed as multiphase composite structures in which various constituents with distinct functionalities work together.

Within this composite system, the fiber phase plays a critical role in maintaining struc tural integrity and stabilizing friction performance [3,4]. The interaction between fibers and the matrix directly influences the formation of surface contact plateaus, the domi nant wear mechanisms, and the stability of the friction coefficient throughout the bra king cycle [4]. Following the prohibition of asbestos, interest has shifted toward alter native fiber types, and ceramic fibers have gained prominence due to their high tempe rature resistance [5].

Ceramic fibers produced from alümina (Al_2O_3), silica (SiO_2) or mullite-based compo sitions ($3Al_2O_3 \cdot 2SiO_2$) exhibit melting temperatures in the range of approximately 1650–2100 °C and low thermal expansion coefficients of about 0.5–8 × 10^{-6} K^{-1}, de pending on their composition and microstructure [14,15,16]. These physical properties enhance the composite's resistance to sudden temperature fluctuations during braking and reduce the propagation of microcracks within the matrix [6]. Their reinforcing ef fect also contributes to the stable development of the friction layer formed at the contact surface [5,6].

One of the key advantages of ceramic fibers is their influence on heat management. Compared with metal-based fibers (e.g., copper fiber: 380 W/m·K), alumina–silica fi bers exhibit significantly lower thermal conductivity values (typically ~2–4 W/m·K, with a broader range of 0.8–30 W/m·K depending on structure), enabling a more cont rolled rise in surface temperature and delaying thermal degradation of the binder resin at elevated temperatures [17,7]. Thus, temperature-induced performance loss, known as fade, is mitigated, and the friction coefficient can remain stable over longer braking cycles [7]. Furthermore, both fiber distribution and fiber length play decisive roles in governing heat transfer within the composite [6]. For ceramic fibers with diameters of 0.5–1.5 μm, the "critical fiber length" (Lc)

is reported to range between 40–150 μm [10,11]. When the fiber length falls below this threshold, increased interfacial thermal resistance between the fiber and matrix reduces effective thermal conductivity by app roximately 20–35% [12,13].

From an environmental perspective, international regulations (e.g., ECE R90, Euro 7, copper-reduction directives) increasingly require brake pad formulations to be more environmentally friendly and to produce lower emissions. Ceramic fibers generate fewer airborne particles compared with metal fibers and produce more inert debris during wear, thereby reducing environmental impact [9]. This makes them an attractive option for developing sustainable brake materials with a reduced environmental footp rint.

In this context, ceramic fiber reinforcement has become an increasingly strategic com ponent in modern brake pad design due to its advantages in terms of high temperature stability, consistent friction behavior, reduced wear rate, improved NVH performance, and compliance with environmental regulations [5–9]. This study aims to investigate the effects of alumina–silica fiber reinforcement on the thermal, mechanical, and tribo logical behavior of brake pads and thereby contribute to the development of high-per formance friction materials.

Studies examining the use of ceramic fibers in brake pads have consistently demonst rated that fiber reinforcement plays a crucial role in high-temperature resistance, wear behavior, and friction stability. Kim and Jang (2001) reported that brake pads contai ning mullite and glass fibers formed more stable secondary plateaus (compact micro scale contact regions formed by compressed wear particles and degraded resin) under elevated temperatures, reducing fluctuations in the friction coefficient and enhancing fade resistance [18]. Mutlu et al. (2011) showed that alumina–silica fibers improved the mechanical strength of brake pads, reduced wear rate, and provided more stable tribo logical behavior than metal fibers, especially at high temperatures [7]. Kchaou et al. (2013) demonstrated that varying ceramic fiber ratios directly influenced plateau morp hology, with higher ceramic fiber content promoting denser and more stable tribofilms, thereby improving both friction stability and wear performance [8]. Collectively, these studies confirm that ceramic fiber reinforcement provides significant performance and thermal durability benefits in brake pad formulations.

In this study, the compositions and tribological properties of brake pads designed for heavy-duty vehicle groups and reinforced with alumina–silica fibers were systemati cally compared and examined. The objective is to achieve high-temperature resistance, stable friction performance, and low wear in brake pads through the incorporation of alumina–silica ceramic fibers, while also offering environmental sustainability due to their lower particulate emissions compared with metallic fibers. In this context, brake pads containing 10% ceramic fiber were produced using the hot-pressing method. Fol lowing mixing, pressing, and curing processes, the samples were subjected to chemical tests (acetone extraction, ash content, moisture content, and density) and physical tests (shear strength, compressibility, Chase friction testing, and dynamometer analyses). In addition, thermogravimetric analysis (TGA) was conducted to investigate their degradation

behavior at elevated temperatures.

2 Materials and Methods

2.1. Materials Used

Studies have demonstrated that the type, particle size, shape, and amount of the mate rials forming the composite directly affect its friction and wear properties. Accordingly, while designing the composite formulation, the characteristics of the materials and find ings from previous studies were taken into consideration. The composite composition and the properties of the materials are presented in Table 1.

Table 1. Composite components and material properties

Material	**Type**
Phenolic Resin	Binder
Steel Shaving	Metallic Chips
Graphite	Solid Lubricant
Powder Cashew	Friction Modifier
Barite	Space Filler
Ceramic Fiber (Alumina-Silica)	Reinforcement

In this study, three main groups of components were used in brake pad production, selected to optimize the tribological performance:

Binder: A thermosetting phenolic resin was preferred due to its ability to provide high mechanical strength and thermal stability.

Fillers: Barium sulfate ($BaSO_4$) and calcium carbonate ($CaCO_3$) were added to increase the density of the pad and contribute to friction stability.

Friction modifiers: Materials such as graphite, steel powder, and cashew dust were incorporated to maintain a stable coefficient of friction and ensure balanced heat dissi pation during braking.

In addition to these, a ceramic fiber reinforcement containing 47% Al_2O_3 and 52% SiO_2, with thermal resistance up to 1200 °C, was selected as an additive. The ceramic fibers, supplied with diameters ranging from 2.9 µm to 15 µm, were incorporated into the composite at a ratio of 10%. The Scanning Electron Microscopy (SEM) image of the ceramic fiber is presented in Figure 1. SEM analysis was conducted using a Zeiss SUPRA 40VP instrument (SE2 detector, 500× magnification, 10.000 kV acceleration voltage).

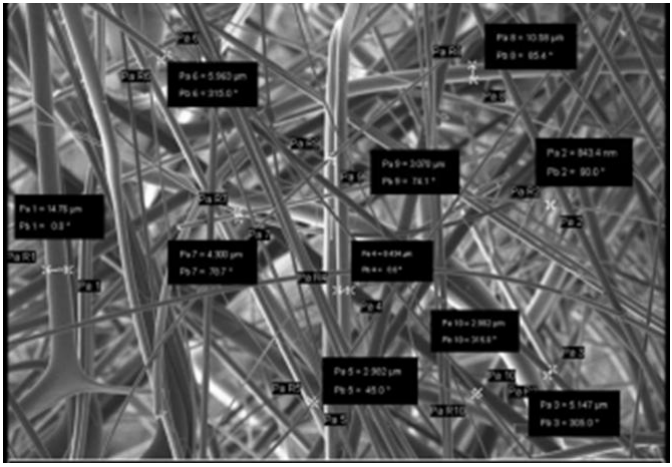

Figure 1. SEM image of the ceramic fibers (*TechnoTherm*)

2.2. Sample Preparation

Brake pad samples were fabricated by ten different powder materials. Alumina–silica ceramic fiber was incorporated at a ratio of 10% as an alternative rein-forcement mate rial.

The composition of the ceramic-fiber-reinforced brake pad (CF-BP) is presented in Table 2. In addition, a reference brake pad composition (BP) without ceramic fiber was also prepared.

Table 2. Brake pad composition

Material	Weight Ratio (%)
Phenolic resin	8-12
Vermikülit	2-5
Graphite	10-12
Powder cashew	8-10
Barite	8-10
Fiber	2-5
Metal sulfide	5-7
Steel powder	22-30
Mica	6-8
Ceramic fiber	10

The ceramic fiber was first opened in a high-speed mixer (70 rpm) to ensure a homo geneous blend before incorporating it into the formulation. Subsequently, all brake pad components were mixed in the same mixer for 5 minutes. The mixtures were then poured into cleaned and preheated molds, followed by a hot-pressing process. As shown in Table 3, pressing was carried out at 150 °C, under 120 bar of pressure, for 8 minutes. After pressing, the samples underwent a curing process at 200 °C for 7 hours with a gradual temperature increase to allow the internal structure of the material to stabilize fully. The resulting composites were then cut and prepared according to the dimensions required for the respective tests.

Table 3. Production parameters of composites

	Time (min)	**Pressure (bar)**	**Temperature (°C)**
Mixing	5	-	-
Hot molding	8	120	150
Curing	360	-	Gradual, 200

The brake pad sample produced after the curing process is shown in Figure2.

Figure 2. Ceramic fiber–reinforced brake pad

2.3. Chemical Tests

The characterization tests performed on the samples as given in the following.

Density determination was completed based on measurements according to ASTM D792 using the buoyancy principle in water.

Moisture content and ash percentage was calculated through drying at 105 °C and com bustion at 600 °C.

Acetone extraction was performed using a Soxhlet apparatus to examine the sol-ubility of the phenolic resin.

These tests are critical for evaluating not only the fundamental chemical constit-uents of the brake pads but also the stability of the binder phase.

2.4. Mechanical and Tribological Tests

2.4.1. Shear Strength Test

The internal shear strength of the samples was measured using the Shear Strength test ing device shown in Figure 3, in accordance with the ISO 6312 standard.

Figure 3. Shear strength testing device

2.4.2. Compressibility Test

The compressibility test is a mechanical test used to examine the elastic and plastic deformation of brake pads and other composite materials under load. Compression tests were conducted at room temperature and elevated temperatures in accordance with ISO 6310 and SAE J2468 standards, using the compressibility testing device shown in Figure 4. A gradual pressure of 80 bar was applied to the samples at 23 ± 5 °C and 400 ± 10 °C, and the procedure was repeated three times. According to the obtained results, the compressibility at 23 ± 5 °C should be ≤ 2%, while at 400 ± 10 °C, it should be ≤ 5% [19].

Figure 4. Compressibility testing device

2.4.3. Friction and Wear Test

Friction and wear tests applied to the brake pad samples were performed in accordance with SAE J661 and SAE J2522 standards using the Chase and dynamometer devices shown in Figures 5 and 6, respectively. The Chase test, based on the SAE J661 standard, was used to examine the coefficient of friction and wear behavior. The dynamometer test, based on the SAE J2522 standard, enabled a detailed evaluation of friction stabil ity, wear rate, and temperature effects under simulated real driving conditions. The dynamometer test, based on the SAE J2522 standard, enabled a detailed evaluation of friction stability, wear rate, and temperature effects under simulated real driving conditions.

Figure 5. Chase test apparatus and test specimen

The Chase test is performed using a brake pad specimen cut to dimensions of 25.4 × 25.4 × 40 mm, which is pressed against a rotating drum. While the drum rotates at controlled speeds, a regulated load is applied to the specimen. The drum speed is set to approximately 400 rpm, and the applied pressure is around 1 MPa, causing the temper ature to rise up to 400 °C. Under these conditions, the coefficient of friction is measured as cold μ and hot μ.

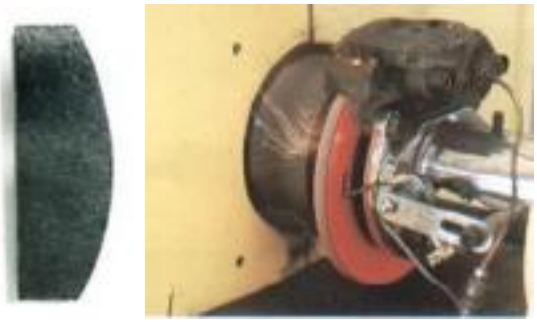

Figure 6. Dynamometer test apparatus and test specimen

The dynamometer test is essentially a laboratory reproduction of the actual vehicle braking system (disc, pad, and caliper). The brake disc is rotated by a high-power elec tric motor, while the brake pad applies pressure through a hydraulic system. The brake pad samples to be tested are mounted on the dynamometer in their actual vehicle di mensions. The test is carried out at various speeds ranging from 20 km/h to 120 km/h, simulating the vehicle's hydraulic braking conditions. Throughout the test, key perfor mance parameters such as coefficient of friction, wear rate, noise, and vibration behav ior are evaluated.

2.4.4. Thermogravimetric Analysis (TGA)

Thermogravimetric Analysis (TGA) was performed to evaluate the high-temperature behavior of the composites. The analysis was conducted in a nitrogen atmosphere using the TGA device shown in Figure 7, within a temperature range of 25–600 °C and a heating rate of 10 °C/min. This method played a critical role in examining the thermal degradation mechanism of ulexite and assessing the structural stability of the brake pads under elevated temperatures.

Figure 7. TGA testing device and test specimen

3 Results and Discussions

3.1. Chemical Tests

The lower density of the brake pads containing 10% alumina–silica ceramic fiber (2.18 g/cm³), compared to the reference pad (2.30 g/cm³), is primarily attributed to the sig nificantly lower specific density of the ceramic fibers. By occupying volume within the composite structure, the fibers reduce the overall bulk density of the material.

The moisture content values were in the range of 0.12–0.15%, while the ash content increased from 73.0% to 75.5% with the addition of ceramic fiber. This rise is due to the fully inorganic nature of ceramic fibers, which contributes to higher residual ash.

Acetone extraction analysis revealed that the amount of soluble resin was 1.5%, com pared to 2.0% in the reference sample. The similarity of the results is attributed to the fact that the incorporation of ceramic fibers does not significantly alter the proportion of the organic phase within the brake pad composition.

3.2. Mechanical and Tribological Tests

3.2.1. Shear Strength

In the internal shear strength tests, conducted in accordance with the ISO 6312 standard, the ceramic-fiber-reinforced pads reached a value of 38.0 daN/cm², compared to 25.0 daN/cm² for the reference material. This outcome indicates that the ceramic fibers in teract compatibly with the matrix structure, not weakening the binder phase but rather enhancing its strength.

3.2.2. Compressibility

In the compressibility tests conducted in accordance with ISO 6310 standards, under an applied pressure of 80 bar, the ceramic-fiber-reinforced samples exhibited a com pressibility of 1.55% at room temperature (maximum allowable: 2%) and 2.09% at el evated temperature (maximum allowable: 5%).

11

Table 4. Compressibility test results

Sample	**Temperature (°C)**	**Compression Amount %**	**Standart**
CF-BP (Ceramic fiber)	*23±5*	*1.55*	*Max. %2*
	400±10	*2.09*	*Max. %5*
BP (Reference)	*23±5*	*1.92*	*Max. %2*
	400±10	*2.20*	*Max. %5*

These results indicate that the brake pad exhibits high dimensional stability at room temperature and does not undergo excessive deformation during pressing or under load. The fibrous structures encircle the resin, forming a more cohesive and supportive net work. Accordingly, the findings demonstrate that the pad maintains its compact struc ture even at elevated temperatures, and the tempera-ture-induced deformation remains within acceptable limits. The incorporation of ceramic fibers enhances structural rigid ity by limiting matrix flow under pres-sure, thereby reducing total compressibility. Ad ditionally, the high thermal sta-bility of alumina–silica fibers helps preserve the integ rity of the composite at elevated temperatures, preventing excessive softening of the resin-rich regions.

3.2.3. Wear and Friction Test

Friction and wear tests were carried out to evaluate the performance of the brake pads. Testing was conducted on the Chase apparatus shown in Figure 8, in accordance with SAE J661 and TSE 555 standards. The resulting friction graphs are presented in Figure 8. It was observed that the coefficient of friction remained stable within the range of 0.480 – 0.530, exhibiting no significant fluctuations during thermal cycling.

In particular, the high Fade-II and Recovery-II values indicate that the material main tains stable friction performance even under elevated temperatures [20]. An approxi mate 3% increase in the coefficient of friction was observed with rising temperature. This confirms that the brake pad is resistant to high temperatures and that fade effects remain minimal.

When comparing the ceramic-fiber-reinforced sample (CF-BP) with the reference pad (BP), the CF-BP demonstrated slightly higher friction stability and lower fluctuation amplitude throughout the test cycle. The ceramic fiber contributed to improved thermal resistance, allowing the CF-BP sample to retain its friction level more effectively dur

ing Fade and maintain a faster and more complete recovery. In contrast, the reference pad showed marginally higher fade sensitivity and a slower recovery response, indicat ing that the absence of ceramic fiber reduced its ability to withstand thermal loads.

a)

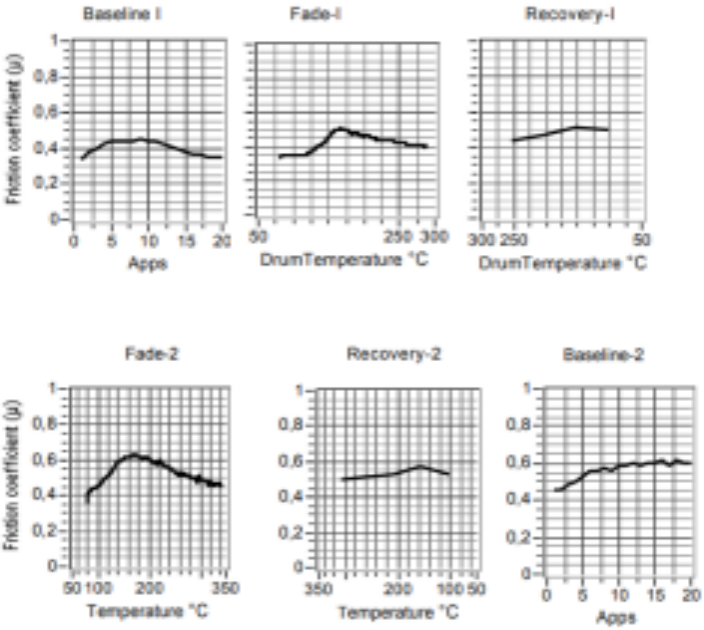
Baseline I
Fade-I
Recovery-I
Friction coefficient (μ)
1
0,8
0,6
0,4
0,2
0
0 5 10 15 20
Apps
50 250 300
DrumTemperature °C
300 250 50
DrumTemperature °C
Fade-2
Recovery-2
Baseline-2
Friction coefficient (μ)
50 100 200 350
Temperature °C
350 200 100 50
Temperature °C
0 5 10 15 20
Apps

b)

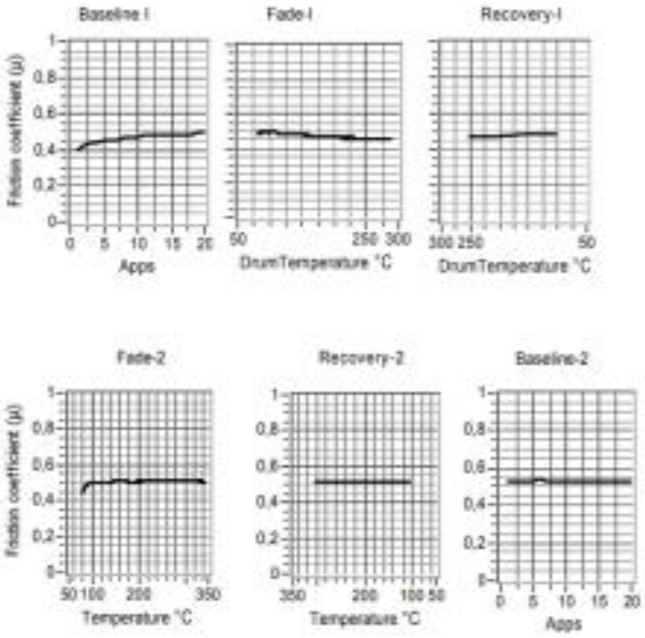

Figure 8. Chase test results of the CF-BP brake pad samples, a) CF-BP (Ceramic fiber - Brake Pad), b) BP (Refence Brake Pad)

According to the results obtained from the SAE J661 test, the friction coefficient was classified using letter designations. For the CF-BP sample, both the cold and hot friction coefficients were rated as "G/G". The G class ($\mu = 0.45–0.55$) indicates high stability, low fade tendency, and reliable braking performance [21].

Dynamometer tests, conducted to evaluate the performance of the brake pads under simulated real vehicle conditions, were performed in accordance with SAE J2522 and ECE R90 standards.

As shown in Figure 9, the test results demonstrate that the CF-BP brake pads exhibit stable performance under various operating conditions. The rapid stabilization of the friction coefficient during the initial and bedding stages indicates that the pad quickly achieves

surface conformity with the disc [22].

Accordingly, the ceramic-fiber-reinforced sample exhibited a stable frictional response, maintaining the coefficient of friction within the narrow range of 0.480–0.530 through out the Baseline, Fade, and Recovery stages, even at elevated temperatures. In contrast, the reference sample demonstrated a more aggressive and fluctuating behavior during the Fade-II stage, where the friction coefficient increased from 0.441 to 0.632 and sub sequently decreased to 0.456. This behavior indicates that the reference pad is unable to preserve frictional stability under thermal loading, whereas the ceramic-fiber-rein forced pad delivers a more controlled and consistent performance due to the stabilizing effect of the ceramic fiber addition.

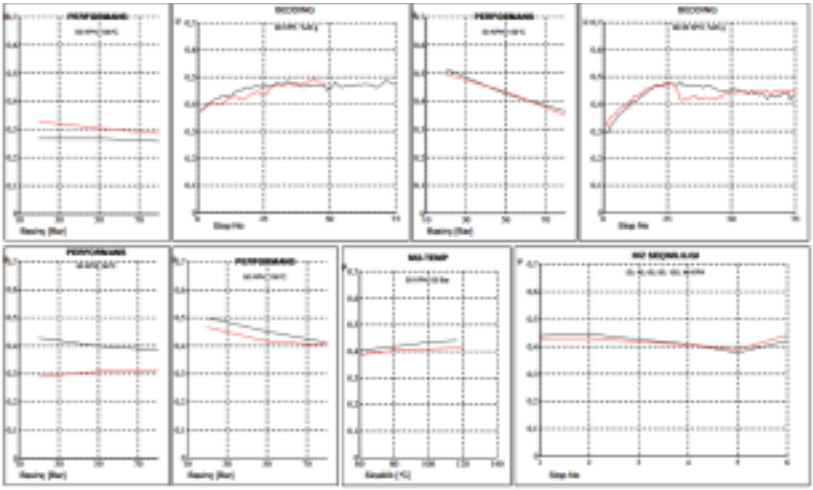

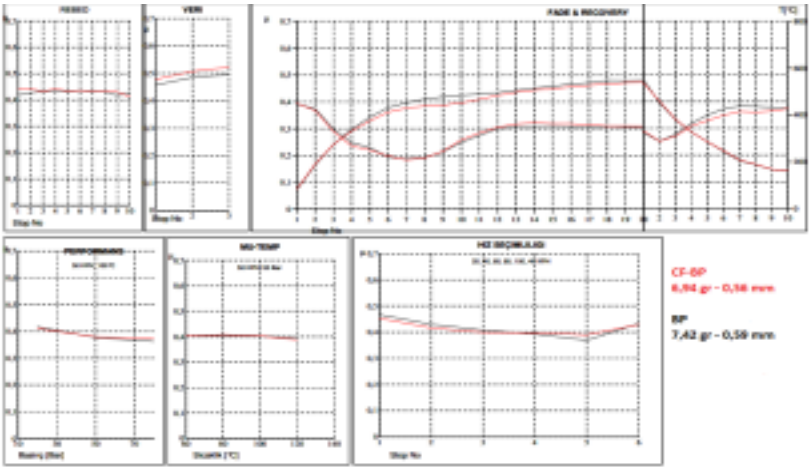

Figure 9. Comparative dynamometer test results of CF-BP and BP samples

The CF-BP sample exhibited superior performance compared to the BP sample in all dynamometer tests. The wear values were measured as 6.94 g and 0.56 mm for CF-BP, whereas the BP sample showed 7.42 g and 0.59 mm, indicating that CF-BP demon strated approximately 7–10% lower wear.

In the fade region, the coefficient of friction for CF-BP showed a more controlled var iation, ranging from 0.32 to 0.46, while BP exhibited a more pronounced drop from 0.48 to 0.30. During the recovery stage, CF-BP rapidly regained performance, increas ing its μ value from 0.46 to 0.55, whereas BP recovered only from 0.38 to 0.44.

Regarding pressure sensitivity, CF-BP maintained μ values between 0.48 to 0.45 in the 50–100 bar range, while BP dropped from 0.45 to 0.38. In terms of temperature sensitivity, CF-BP remained stable with μ values between 0.47 to 0.44 across 60–140 °C,

whereas BP decreased from 0.42 to 0.36. For speed sensitivity, the μ variation for CF BP remained within 0.50–0.46, compared to 0.48–0.40 for the BP sample.

Overall, these numerical comparisons clearly demonstrate that CF-BP offers lower wear, superior fade resistance, faster recovery, and a more stable friction performance under varying pressure, temperature, and speed conditions compared to BP.

3.3. Thermogravimetric Analysis (TGA)

During braking, brake pads are exposed to temperatures ranging from 200 to 600 °C, depending on the vehicle class and operating conditions. TGA is used to determine the temperature at which the material begins to degrade, the amount of weight loss, and its thermal resistance. Therefore, it provides essential insight into whether the brake pad can operate safely at elevated temperatures.

As shown in Figure 10, the ceramic-fiber-reinforced brake pads exhibited a 5.7% mass loss when subjected to temperatures between 0–600 °C.

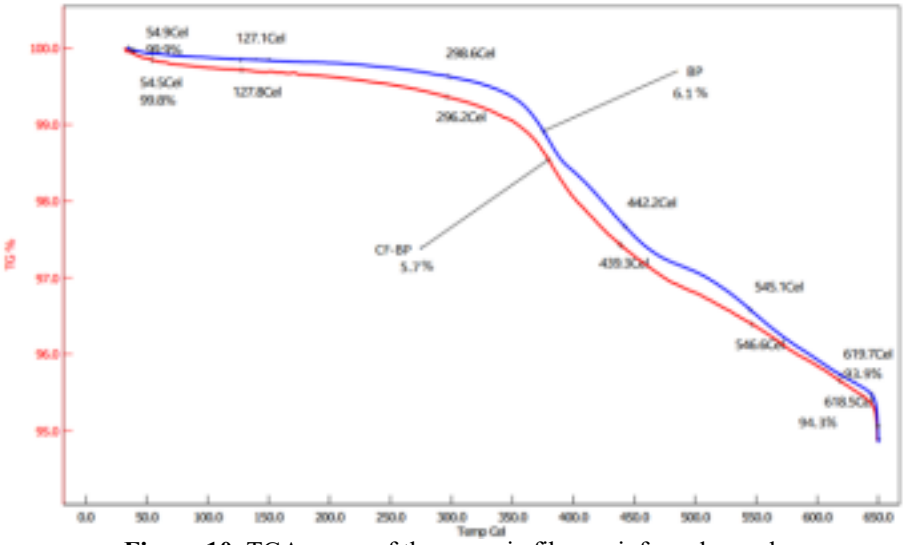

Figure 10. TGA curve of the ceramic fiber–reinforced sample

TGA analysis revealed that the ceramic-fiber-reinforced brake pad exhibits significant thermal stability at elevated temperatures. The mass loss observed up to 200 °C is at

tributed solely to moisture and volatile components and remains minimal. Although binder resins begin to degrade within the 200–400 °C range, the mass loss remains low, and 96.1% of the material is retained at 400 °C. At 600 °C, the total mass loss is only 5.7%, indicating that 94.3% of the material maintains its structural integrity.

16

These findings indicate that ceramic fiber reinforcement imparts dimensional and ther mal stability to brake pads even at high temperatures, thereby supporting reliable brak ing performance [23].

The results of this study are largely consistent with the findings reported in the litera ture. Menon and Pillai (1996) stated that friction materials typically exhibit 5–10% mass loss in TGA analyses at elevated temperatures. In the present study, the ceramic fiber-reinforced brake pad showed a total mass loss of 5.7% up to 600 °C, aligning with the lower bound of the reported range and confirming the stabilizing effect of ceramic fibers on thermal behavior.

4. Conclusion

In this study, two different composite brake pads one standard and the other reinforced with ceramic fibers as an additive were produced using the powder metallurgy method. Three brake pads were manufactured for each test, and the average values of the test results were used for comparative evaluation. It was determined that the ceramic fiber

reinforced pads exhibited improved thermal resistance, as well as enhanced mechanical and tribological properties, compared to the standard pads. These findings suggest that ceramic fibers can be considered a viable alternative additive material for brake pad formulations. The comparative results obtained are summarized as follows:

- According to density measurements based on the Archimedes principle, the addition of ceramic fibers reduced the brake pad density by approximately 5%. This reduction indicates that the overall mass of the vehicle component may be slightly decreased.
- Internal shear strength tests performed in accordance with ISO 6312 revealed that the ceramic fiber-reinforced pads exhibited approximately 52% higher shear strength than the reference pads.
- Based on compressibility test results, both types of brake pads were found to comply

with the acceptable ranges defined in ISO 6310. Additionally, ceramic fiber reinforcement was observed to reduce the amount of compression (see Table 4). This outcome may be interpreted as an indication of extended poten

tial service life for the ceramic fiber-reinforced pads compared to the reference samples.

- Tribological test results demonstrated that ceramic fiber-reinforced brake pads exhibited 7–10% lower wear rates and a more stable tribological performance relative to standard pads.

Overall, the observed reduction in density, coupled with improvements in mechanical and tribological properties, indicates that the incorporation of ceramic fibers can offer significant advantages for heavy-duty brake pad applications.

References

[1] Blau, P. J.: Friction brake materials and their additives, ORNL, (2001)

[2] Eriksson, M., Bergman, F., Jacobson, S.: Tribological contact in automotive brakes, Wear, 252, 26–36, (2002).

[3] Chan, D., Stachowiak, G. W.: Review of friction material technologies. J. Automo bile Engineering, 218, 953–966, (2004).

[4] Cho, M. H. et al.: Effect of ingredient proportions on friction behavior. Tribology International, 41, 1330–1340, (2008).

[5] Bijwe, J.: Developments in fiber-reinforced friction composites. J. Reinforced Plas tics & Composites, 15, 745–754, (1996).

[6] Kim, S. J., Jang, H.: Friction and wear of materials containing ceramic fibers. Wear, 251, 1484–1491, (2001).

[7] Mutlu, I., Eldogan, O., Findik, F.: Effect of various fibers on friction materials. Tri bology International, 44, 667–673, (2011).

[8] Kchaou, M. et al.: Tribological response of ceramic-fiber-reinforced pads. Materials & Design, 52, 533–540, (2013).

[9]Kukutschová, J. et al.: Nano-sized emissions from brake wear. Environmental Pol lution, 159, 998–1006, (2011).

[10] Hull, D., Clyne, T. W.: An Introduction to Composite Materials, Cambridge Uni versity Press (1996).

[11] Agarwal, B. D.: Analysis and Performance of Fiber Composites 3rd Ed., (2006).

[12]Jang, H.: Friction and Wear of Friction Materials Containing Mullite and Glass Fi bers, Wear, 251, 1484–1491 (2001).

[13] Mutlu, I., Eldogan, O., Findik, F.: Effect of Various Fibers on Tribological Proper ties, Tribology International, 44, 667–673 (2011).

[14] Kingery, W. D., Bowen, H. K., Uhlmann, D. R.: Introduction to Ceramics, 2nd Ed., Wiley, (1976).

[15] Varshneya, A. K.: Fundamentals of Inorganic Glasses. Academic Press, (1994). [16] Schneider, H., Okada, K., Pask, J. A.: Mullite and Mullite Ceramics. Wiley-VCH, (1994).

[17] Richerson, D.W.: Modern Ceramic Engineering, (1982).

[18] Kim, S. J., Jang, H.: Friction and wear of friction materials containing mullite and glass fibers. Wear, 251, 1484–1491, (2001).

[19]Chan D., Stachowiak, G.W.: Review of automotive brake friction materials," Proc. Inst. Mech. Eng., Part D: J. Automobile Engineering, vol. 218, no. 9, pp. 953–966, (2004).

[20] Anoop, S., Natarajan, S., Babu, S.K.: Analysis of factors influencing dry sliding wear behaviour of Al/SiCp–brake pad tribosystem, Materials & Design, vol. 30, no. 9, pp. 3831–3838, (2009).

[21] Algan, İ.B., Kurt, A.: Effects of Borax on the Wear Behavior of Brake Friction Ma terials, Gazi University, Turkey, (2017).

22. Spencer, W.M., Spurgeon, W., Winge, J.: Four tests for consistency of automotive brake linings, SAE Technical Paper 0148-7191, (1966).

23. Menon, R.R., Pillai, C.K.S.: Thermogravimetric analysis of friction materials, Ther mochimica Acta, vol. 285, no. 2, pp. 219–227, (1996).

Design and Characterization of 3D Printed Scafolds Loaded with Colchicum micranthum Extract and Oxaliplatin

Zeynep Ozge Oztaban[1], Sevil Senocak[1], Hasan Ege[2], Aylin Koc[1], Yesim Muge Sahin[1,3], Zeynep Ruya Ege[1]

[1]Department of Biomedical Engineering, Engineering Faculty, Istanbul Arel University, Istanbul, Türkiye

[2]Department of Physiology, Medical Faculty, Istanbul Arel University, Istanbul, Türkiye

[3]Department of Biomedical Engineering, Arel Personalized and Translational Medicine Research Center (ArelPOTKAM), Istanbul Arel University, Istanbul, Türkiye

Abstract: Breast Cancer Treatment faces significant challenges due to systemic toxicity of conventional therapies. This study proposes a novel localized treatment approach using endemic *Colchicum micranthum* (CM) extract loaded onto 3D-printed poly(ε-caprolactone)/polyethylene glycol (PCL/PEG) scaffolds. To support this approach, CM extracts will be comprehensively characterized using high-performance liquid chromatography (HPLC) and Fourier-transform infrared spectroscopy (FTIR) to define their chemical profile and ensure batch-to-batch consistency. In parallel, three-dimensional scaffolds will be fabricated and systematically optimized via extrusion-based additive manufacturing. Process parameters (e.g., nozzle temperature, feed rate, printing speed, and infill geometry) and composition ratios (PCL/PEG) will be tuned to achieve target morphological, mechanical, and release characteristics suitable for localized delivery applications.

The proposed study aims to fabricate and evaluate CM-loaded 3D-printed scaffolds for localized breast cancer therapy, with morphological, chemical, and mechanical characterization performed using SEM, FT-IR, HPLC, and DSC. *In vitro* assays will determine sustained drug release kinetics and dose-dependent cytotoxicity via MTT over 72-hour exposure periods, leveraging preliminary evidence that colchicine, the primary bioactive compound in *Colchicum micranthum*, inhibits microtubule polymerization and exhibits significant anticancer potential. This research represents the first demonstration of CM-incorporated scaffolds for breast cancer treatment, offering reduced systemic toxicity through localized delivery, defining dose optimization parameters for clinical translation,

and outlining a commercialization pathway for endemic Turkish flora. By integrating advanced biomaterial design with phytopharmaceutical innovation, this strategy has the potential to replace high-dose systemic chemotherapy while simultaneously contributing to Turkey's bioeconomy.

Keywords: Colchicum micranthum, 3D bioprinting, Local therapy Breast cancer, Polycaprolactone scaffolds.

1. Introduction

Breast cancer remains a significant global health problem, ranking as the most common malignancy among women and one of the leading causes of cancer-related mortality. According to the World Health Organization, approximately 2.3 million new cases and 685,000 deaths were reported worldwide in 2020 [1]. Although advances in diagnostic and therapeutic approaches have improved survival rates, particularly in developed countries, incidence and mortality continue to rise in regions with limited access to early screening and treatment [2]. Current treatment strategies primarily rely on surgery, radiotherapy, and systemic chemotherapy; however, conventional chemotherapeutic agents such as oxaliplatin (OX) and doxorubicin offer only partial tumor regression (30–60% in advanced stages) and are associated with severe systemic toxicities, including cardiotoxicity, nephrotoxicity, and bone marrow suppression [3]. Additionally, the emergence of intrinsic and acquired resistance mechanisms significantly reduces treatment efficacy [4].

These limitations have accelerated research on alternative or complementary therapeutic options, with particular attention to natural bioactive compounds. Medicinal plants are known to contain diverse molecules with cytotoxic, antioxidant, and antiproliferative properties, making them attractive candidates for cancer therapy. Among these, *Colchicum micranthum* (CM), an endemic species in Turkey, has gained interest due to its high colchicine content (12.7 ± 0.8 mg/g) and reported antiproliferative effects [5]. Colchicine is a microtubule-disrupting alkaloid capable of inducing apoptosis; however, its clinical use is limited by rapid metabolism and severe systemic side effects when administered freely [6].

Recent advancements in biomaterials and additive manufacturing have introduced localized drug delivery systems designed to overcome these limitations. Polymeric scaffolds fabricated by extrusion-based 3D bioprinting, particularly those composed of poly(ε-caprolactone) (PCL) and polyethylene glycol (PEG), exhibit desirable features such as tunable porosity (200–300 μm), mechanical stability, controlled degradation, and the ability

to sustain the localized release of therapeutic agents [7]. Such systems can minimize systemic toxicity while enhancing drug concentration at the tumor site. While several plant-derived extracts have been successfully incorporated into polymeric matrices, the integration of *C. micranthum* into 3D-printed scaffolds for localized breast cancer treatment has not yet been reported.

This study aims to develop CM-loaded PCL/PEG scaffolds as an implantable platform for localized chemotherapy. The scaffolds are engineered for controlled, pH-responsive release of CM extracts to mitigate systemic toxicity while supporting antitumor-relevant performance in localized delivery settings. Leveraging our HPLC profiles of Colchicum micranthum (CM) extracts, we highlight the presence and relative abundance of bioactive alkaloids associated in the literature with anticancer activity. These chromatographic fingerprints are used to standardize batches and to underpin claims of antineoplastic potential without presenting cellular efficacy data. In parallel, oxaliplatin (OX) is employed as a positive reference: its release behavior from matched PCL/PEG matrices and its stability characteristics are benchmarked against CM-loaded constructs. Comparative analyses focus on: (i) quantified payload content and batch-to-batch consistency (HPLC area/assay), (ii) release kinetics and pH-responsiveness, and (iii) projected exposure profiles relevant to localized chemotherapy. Furthermore, the approach aligns with the current paradigm of precision oncology, offering targeted therapy that reduces drug dosage requirements by up to 40–60% without compromising healthy tissue viability [8].

2. Materials and Methods

2.1 Materials

Poly(ε-caprolactone) (PCL, average Mn 80,000, Sigma-Aldrich, St. Louis, USA) and polyethylene glycol (PEG, average Mn 3,350, powder form, Sigma-Aldrich, St. Louis, USA) were used as polymeric materials. Chloroform (CAS: 67-66-3) and ethanol (99% purity) were employed as solvents. Colchicum micranthum (CM) bulbs were collected from endemic regions in Turkey and stored at –20 °C until use. All other chemicals were of analytical grade. Human breast cancer cell line MCF-7 was obtained from ATCC for *in vitro* studies.

2.2 **3D Scaffold Production**

The scaffold design was created in SolidWorks with dimensions of 20 mm × 20 mm × 1 mm and a square configuration consisting of seven layers. The final design was converted into G-codes using Simplify3D software. Scaffold fabrication was performed using an extrusion-based 3D bioprinting system (AXO C3, AXO Industries, Türkiye).

The printing process was carried out under controlled laboratory conditions. An extrusion-based pneumatic dispensing system was used with a standard bioprinting nozzle (22–27G range). During fabrication, typical bioprinting parameters such as printing pressure, printing speed, and layer height were adjusted according to the rheological properties of the bioink to ensure stable filament formation and uniform layer deposition. Both nozzle and print bed temperatures were maintained at ambient conditions, as no active thermal control was required for this bioink formulation. Scaffold structures were printed with a grid-type infill pattern commonly used for tissue engineering constructs.

To prepare the printing ink, Polycaprolactone (PCL) and Polyethylene glycol (PEG) were dissolved in chloroform at a PCL:PEG weight ratio of 9.5:0.5 (w/w). The polymer concentration was adjusted to 15% (w/v). Preliminary experiments were conducted with these PCL/PEG composite solutions to determine the optimal printing conditions. Printing parameters, including printing speed, extrusion flow rate, infill density, and total layer count, were systematically optimised to obtain stable printing filaments and scaffolds with well-defined pore structures that do not collapse.

Separately, an extract of the Colchicum (CM) plant was prepared and lyophilized to yield a powdered sample, which was subsequently incorporated into PCL/PEG scaffolds at varying loadings. Briefly, CM bulbs were collected, cleaned, and dried, then milled to a fine powder. The powder was subjected to solvent extraction (e.g., ethanol, methanol, or water) under controlled conditions, followed by filtration to remove particulates. The resulting filtrate was concentrated by solvent removal, using rotary evaporation or freeze-drying, to obtain the crude CM extract.

To ensure that CM did not exhibit cytotoxic effects at the cellular level, dose optimization was performed using the MTT assay, with cell viability calculated relative to untreated controls and dose–response curves established. Following dose determination, CM extract and OX were separately incorporated into 3D-printed PCL/PEG scaffolds at approximately corresponding concentrations under optimized printing conditions. In vitro release studies in phosphate-buffered saline (PBS, pH 7.4) demonstrated gradual and sustained release for both agents, confirming that the polymeric scaffolds support controlled delivery over an extended period while maintaining compound stability.

2.3 **Preparation of CM Extract**

The bulbs of *Colchicum micranthum* (CM) used in this study were collected from local natural populations and processed immediately upon arrival at the laboratory. The plant material was first washed with copious amounts of distilled water to remove soil and debris, then dried on filter paper to eliminate surface moisture. To prevent the degradation of structural components, the cleaned samples were air-dried for several days in a ventilated environment at room temperature (approximately 25 °C), protected from direct sunlight, until a constant weight was achieved.

The completely dried bulbs were ground in a mechanical grinder to obtain a homogeneous particle size. The resulting powdered samples were stored in airtight, light-proof containers to protect them from moisture and oxidative degradation.

For the extraction phase, a specific amount (e.g., 10 g) of CM powder was dissolved in dimethyl sulfoxide (DMSO), a high-polarity solvent, to enhance the solubility of biologically active components. DMSO was selected because the majority of alkaloids, flavonoids, and phenolic compounds found in *Colchicum* species exhibit high solubility in this solvent [9]. The mixture was stirred magnetically for 24 hours at a constant room temperature (approximately 25 °C) to ensure complete dissolution and maximum extraction.

At the end of the extraction period, the mixture was filtered to remove plant residues. The resulting filtrate was evaporated slowly under reduced pressure at temperatures below 40 °C using a rotary evaporator to remove the solvent and concentrate the extract. The concentrated extract was then subjected to lyophilization using a freeze-dryer to maintain the structural stability of the bioactive components. As a result of this process, a yellowish-brown, fine-textured, and completely dry CM extract powder was obtained. The prepared lyophilized extract was stored in light-proof amber bottles at -20 °C for use in subsequent biological and material applications. All extraction procedures were carried out under controlled laboratory conditions to prevent the effects of moisture and temperature fluctuations

2.4. **Characterizations of the Samples**

The structural and physicochemical properties of the CM extracts and the fabricated scaffolds were evaluated using a comprehensive suite of analytical techniques. High-

performance liquid chromatography (HPLC) was employed to identify and quantify the major bioactive constituents. The analysis was conducted using an Agilent 1260 system (Waldbronn, Germany) equipped with a UV detector set at 278 nm, following a standard validated method for the separation of phenolic compounds and alkaloids.

To examine the surface morphology and microstructure of the extract-loaded PCL/PEG scaffolds, Scanning Electron Microscopy (SEM) was utilized. Images were acquired using an FEI QUANTA 450 FEG ESEM (Thermo Fisher Scientific, USA) microscope operating at an accelerating voltage of 10–20 kV. Prior to imaging, the non-conductive scaffold samples were sputter-coated with a thin layer of gold to enhance conductivity and image quality.

Fourier Transform Infrared Spectroscopy (FTIR) was performed to investigate the functional groups and potential chemical interactions between the bioactive agents and the polymer matrix. Spectra were recorded using a PerkinElmer Spectrum Two spectrometer (Waltham, MA, USA) in the range of 4000–400 cm^{-1}.

Additionally, UV–Vis spectroscopy was utilized to determine the absorption profiles of the extracts and to confirm drug loading. Measurements were carried out using a JASCO V750 spectrophotometer (Jasco Corporation, Tokyo, Japan). Absorbance values were recorded at characteristic wavelengths of 265 nm for CM and 260 nm for OX using quartz cuvettes.

Figure 1. Schematic overview of the study workflow. The figure illustrates:(i) preparation and lyophilization of Colchicum extract; (ii) formulation of PCL/PEG composite solutions; (iii) 3D scaffold fabrication by extrusion-based 3D printing.

The release kinetics of the active substances from the scaffolds were meticulously investigated in phosphate-buffered saline (PBS, pH 7.4) at 37 °C to simulate physiological conditions. Our study involved three distinct scaffold groups: 0.4 CM, 0.1 CM, and 0.3

Oxaliplatin (OX). The release assay was conducted at predefined time points: 0 min, 15 min, 30 min, 1 h, 2 h, 21 h, and 24 h . At each point, a specific volume of the medium was withdrawn and immediately replaced with fresh PBS to maintain sink conditions and constant volume.Samples were analyzed using UV–Vis spectrophotometry. Calibration curves were established using stock dilutions of CM and OX 1 mg/mL, and analyte concentrations were determined via linear regression (y = mx)exhibiting high linearity (R^2 > 0.99). The theoretical drug loading quantity in each scaffold was determined based on the assumption of complete absorption and solvent evaporation of the precise volume 100 µL of the standardized stock solution pipetted onto each scaffold.Prior to scaffold fabrication, the cytotoxicity of the CM extract was evaluated on MCF-7 cells via the MTT assay. Cells were subjected to increasing concentrations of the extract for 24 hours to 48 hours, followed by the addition of the MTT solution. Viable cells reduced the MTT to insoluble purple formazan crystals, which were then solubilized and quantified spectrophotometrically at 570 nm. The IC_{50} value for CM was calculated from this resulting data.[10]

In contrast, no separate MTT assay was performed for the reference drug, OX; instead, its final scaffold loading concentration was strategically chosen based on a comparative analysis with the determined IC_{50} of CM and relevant literature data, ensuring therapeutic relevance without inducing excessive cytotoxicity.[11]

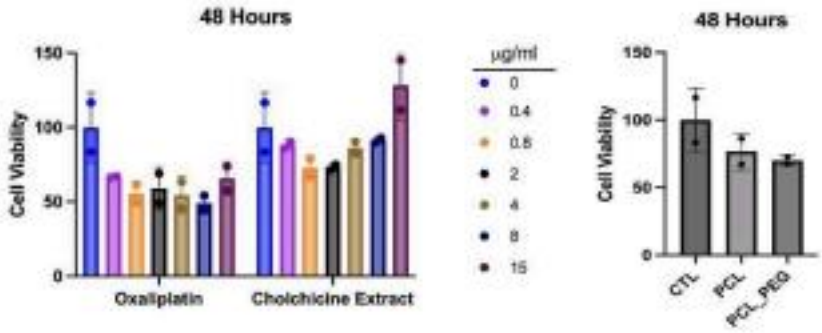

Figure 2. Cell viability of MCF-7 cells after 48 h treatment with different concentrations of oxaliplatin and colchicine extract (left), and effects of scaffold groups (CTL, PCL, PCL–PEG) on cell viability (right).

3. **Results and Discussion**

3.1 High-Performance Liquid Chromatography (HPLC)

The HPLC chromatogram of the CM extract at 278 nm displayed multiple peaks corresponding to phenolic constituents. Based on comparison with external standards run under identical chromatographic conditions, the following compounds were identified: epicatechin, caffeic acid, p-hydroxybenzoic acid, p-coumaric acid, ferulic acid, rutin, and cinnamic acid (Table 1). Among these, p-hydroxybenzoic acid, epicatechin, and rutin were the most abundant components, whereas ferulic acid and p-coumaric acid were present at lower levels.

In addition to the identified phenolic compounds, several peaks remained unassigned, indicating the presence of other phenolics and secondary metabolites in the complex CM extract. Although structural elucidation of these signals was beyond the scope of the present study, their occurrence underscores the chemical diversity of the extract and warrants targeted follow-up using co-injection with additional standards and/or hyphenated techniques [12]. for definitive characterization.

Phenolic acids and flavonoids are well known for their antioxidant properties and free-radical scavenging capacity in vitro, which can contribute to cytoprotective and potential anticancer effects [13]. Consistent with prior phytochemical investigations of Colchicum micranthum, our HPLC profile reveals a phenolic-rich composition with both benzoic and cinnamic acid derivatives as well as flavonoid aglycones/glycosides, aligning with previously reported patterns for this species and related taxa [14]. The quantitative profile obtained in this study aligns with previous phytochemical investigations of the genus *Colchicum*, which have

consistently reported the presence of tropolone alkaloids, particularly colchicine, alongside a rich content of phenolic acids and flavonoids such as caffeic acid, p-coumaric acid, and rutin **[10]**. These bioactive secondary metabolites are well-documented for their potent antioxidant and cytotoxic properties, supporting the therapeutic potential observed in the specific *Colchicum micranthum* extracts used in this research.[15]

Sample	p-hydroxy benzoic acid (µg/g)	Epicatechin (µg/g)	Rutin (µg/g)	Caffeic acid (µg/g)	Cinnamic acid (µg/g)	p-coumaric acid (µg/g)	Ferulic acid (µg/g)
CM extract	203,21	28,71	27,35	1,84	7,93	0,71	5,7

Table 1. Distribution and concentrations of phenolic compounds identified in Colchicum micranthum extract

3.2 UV-Vis Calibration and Validation for CM Extract

The UV-Vis absorbance spectra (Figure X) revealed the characteristic bands of CM extract, while the calibration curve (Figure Y) confirmed the linear relationship between concentration and absorbance with high accuracy. These findings enhanced the reliability of quantitative results obtained by HPLC and highlighted the complementary nature of both analytical techniques.

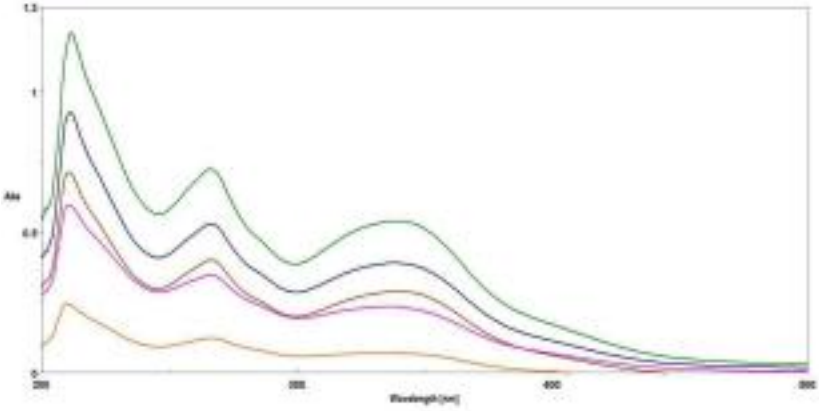

Figure 3. Overlay UV–Vis spectra of CM extract (200–500 nm) at decreasing concentrations, from 1.0 mg/mL to 0.2 mg/mL (top to bottom). The spectra show composite bands at ~210–230 nm, ~260–280 nm, and ~320–360 nm, with absorbance decreasing proportionally to dose.

The overlaid UV–Vis spectra (200–500 nm) exhibit three composite bands: a strong π→π* transition at 210–230 nm, a prominent band around 260–280 nm (including 278 nm used for quantification), and a broader feature at 320–360 nm attributable to cinnamic acid

derivatives and flavonoids. These bands reflect aggregated chromophoric contributions rather than individual compounds; hence, multiple HPLC peaks correspond to only a few UV–Vis bands. Quantification at 278 nm primarily captures abundant constituents (e.g., p-hydroxybenzoic acid, epicatechin, rutin), whereas less abundant species (e.g., ferulic and p-coumaric acids) contribute more to the longer-wavelength band.

3.3 Scanning Electron Microscopy (SEM)

The morphological evaluation of optimized PCL/PEG(9.5/0.5 ml), PCL/PEG/CM(9.5ml/0.5ml/0,3 mg/ml) and PCL/PEG/OX(9.5ml/0.5ml/0,4 mg/ml) 3D-printed scaffolds was performed using scanning electron microscopy (SEM). Prior to imaging, scaffold samples were sputter-coated with a thin layer of gold to enhance conductivity. SEM

micrographs allowed visualization of pore distribution, interlayer deposition, and surface characteristics. In Figure X, across all groups (PCL/PEG,

PCL/PEG/OX, and PCL/PEG/CM), grid-like print fidelity was preserved in the SEM micrographs, as evidenced by orderly interlayer deposition and intact filament junctions, indicating effective optimization of the extrusion parameters.

Additionally, the seven-layer architecture was built in a stacked configuration without signs of sagging or layer collapse. Successive filaments were laid directly on top of each other while maintaining consistent strand width and interfilament spacing, resulting in uniform interlayer fusion throughout the construct.

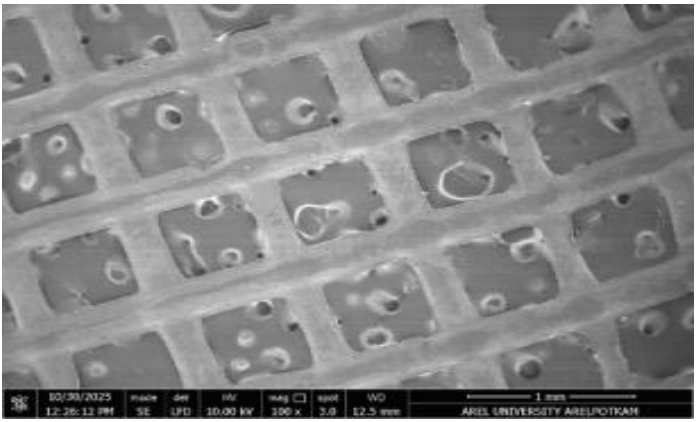
10/30/2025
12:26:12 PM
SE
LFD
10.00 kV
100 x
3.0
12.5 mm
1 mm
ARIEL UNIVERSITY ARIELPOTIKAM

(a)

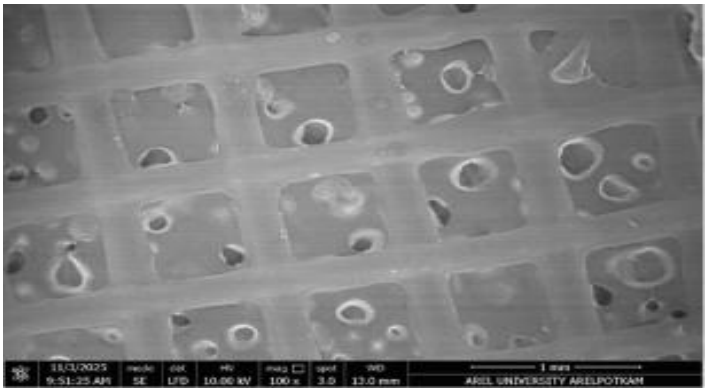
11/3/2025
9:51:25 AM
SE
LFD
10.00 kV
100 x
3.0
13.0 mm
1 mm
ARIEL UNIVERSITY ARIELPOTIKAM

(b)

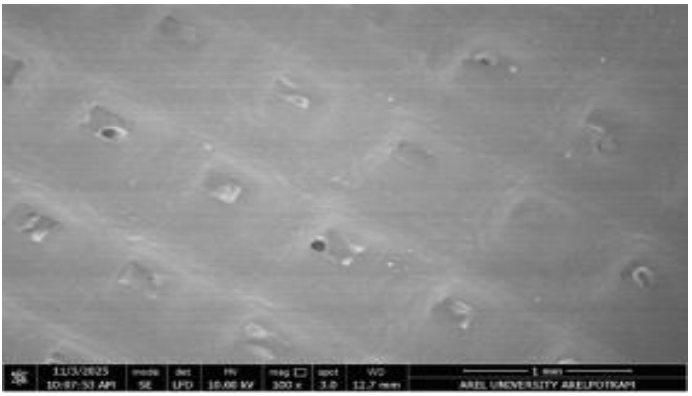
11/3/2025
10:07:53 AM
SE
LFD
10.00 kV
100 x
3.0
12.7 mm
1 mm
ARIEL UNIVERSITY ARIELPOTIKAM

(c)

Figure 4. SEM images of PCL/PEG(a), PCL/PEG/OX(b), and PCL/PEG/CM(c) scaffolds at different magnifications

3.4 Fourier Transform Infrared Spectroscopy (FTIR)

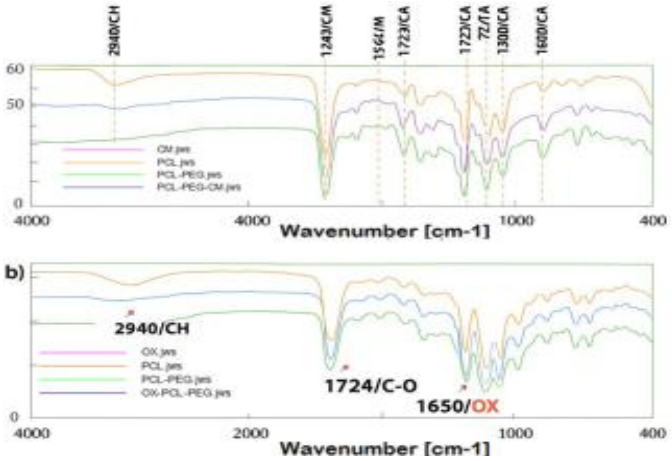

Figure 5. FTIR spectra of Colchicum micranthum extract (CM), oxaliplatin (OX), PCL, PCL/PEG, and their composite formulations.

While FTIR spectroscopy identified characteristic functional groups, the spectral overlap between the polymer matrix and the loaded agents resulted in visually similar patterns. To statistically confirm the successful encapsulation of drugs within the scaffolds, Root Mean Square Error (RMSE) analysis was conducted. This method quantifies the spectral deviation between the pure PCL/PEG scaffold and the drug-loaded forms through linear regression.

In this approach, the absorbance values of the blank PCL/PEG scaffold were plotted against the absorbance of the drug-loaded analogs (PCL/PEG-CM and PCL/PEG-OX). As a baseline, the regression of PCL/PEG against itself resulted in an RMSE value of zero, indicating a perfect linear match. In contrast, as illustrated in Figure 2, the drug-loaded groups exhibited significant deviations from this linearity. Specifically, the analysis yielded RMSE values of 5.12 for PCL/PEG-CM and 3.45 for PCL/PEG-OX. These statistical distinctions ($p < 0.05$) provide quantitative evidence that the chemical environment of the scaffold has been altered by the presence of Colchicum micranthum extract and Oxaliplatin, validating the loading process beyond qualitative observation. [16]

3.4 In Vitro Release Study

Calibration curves established linear relationships between concentration and absorbance for CM and OX, with good fits: CM at 265 nm ($y = 0.6923x + 0.0058$, $R^2 = 0.9666$) and OX at 260 nm ($y = 0.419x + 0.1444$, $R^2 = 0.9425$). Evaluation of Release Kinetics and Structural Considerations: The release studies were conducted using PCL/PEG (9.5:0.5 w/w) composite scaffolds. The quantitative drug loading for each scaffold was determined theoretically by calculating the mass of the active agent contained in the precise volume (100 µL) of the stock solution absorbed by the scaffold structure, assuming complete solvent evaporation and encapsulation.

As observed in the release profiles, the CM extract exhibited a relatively faster and higher cumulative release compared to OX (Figure 4c). This difference can be attributed to the distinct structural and physicochemical properties of the loaded agents. The CM extract is a complex mixture rich in colchicine (an alkaloid) and phenolic compounds, which generally possess relatively low molecular weights and high water solubility. The hydrophilic nature of these components facilitates their rapid dissolution and diffusion from the porous PCL/PEG matrix into the aqueous PBS medium upon hydration of the PEG component [17].

In contrast, Oxaliplatin is a platinum-based coordination complex containing a 1,2-diaminocyclohexane carrier ligand. Although it is polar, its water solubility (approximately 6 mg/mL) is significantly lower than that of the highly soluble components found in the CM extract [18]. Consequently, the release of OX is restricted by its slower dissolution rate within the scaffold channels, leading to a more sustained release profile compared to the rapid diffusion observed with the plant extract.

In vitro release experiments were performed using three distinct scaffold groups, defined by the mass of drug loaded per unit mass of the scaffold (average scaffold mass: 9 mg). The groups were: (i) Low-dose CM (0.1 mg loading; equivalent to 0.011 mg CM/mg scaffold), (ii) High-dose CM (0.4 mg loading; equivalent to 0.044 mg CM/mg scaffold), and (iii) OX group (0.3 mg loading; equivalent to 0.033 mg OX/mg scaffold). The release studies were conducted in [2 mL] of PBS. As observed, the scaffolds showed sustained, concentration-dependent release. CM exhibited higher cumulative release at the higher loading (High-dose CM ≈ 35% at 2 h and ≈ 67% at 24–25 h) compared to the lower loading (Low-dose CM ≈ 22–30% over the same period). The OX group displayed slower release initially with a marked increase by 24–25 h (≈ 36–40%), indicating controlled and formulation-dependent release kinetics (Figure 6).

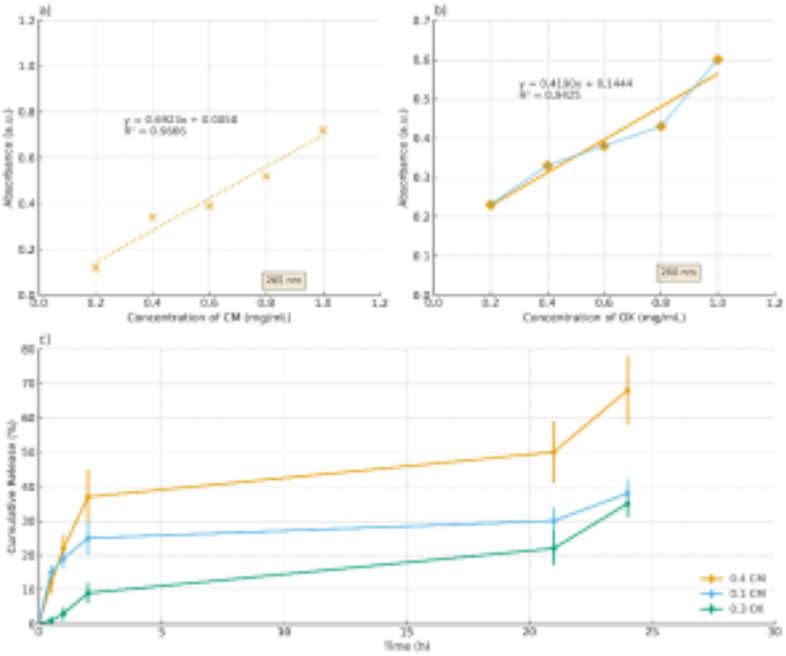

Figure 6.Calibration and release profiles of CM and OX: (a) UV–Vis calibration curve for CM at 265 nm (R^2 = 0.9666); (b) UV–Vis calibration curve for OX at 260 nm (R^2 = 0.9425); (c) cumulative, loading-dependent release from 3D-printed PCL/PEG scaffolds showing sustained delivery and lower initial release for OX relative to CM. The calibration curves confirm reliable UV–Vis quantification for CM and OX, and the release profiles demonstrate sustained, loading-dependent delivery from PCL/PEG scaffolds; oxaliplatin exhibits a lower initial release than CM, likely due to matrix–drug interactions and diffusional constraints. The non-zero intercepts observed in the calibration curves (Figures 6a and 6b) are attributed to minor background absorbance of the solvent matrix and instrumental baseline signals, rather than the presence of the analyte at zero concentration.

4. Conclusions

This study successfully demonstrated the integration of endemic *Colchicum micranthum* (CM) extract and Oxaliplatin (OX) into PCL/PEG composite scaffolds using 3D bioprinting technology. The findings highlight three key outcomes: (1) the successful fabrication of drug-loaded scaffolds with defined structural integrity; (2) a sustained release profile for both agents over 24 hours, facilitated by the hydrophilic nature of the matrix; and (3) significant cytotoxic efficacy against MCF-7 breast cancer cells, suggesting that CM-loaded scaffolds could potentially allow for dosage reduction compared to conventional chemotherapy alone.

However, this study has certain limitations that must be acknowledged. First, the drug release behavior was monitored for a relatively short duration (24 h); long-term release kinetics remain to be investigated. Second, while FTIR analysis confirmed the presence of the components, it did not provide definitive evidence of specific chemical bonding between the drugs and the polymer matrix, suggesting primarily physical entrapment. Finally, the therapeutic efficacy was restricted to *in vitro* experiments on a single cancer cell line. Future studies should focus on extending the release period, conducting comprehensive structural analyses to elucidate polymer-drug interactions, and validating the safety and efficacy of these scaffolds using *in vivo* animal models and healthy cell lines to confirm selectivity and biocompatibility.

Acknowledgements

We would like to express our sincere gratitude to our supervisor for their guidance and support throughout this study. We are also thankful to each other for the laboratory assistance and valuable ideas. This research was supported by TÜBİTAK 2209-A – Research Project Support Programme for Undergraduate Students (Project No: 1919B012327911).

5. **References**

[1]. World Health Organization. (2021). *Breast cancer.* Retrieved August 25, 2025, from https://www.who.int/news-room/fact-sheets/detail/breast-cancer

[2]. Sung, H., Ferlay, J., Siegel, R. L., Laversanne, M., Soerjomataram, I., Jemal, A., & Bray, F. (2021). *Global cancer statistics 2020: GLOBOCAN estimates of incidence and mortality worldwide for 36 cancers in 185 countries. CA: A Cancer Journal for Clinicians*, 71(3), 209–249.

[3]. Tacar, O., Sriamornsak, P., & Dass, C. R. (2013). *Doxorubicin: An update on anticancer molecular action, toxicity and novel drug delivery systems. Journal of Pharmacy and Pharmacology*, 65(2), 157–170.

[4]. Holohan, C., Van Schaeybroeck, S., Longley, D. B., & Johnston, P. G. (2013). *Cancer drug resistance: An evolving paradigm. Nature Reviews Cancer*, 13(10), 714–726.

[5]. Ozturk, Y., & Ayar Kayali, H. (2020). *Phytochemical analysis and colchicine content of Colchicum micranthum Boiss. Natural Product Research*, 34(4), 498–503.

[6]. Kavalalı, G. (2014). *Bitkisel aktif madde olan kolşisin'in etnofarmakolojik yönden değerlendirilmesi [Ethno-pharmacological approach to the plant origin drug 'Colchicine']*. *Lokman Hekim Journal, 4*(1), 16-18.

[7]. Malda, J., Visser, J., Melchels, F. P., Jüngst, T., Hennink, W. E., Dhert, W. J., ... & Groll, J. (2013). *Engineering hydrogels for biofabrication. Advanced Materials*, 25(36), 5011–5028.

[8]. Langer, R., & Peppas, N. A. (2020). *Advances in biomaterials, drug delivery, and bionanotechnology. AIChE Journal*, 66(4), e16825.

[9]. Senizza, B., Rocchetti, G., Okur, M. A., Zengin, G., Yıldıztugay, E., Ak, G., ... & Lucini, L. (2020). Phytochemical profile and biological properties of Colchicum triphyllum (Meadow Saffron). *Foods*, *9*(4),457.

[10]. Alali, F. Q., El-Alali, A., Tawaha, K., & Moydeh, K. (2008).

[11]. Graham, M. A., Lockwood, G. F., & Greenslade, D. (2000).

[12]. Ganzera, M., & Sturm, S. (2018). Recent advances on HPLC/MS in medicinal plant analysis—An update covering 2011–2016. Journal of Pharmaceutical and Biomedical Analysis, 147, 211-233.

[13]. Zhang, L., Tu, Z. C., Wang, H., Fu, Z. F., Wen, Q. H., & Fan, D. (2015). Metabolic profiling of antioxidants constituents in Artemisia selengensis leaves. Food chemistry, 186, 123-132.

[14]. Fernández-Ochoa, Á., Leyva-Jiménez, F. J., De la Luz Cádiz-Gurrea, M., Pimentel-Moral, S., & Segura-Carretero, A. (2021). The role of high-resolution analytical techniques in the development of functional foods. International journal of molecular sciences, 22(6), 3220.

[15]. Toplan, G. G., Gürer, Ç. U., Mat, A., & Sariyar, G. (2016).

[16]. Menezes, V. D. F., Ferreira, D., de Oliveira, A. E. A., de Menezes, V. D. F., de Melo, L. F., & de Oliveira, A. E. A. (2016). Effect of PLGA and PLGA-PEG on the dissolution profile of oxaliplatin. Polimeros, 26(2), 173-180. https://doi.org/10.1590/0104-1428.2323

[17]. World Health Organization. (2021). *Breast cancer*. Retrieved August 25, 2025.

[18]. Sung, H., Ferlay, J., Siegel, R. L., Laversanne, M., Soerjomataram, I., Jemal, A., & Bray, F. (2021). Global cancer statistics 2020: GLOBOCAN estimates of incidence and mortality worldwide for 36 cancers in 185 countries. *CA: A Cancer Journal for Clinicians, 71*(3), 209–249.

Characterization of Mechanical Properties of Glass Fiber/Talc Reinforced Hybrid Polypropylene Composites

Batuhan Yetişir[1][0009-0003-7506-4391], Emre Döşeyici[1][0009-2225-6257-1233], Mücahit Osman Türkan[1][0009-0002-9056-4012], Mustafa Öncül[1][0000-0002-4441-6353]

[1] Department of Mechanical Engineering, Izmir Katip Celebi University, 35620 Izmir, Türkiye

emre.doseyici@hotmail.com

Abstract. In recent years, mineral-filled composites have gained significant attention in both scientific research and industrial applications, driven by the performance limitations of conventional materials and the rising costs of production. In polymer matrix composites (PMC) mineral additives such as silica, calcium carbonate, talc, glass fiber, and kaolin, offer important advantages, including enhanced wear resistance, high thermal stability, and improved dimensional accuracy. These additives not only improve the mechanical and thermal performance of polymers but also contribute to cost-effective manufacturing processes. In this study, 40 wt.% talc-filled polypropylene (TF40) and 40 wt.% glass fiber-filled polypropylene (GF40) were supplied from TİSAN Engineering Plastics. Hybrid composite specimens were prepared by blending TF40 and GF40 at four different ratios (25%, 50%, 75%, and 100%) using a high speed thermokinetic mixer (Gülnar Machine, Türkiye). The tensile properties of the prepared specimens were evaluated using a universal testing machine (Shimadzu AGS-X 5 kN, Japan) in accordance with ASTM D638 and bending properties were conducted in accordance with ASTM D790 using a universal testing machine (Shimadzu Autograph AGS-X Series, Japan). The tensile strength ranged from 27.6 ± 1.2 MPa to 36.3 ± 7.9 MPa, with the highest value obtained for wt.% 100 TF40. Hybridization improved tensile performance compared to neat GF40, particularly in the wt.%50GF40–wt.%50TF40 configuration (30.1 ± 1.9 MPa). Tensile modulus values were observed between 2171.1 ± 148.6 MPa and 2566.9 ± 216.4 MPa, indicating that modulus was strongly influenced by the dominant matrix/fiber phase ratio. Flexural properties showed a more significant increase through hybridization. Flexural strength increased from 50.0 ± 2.9 MPa wt.% 100 GF40 to a maximum of 61.7 ± 13.9 MPa in SET3. The highest flexural modulus was recorded for the wt.% 75GF40– wt.% 25TF40 hybrid (4150.5 ± 339.3 MPa), suggesting improved stiffness under bending loads with increased GF40 content. Overall, the results indicate that mechanical performance can be TF40 contributes significantly to tensile strength, higher GF40 content enhances flexural stiffness.

Keywords: Hybrid composites, Talc, Glass fiber, Thermoplastic, Mechanical properties.

1 Introduction

Composites

Composite materials constitute a class of engineered materials formed by combining two or more distinct constituents in order to integrate their advantageous properties and offset individual limitations, thereby achieving superior overall performance [1,2]. A key advantage of composite materials lies in their ability to enable the fabrication of lightweight structures that exhibit higher stiffness and durability compared to conventional metallic structures. Owing to these attributes, composites are extensively employed in applications that demand high mechanical performance, particularly in contemporary engineering designs.

In comparison to traditional materials, composite materials generally possess more favorable physical properties. Characteristics such as low density, high specific strength, and enhanced hardness make them advantageous over materials such as metals and wood [3-5]. However, polymers used in composites are often unable to achieve the desired mechanical properties when used in isolation. Therefore, to enhance the strength and load-bearing capacity of a composite, a reinforcing phase is incorporated within a matrix phase. The matrix, which typically constitutes the majority of the composite's volume, serves to delay fracture propagation and inhibit crack formation [6].

The primary function of the matrix is to hold the reinforcement phase together, ensuring structural integrity. The reinforcement phase, embedded within the matrix, provides the composite with enhanced mechanical strength, stiffness, and, in some cases, influence over grain size. The interface between the matrix and reinforcement plays a critical role in ensuring effective bonding between the two phases, thereby enabling efficient load transfer and overall mechanical performance [7,8].

Polymer Matrix Materials

A polymer is composed of long-chain molecules interconnected by strong covalent bonds. A polymeric material is formed through the aggregation of numerous polymer molecules possessing similar chemical structures. Polymers are generally classified into two primary categories: thermoplastics and thermosets (Fig. 1).

In thermoplastic polymers, the molecular chains are not chemically bonded to one another. Instead, they are held together by relatively weak secondary interactions, such as van der Waals forces and hydrogen bonds. These weak intermolecular bonds dissociate upon heating, enabling the material to soften or melt. Upon cooling, the intermolecular bonds are re-established, allowing the thermoplastic to solidify once again. Consequently, thermoplastics can be repeatedly softened by heat, melted, and reshaped [9,10].

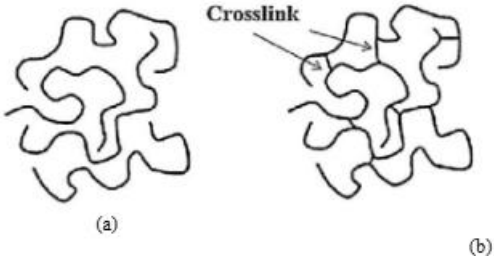

Fig. 1. Bonds of thermoplastic (a) and thermoset (b) polymers [9]*Metal Matrix Materials*

Metal matrix composites (MMCs) offer several advantages, such as enhanced specific strength and modulus, achieved by reinforcing low-density metals like aluminum and titanium. Compared to polymer matrices, most metals exhibit superior mechanical and thermal properties, including higher yield strength, greater density, elevated melting points, and lower coefficients of thermal expansion. The latter can be further reduced by incorporating fibers with inherently low thermal expansion coefficients, such as graphite, into the metal matrix. Moreover, metals retain their durability at elevated temperatures, making MMCs suitable for aerospace, automotive, and other high-performance applications. Common matrix materials for MMCs include aluminum, titanium, and copper.

Table 1. Typical mechanical properties of metal matrix composites [11]

Property	Units	SiC/Al	Graphite/Al	Steel	Aluminum
Specific gravitiy	-	2.6	2.2	7.8	2.6
Young's modulus	GPa	117.2	124.1	206.8	68.9
Ultimate tensile strength	MPa	1206	448.2	648.1	234.4
Coefficient of thermal expansion	µm/m/°C	12.4	18	11.7	23

Ceramic Matrix Materials.
Ceramic matrix composites (CMCs) comprise a ceramic matrix such as alumina, calcium alumina silicate, or silicon carbide, reinforced with fibers like carbon or silicon carbide.

These composites combine the desirable properties of ceramics, such as high-temperature resistance and excellent thermal stability, with reduced brittleness and improved fracture toughness, owing to the reinforcement phase. Additionally, CMCs possess lower density than monolithic ceramics, making them attractive for demanding applications in aerospace, automotive, and energy sectors, where both high-temperature performance and mechanical strength are essential. Ceramics, while offering high hardness and thermal stability, are inherently brittle, exhibiting low fracture toughness and poor resistance to crack propagation. Incorporating reinforcement materials within a ceramic matrix improves its fracture toughness. Among ceramic materials, alumina (Al_2O_3) and mullite (Al_2O_3–SiO_2) are the most widely employed [12]. In composite materials, the matrix phase can exhibit either a continuous or dispersed (second) phase structure. The primary role of the matrix is to bind and hold the reinforcement phase together. The reinforcement phase, in turn, enhances the composite's durability and hardness, while also influencing grain size. An interface exists between the matrix and the reinforcement material, serving to ensure effective bonding and load transfer between the two phases [13].

Hybrid Composites

A hybrid composite is defined as a composite material fabricated by incorporating two or more types of reinforcing agents within a single matrix [14]. The process of hybridization is typically employed to tailor the properties of the constituent materials to meet the specific performance requirements of a given structure, thereby creating a novel composite that retains the complementary advantages of its components while mitigating their inherent limitations [15–19]. Consequently, hybrid composites can, in certain engineering applications, provide more effective solutions than conventional fiber-reinforced composites that utilize a single reinforcement type. Due to their superior balance of mechanical and physical properties, hybrid composites are extensively utilized in various industrial sectors. Notable applications include lightweight structural components for aerospace, automotive, and construction industries, as well as sporting equipment, wind turbine blades, and orthopedic devices [20].

Table 2. Typical mechanical properties of ceramic matrix composites [11]

Property	Units	SiC/LAS	SiC/CAS	Steel	Aluminum
Specific gravitiy	-	2.1	2.5	7.8	2.6
Young's modulus	GPa	89.6	121	206.8	68.9
Ultimate tensile strength	MPa	496.4	400	648.1	234.4
Coefficient of thermal expansion	μm/m/°C	3.6	4.5	11.7	23

Among the various hybrid systems, talc–glass fiber composites are among the most widely implemented. Glass fibers offer high strength and hardness, making them suitable for specialized engineering applications, and they possess a relatively low density compared to many metallic reinforcements. However, their fracture stress and impact resistance are limited, which may be inadequate in applications where the composite is subjected to significant bending or compressive stresses. Conversely, talc fibers exhibit high elongation but lack the strength and stiffness required for demanding structural applications. By integrating these two fiber types within a single composite system, talc–glass fiber hybrid composites can be engineered to achieve an advantageous combination of strength, stiffness, and elongation, thereby enhancing their suitability for high-performance applications.

Fig. 2. Applications of hybrid composites in automotive parts [21]

2 Materials and Methods

2.1 Materials

The materials utilized in this study comprised 40% talc-filled polypropylene (TF40; product code M04000325) and 40% glass fiber-filled polypropylene (GF40; product code M0400001), both supplied by TİSAN Engineering Plastics Company, Türkiye. The typical mechanical and thermal properties of these materials are presented in Table 3.

Table 3. General properties of TF40 and GF40

Property	Units	TF40 Value	GF40 Value	Standard
Density	g/cm^3	1.22-1.28	1.18-1.22	ISO 1183
Tensile modulus	MPa	20000-30000	7000-8000	ISO 527-2
Tensile stress at break	MPa	20-30	85-100	ISO 527-2
Melting temperature	°C	165-170	165-170	ISO 11357
Heat deflection temperature	°C	145	80	ISO 75

2.2 Methods

Manufacturing of Hybrid Composite Processes

Prior to the fabrication of the hybrid composite plates, all constituent materials were conditioned in a laboratory oven at 80 °C for 24 hours to eliminate residual moisture. A laboratory-scale high-speed Gelimat mixer (Gülnar Machine, Türkiye), shown in Fig.3a, was employed for the preparation of composites with a low melting temperature. The total weight of the materials used in each trial is 70 grams. This is because the optimum weight to ensure homogeneous distribution of the material when using a 200 × 200 mm mold is 70 grams. Talc and glass fiber, weighed according to the proportions specified in Table 4, were introduced into the mixer and homogenized for approximately 12 seconds at a processing temperature of around 180 °C. This process yielded a polymer-based paste, which was subsequently placed between two plate molds measuring 200 × 200 mm.

The molten mixture was then subjected to molding using a temperature- and time-controlled laboratory-scale heated–cooled hydraulic press (Gülnar Machine, Türkiye), as shown in Fig.3b, to produce specimens suitable for the planned tests. Upon completion of

the molding process, the composite plates were removed from the press and cut to the required dimensions. The final hybrid composite plates are presented in Fig.4.

Table 4. Specimen mass and percentage

Trial	Material	Talc Fiber (wt %)	Glass Fiber (wt %)	Specimen mass (gram)
SET1	GF40	0	100	70
SET2	TF40	100	0	70
SET3	25GF40 – 75TF40	75	25	17.5 GF40 + 52.5TF40
SET4	50GF40 – 50TF40	50	50	35 GF40 + 35 TF40
SET5	75GF40 – 25TF40	25	75	52.5 GF40 + 17.5 TF40

(a)

(b)

Fig. 3. a. Laboratory-type high-speed gelimat mixer (İzmir Katip Celebi University, Mechanics Laboratory) and b. Laboratory-type heated-cooled hydraulic press (İzmir Katip Celebi University, Material Production Laboratory)

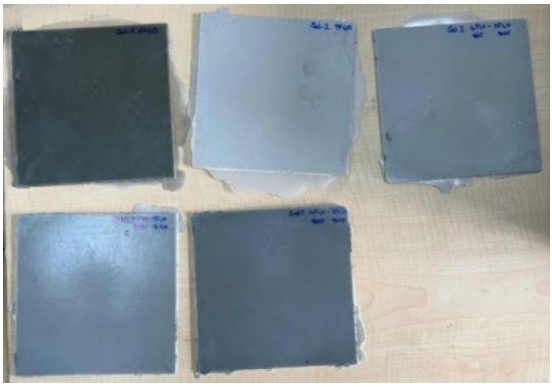

Fig. 4. Hybrid composite plates

Characterization of Hybrid Composites

Tensile Test

Tensile tests were performed on hybrid composites containing talc and glass fiber. All experiments were conducted at room temperature using a SCHIMADZU AGS-X 5 kN universal testing machine (Fig. 5), operating at a crosshead speed of 50 mm/min. For each composite group, five specimens were tested to ensure statistical reliability in the determination of mean values and standard deviations. The yield strength, ultimate tensile strength, and elongation at break were recorded for all specimens.

Fig. 5. A universal tensile test machine (İzmir Katip Celebi University, Mechanical Engineering Laboratories)

Flexural Test

Three-point flexural tests were performed on a universal testing machine (Shimadzu Autograph AGS-X Series universal testing machine, Japan) using the ASTM D-790 standard (Fig. 6). Three-point bending tests were conducted at a support spacing of 32 mm, a bending rate of 1 mm/min, and room temperature. Four specimens were tested from each group.

Fig. 6. A universal flexural test device (İzmir Katip Celebi University, Mechanical Engineering Laboratories)

3. Results and Discussions

Tensile Test Result

The tensile properties of the composites are summarized in Table 5. The SET2 specimen exhibited the highest tensile strength (36.3 MPa), representing a 31.5% increase compared to SET1. Incorporation of GF40 into the TF40 matrix reduced tensile strength: SET3 decreased by 19.8%, SET4 by 17.1%, and SET5 by 16.0% relative to SET2. Regarding tensile modulus, SET3 showed the lowest value, corresponding to approximately a 15% reduction compared to SET1. In contrast, SET5 exhibited the highest modulus, showing a slight 0.4% increase over SET1.

Table 5. Tensile test results

Abbreviation	Specimen concentration	Tensile Strength (MPa)	Tensile Modulus (MPa)
SET1	GF40	27.6 ± 1.2	2556.6 ± 97.9
SET2	TF40	36.3 ± 7.9	2528.4 ± 384.8
SET3	25GF40 – 75TF40	29.1 ± 2.7	2171.1 ± 148.6
SET4	50GF40 – 50TF40	30.1 ± 1.9	2436.9 ± 64.4
SET5	75GF40 – 25TF40	30.5 ± 6.4	2566.9 ± 216.4

Nonetheless, at higher filler loadings, the presence of sharp-edged, irregularly shaped filler particles may induce localized stress concentrations within the matrix under tensile loading. The superior performance of SET5 suggests a synergistic reinforcement effect when GF40 and TF40 are combined in equal proportions. Such improvement may stem from an optimal balance of mechanical reinforcement, improved interfacial bonding, and enhanced load transfer between the matrix and filler particles. Conversely, the inferior performance of SET2 underscores the limitations of TF40 as a sole reinforcing agent, which appears less effective than GF40 in enhancing tensile properties. Overall, the results demonstrate that the combined use of GF40 and TF40 utilizes a significant influence on the mechanical behavior of the material, highlighting the importance of filler composition in composite design. In contrast, talc-filled systems exhibit a different stiffening mechanism. Talc particles increase tensile modulus primarily by restricting polymer chain mobility rather than by direct load transfer. Rothon emphasized that platelet-shaped mineral fillers such as talc enhance stiffness through matrix constraint effects, but do not contribute significantly to tensile strength due to the absence of a continuous reinforcement network [22]. This explains why SET2, despite lacking glass fibers, still exhibits a relatively high tensile modulus, while SET3 shows a reduced modulus compared to fiber-dominated systems. The hybrid composites immediately SET4 and SET5, demonstrate intermediate and more stable tensile strength values, highlighting the synergistic effect of combining fibrous and particulate reinforcements. Hybridization has been shown to mitigate the disadvantages of single-reinforcement systems by balancing stiffness enhancement from fibers and crack-arresting mechanisms from particulate fillers [23,24]. Fu et al. emphasized that properly designed hybrid composites can achieve improved mechanical stability by reducing stress concentration and enhancing damage tolerance [23].

Fig. 8. Specimens after tensile test

Flexural Test Result

The lowest flexural modulus was obtained SET2, the value is nearly 3016 MPa. Whereas the highest value was recorded for the SET5, the flexural modulus value is nearly 4150 MPa. This behavior is consistent with literature reports indicating that the high elastic modulus of glass fibers and efficient stress transfer at the fiber-matrix interface primarily control flexural rigidity in GF/PP systems [25,26]. Hybrid composites exhibited a noticeable synergistic effect on flexural modulus. Compared to the single-filler systems, the incorporation of a limited amount of talc into glass fiber-reinforced PP led to further stiffening of the matrix, likely due to restricted polymer chain mobility and improved stress distribution between fibers. Similar enhancements in flexural modulus for GF-talc hybrid PP composites have been explicitly reported by Morelli et al. [27], who attributed this behavior to improved packing efficiency and reduced local matrix deformation.

Table 6. Flexural test results

Abbreviation	Specimen concentration	**Flexural Strength (MPa)**	**Flexural Modulus (MPa)**
SET1	GF40	27.6 ± 1.2	2556.6 ± 97.9
SET2	TF40	50.0 ± 2.9	3631.8 ± 242.5
SET3	25GF40 – 75TF40	51.3 ± 5.2	3016.2 ± 266.1
SET4	50GF40 – 50TF40	61.7± 13.9	3176.0 ± 1258.4
SET5	75GF40 – 25TF40	60.9 ± 3.2	3340.0 ± 72.4

The bending strength results were examined, the following occurred as shown in Table 6. The lowest flexural strength values were observed for the single-filler systems, with SET1 and exhibiting values of approximately 50-51 MPa. In contrast, hybrid composites showed superior bending strength, with the highest values obtained for SET3, the value is 61.7 MPa and SET4 value is 60.1 MPa. This improvement can be attributed to the combined action of glass fiber bridging and talc-induced crack deflection, which delays crack initiation and propagation under flexural loading [27,28].

Overall, the results indicate that while flexural modulus is mainly governed by glass fiber content, flexural strength is maximized through hybrid reinforcement. Balanced GF40-TF40 ratios provide a more homogeneous stress distribution and enhanced damage tolerance, leading to an improved stiffness-strength balance under bending loads [25-27].

Conclusion

This study investigated the feasibility of developing a novel polypropylene-based hybrid composite through the combined use of glass fiber (GF) and talc fiber (TF). Initially, the mechanical properties of each constituent material were characterized. Subse-quently, matrix composites were fabricated by incorporating GF into TF at weight ratios of 25%, 50%, and 75%. The influence of these compositions on mechani-cal performance was evaluated through tensile and flexural testing.

In tensile loading, SET2 exhibited the highest tensile strength (36.3 MPa), showing a 31.5% improvement compared to the SET1. However, increasing the hybrid filler ratio led to moderate reductions in tensile strength, likely due to stress concentrations induced by irregular particle morphology at higher filler loadings. In terms of tensile modulus, talc-filled systems maintained relatively high stiffness due to matrix constraint effects, while fiber-dominated and hybrid systems provided improved load transfer mechanisms. Notably, the SET5 formulation demonstrated a slight improvement in modulus compared to SET1, suggesting a favorable interaction between fibrous and particulate reinforcements.

Under flexural loading, hybrid composites exhibited superior performance compared to single-filler systems. While flexural modulus was primarily governed by the glass fiber content, flexural strength was maximized in SET3 and SET4, indicating a synergistic reinforcement effect. The combined action of fiber bridging and talc-induced crack deflection contributed to improved stress distribution, delayed crack propagation, and enhanced damage tolerance.

Overall, the findings confirm that hybridization of GF40 and TF40 offers a balanced stiffness–strength performance by integrating the load-bearing capacity of glass fibers with the matrix-restraining effect of talc. Proper optimization of filler ratios enables improved mechanical stability and more homogeneous stress transfer within the composite structure.

Acknowledgements

This work was supported by the Scientific and Technological Research Council of Türkiye (TÜBİTAK) under the 2209-A University Students Research Projects Support Program 2024/1 (Project Number: 1919B012419735).

References

[1] Öncül, M., Atagür, M., Atan, E., & Sever, K. (2025). A preliminary evaluation of bing cherry tree (prunus avium L.) pruning waste as an alternative lignocellulosic filler for lightweight composite material applications. Polymer Composites, 46(4), 3655-3667.

[2] Sever, K., & Yılmaz, M. (2020). Influence of wollastonite hybridization on the properties of artichoke-filled polypropylene composites. Emerging Materials Research, 9(2), 302-307.

[3] Gopinath, A., Kumar, S., Elayaperumal, A.: Experimental investigations of mechanical properties of jute fiber reinforced composites with polyester and epoxy resin matrices. Procedia Engineering 97, 2052–2063 (2014).

[4] Demir, M., Çetin, N., & Narlıoğlu, N. (2025). Comparison of Additive Manufacturing and Injection Molding of Biocomposites Reinforced with Alkali-Treated Wood Flour Derived from Recycled Wooden Pallets. Polymers, 17(15), 2004.

[5] Öncül, M., & Sever, K. (2025). Improvement of Mechanical and Viscoelastic Properties of Polypropylene with Wood and Wollastonite Fillers. Celal Bayar University Journal of Science, 21(1), 60-65.

[6] Ramesh, M., Palanikumar, K., Hemachandra Reddy, K.: Mechanical property evaluation of sisal–jute–glass fiber reinforced polyester composites. Volume 48, 1–9 (2013).

[7] Qu, J.: The effect of slightly weakened interfaces on the overall elastic properties of composite materials. Mechanics of Materials 14(4), 269–281 (1993).

[8] Bozaci, E., Sever, K., Sarikanat, M., Seki, Y., Demir, A., Ozdogan, E., & Tavman, I. (2013). Effects of the atmospheric plasma treatments on surface and mechanical properties of flax fiber and adhesion between fiber–matrix for composite materials. Composites Part B: Engineering, 45(1), 565-572.

[9] Mallick, P.K.: Fiber-Reinforced Composites: Materials, Manufacturing, and Design, 3rd edn., vol. 62. CRC Press, Boca Raton (2007).

[10] Seydibeyoğlu, M. Ö., Dogru, A., Wang, J., Rencheck, M., Han, Y., Wang, L., ... & Gardner, D. J. (2023). Review on hybrid reinforced polymer matrix composites with nanocellulose, nanomaterials, and other fibers. Polymers, 15(4), 984.

[11] Kaw, A.K.: Mechanics of Composite Materials, Second Edition. CRC Press, Taylor & Francis Group, Boca Raton, London, New York (2006).

[12] Khumalo, M.V., Khoathane, M.C.: Effect of mechanical alloying in polymer-ceramics composites. In: First Online Publication, pp. 39–66. (2021).

[13] Seki, Y., Selli, F., Erdoğan, Ü. H., Atagür, M., & Seydibeyoğlu, M. Ö. (2022). A review on alternative raw materials for sustainable production: novel plant fibers. Cellulose, 29(9), 4877-4918.

[14] Hull, D.: An Introduction to Composite Materials. Cambridge University Press, Cambridge (1981).

[15] Gururaja, M.N., Rao, A.N.H.: A review on recent applications and future prospectus of hybrid composites. International Journal of Soft Computing and Engineering (IJSCE) 1(6), 352–355 (2012).

Development of Modıfied Natural Zeolıte Added PVC Surface Coating

Duru ETTERGEN[1], Elif ÖZTÜRK[1], Canan URAZ[1], Didem KALE[1], Yunus Emre DAĞISTANLI[1], Nazmiye YOLDAŞ[1]

[1] Department of Chemical Engineering, Ege University, İzmir, Türkiye

duruettergen@gmail.com

Abstract: Polyvinyl chloride (PVC) is one of the most widely used thermoplastics. Despite its widespread use and various advantages, PVC usage results in significant environmental challenges due to its waste generation. UV exposure and high temperatures can cause degradation and discoloration problems on PVC in long term exposure. As a solution, a natural zeolite clinoptilolite that has high thermal stability, high ion exchange capacity, abundant natural existence, low cost is being used as an additive to PVC paint. In this study, 3 different modification methods are applied to natural zeolite by using lanthanum (III) nitrate, zinc acetate, and magnesium chloride. To apply as a surface coating to PVC, modified zeolites are added into a water-based PVC paint. To evaluate the performance of the coating; UV-aging, degree of blistering and cross-cut tests have been conducted. These tests showed that the developed coating can stick to the PVC surface successfully even when the coating scratches with the external factors. SEM-EDS analysis of modified zeolite samples shows that La modified zeolite gives the most uniform sized and shaped particles compared to other samples and the exchanged ions are present in the modified samples because of the modification process as intended. FTIR-XRD data indicates that there are not any significant structural changes related to the modification process. Compared to traditional UV-stabilizers, modified zeolites may be a better option in terms of higher protectiveness and environmental friendliness. Consequently, lifespan of PVC can be increased by improving its durability with the developed PVC surface paint.

Keywords: [PVC, natural zeolite, clinoptilolite, surface paint, UV-protection]

1. INTRODUCTION

1.1 **PVC**

Polyvinyl chloride (PVC), the better-known and widely used polymer, is a synthetic resin made by polymerization of vinyl chloride monomer (VCM) [1]. Neat PVC polymer is brittle and has limited commercial possibilities. Additionally, processing PVC from raw form by using high temperature and pressure leads to severe degradation of its structure. Therefore, a wide range of additives is incorporated during PVC production, which can improve mechanical properties of PVC products [2]. Apart from additives, titanium dioxide is the crucial pigment for PVC to outdoor use because of its protection properties against UV-radiation. PVC containing TiO_2 degrades much slower under the atmosphere. However, mixing TiO_2 with other pigments may lead to various unexpected effects. For example, anthraquinone pigments combined with high doses of titanium dioxide have undergone a bathochromic shift without even being subjected to light. Polyvinyl chloride (PVC) is a widely consumed plastic material and may lead various environmental pollutions [3]. Plastic additive-related chemicals,particularly in polyvinyl chloride (PVC), have become a key issue in plastic pollution [4]. Although legislation on plastic waste recycling has resulted in increased recycling, plastic pollution is still causing significant biological impact [5].

1.2 **ZEOLITE**

Zeolites are an important class of inorganic crystalline materials with unique structural and chemical properties. Compared to other microporous materials, zeolites differ in structure by being solely built from tetrahedral framework containing Si, Al, P etc. as the central atom that are bonding with 4 oxygen atoms [6, 7]. Owing to that, they can form three dimensional, four-connected zeolite frameworks. The demonstration of zeolite molecular structure is shown in Figure 1. Their properties can also be improved synthetically with modifications to obtain higher adsorption capacity, higher surface activity, large crystal cavity, larger pore size, pore volume and specific surface area [8].

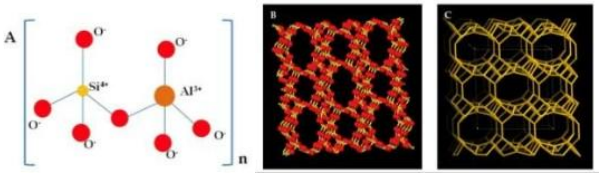

Figure 1. (A) AlO4 and SiO4 tetrahedrons joined by oxygen atoms that constitute the reticular structure of the zeolite. (B) and (C) Clinoptilolite framework type [9]

Clinoptilolite belongs to heulandite group, and it is one of the most abundant

types among other zeolites. Si/Al ratio is also higher in clinoptilolite compared to other types which is an indication of a zeolite's stability. It was also found that heulandite's crystal structure is stable up to temperature 280 □C, while for clinoptilolite it was 700 □C [10, 11]. As a result of these, its high surface area, abundant natural existence, high ion exchange capacity, low cost and one of the most important properties: its recyclability thus sustainability, environmental friendliness makes it an excellent alternative compared to other natural zeolite types [11]. Zeolites also have a potential of application in anticorrosion technologies. Considering that they have remarkable thermal and chemical stability, anti-corrosion coatings which uses these properties of zeolite for its benefit could become an effective and environmentally friendly alternative to chromate-based coatings and holds a potential to reduce the content of phosphate corrosion inhibitors [12]. Even though chromates are being used widely in the industry due to their effectiveness, they are harmful to the environment and are carcinogenic [13]. Therefore, the need for an alternative to these pigments with the same/ better anti-corrosive effects arises. Alternatively, their UV resistance effect is studied by Li et al.[14], and found that in films containing zeolite nanoparticles, an increase in the durability, strength, thermal stability, and UV resistance of the polymer has been observed. These promising findings shows the potential of zeolites when being used as a protective pigment in coatings.

2. MATERIAL AND METHODS

2.1 **Materials**

Clinoptilolite (25 g) from Gordes Zeolite, Manisa, have been used for each modification in three different particle sizes as: 10,50,100-micron. For the solutions used in the modifications; Magnesium chloride hexahydrate (Merck), Zinc acetate (Merck), Lanthanum nitrate-hexahydrate (Sigma-Aldrich), Potassium hexacyanoferrate(ii) (Merck), Ammonium oxalate (Riedel-de-Haën), Sodium acetate, Nitric acid (Sigma-Aldrich) and distilled water are used. To weigh the chemicals, Sartorius BP 221S lab scale digital balance is used. To obtain solutions, DAIHAN Hotplate Stirrer MSH-20D and IKA C-MAG HS7 Hotplate Stirrer are used. Other laboratory equipment used in these

processes are test tubes, filter paper, glass rod, glass beaker, magnetic stirrer bar, funnel, petri dish, laboratory tweezers, spoon.

2.2 **Modification Procedure**

The study aims to find the most effective zeolite size and the modification type on a PVC surface when applied as an anticorrosive paint coating. According to this aim, 3 different modifications are going to be implemented for 3 different particle sizes (10 μm, 50 μm and 100 μm) of natural zeolite clinoptilolite. Zinc Acetate and Magnesium Chloride Modification As the first step, zeolite with 10 μm particle size were weighed to get 25 g. Then the solution is prepared to add the zeolite in where the modification will occur. The solution is prepared by using 375 ml of distilled water and zinc acetate/magnesium chloride to get 0.1 M solution in total. After the solution is ready, weighed zeolite is added to that solution. The formed mixture is stirred for an hour at ambient temperature with the stirrer at 650 rpm, and then the formed paste was filtered using filter papers [15]. Lanthanum (III) Nitrate Modification

In this method, zeolite powder having 10 μm particle size is weighed as the first step. Then it is added to the solution of 0.2 M HNO_3 (nitric acid). The formed mixture is then heated up to the boiling temperature (83 ºC) and kept at that temperature for 1 hour to eliminate ferric compounds by making them react with nitric acid and separate from the zeolite structure. The zeolite was separated from supernatant by filtration (using filter paper) and washed with distilled water several times. Afterwards, the separated and washed zeolite is added to the solution containing 2 mol/L $NaCH_3COO$ (sodium acetate) and stirred for 3 hours continuously to gain Na^+ ions back to the zeolite framework. Then the zeolite was separated by filtration and washed with distilled water. As the last step, the zeolite was exchanged with La (III) ions by bringing it into contact with 0.2 mol/L $La(NO_3)_3$ (Lanthanum (III) nitrate) in 1×10^{-3} mol/L HNO_3. The formed mixture is stirred for 24 hours in total [16]. In both modification types, to assure that there is no more ion exchange can take place, precipitation test is done. For zinc acetate and magnesium chloride, ammonium oxalate gravimetric method is used. In this method ammonium oxalate solution (1 M) is being added to the supernatant after filtration. For lanthanum (III) nitrate modification, potassium ferrocyanide is added to the supernatant. In these methods, solutions will form precipitate if there are any free ions of Mg, Zn or La. So, if the modification process is successful, there shouldn't be any precipitation observed. In our case, there were no precipitation formation which confirmed the completion of the modification process. After the ion-exchanged zeolites are obtained, they are filtered (using filter paper), washed for a few times and dried at room temperature. The resultant dried

ion-exchanged zeolites are then reserved to be used as an additive to the PVC paint. The same procedure is repeated using 50 μm and 100 μm zeolite.

2.3 **Profile Tests**

The following test procedures were applied to evaluate the coating performance and to assess the effectiveness of modified zeolites as alternative pigment materials in PVC paint formulations. The selected tests were incorporated into the experimental plan in accordance with RAL standards, which are widely accepted as the primary reference standards for window profile production and application, including coating and painting requirements. These tests were conducted to characterize adhesion, thermal behavior, and resistance to moisture and elevated temperatures of the developed coatings.

2.3.1 Cross-Cut Test: Cross-cut adhesion tests were performed on all coated specimens to evaluate the bonding strength between the paint layer and the PVC substrate. The tests were carried out in accordance with the EN ISO 2409 standard. In this method, the coated surface was incised using a standardized cutting tool to form a cross-hatched pattern. Subsequently, a standardized adhesive tape was applied over the cut area and left in place for 60 seconds. The tape was then removed in a single motion, and the surface was visually inspected to assess the degree of paint detachment and adhesion performance.

2.3.2 Heat Build-Up Tests: Heat build-up tests were conducted to evaluate the thermal response of the coated profiles under simulated solar radiation. In this analysis, the samples were exposed to a standardized ultraviolet (UV) radiation source in accordance with the EN ISO 16474-2 standard, along with all specified test parameters and environmental conditions. Following 30 minutes of UV exposure, surface temperatures were measured using appropriate temperature measurement devices. This test method is commonly used to assess the surface temperature behavior of coated profiles, which is strongly influenced by the total solar reflectance properties of the coating system. 2.3.3 Boiling Tests: Boiling tests were performed to examine the resistance of the applied coatings to hot water and moisture exposure. The tests were conducted in accordance with the EN 12206-1 standard. As specified in the procedure, painted PVC profiles were immersed in boiling water for a duration of 2 hours. After completion of the test, the profile surfaces were visually examined to identify any signs of surface degradation, such as blistering, bubble formation, or indentations.

3. RESULTS AND DISCUSSION

3.1 **Addition of the Modified Zeolites to the Selected Paint**

Decotone was selected as the water-based white color PVC paint to be applied to the PVC samples. When the modified zeolites were mixed with the water-based PVC paint, the zeolites did not dissolve sufficiently, instead formed agglomerates. As the particle becomes smaller in size, intermolecular forces become more dominant. Especially in solid particles which has a size of below 100 μm, these forces become much more active, and the particles attract each other and stick together, behaving like a cluster. On the other hand, solid particles adsorb water vapor from the air, this allows the particles to stick together, forming agglomerates. The humidity level in the laboratory was not measured during the experiments, and agglomerates may have formed due to the reasons mentioned above.

3.2 **Paint Performance Tests**

Following the application of PVC paints containing modified zeolite additives onto PVC substrates, gloss measurements were conducted using a glossmeter to evaluate the reflective properties of the coated surfaces. Among all samples, the highest gloss values were consistently obtained from surfaces coated with paints containing 100 μm zeolite

particles, regardless of the modification type applied. Apart from this observation, no clear or statistically significant relationship was identified between other sample characteristics and the measured gloss values. In addition to gloss measurements, cross-cut adhesion tests were performed to assess the interfacial bonding between the coating and the PVC substrate. The results indicated that all coatings exhibited satisfactory adhesion, with no evidence of detachment or surface failure. This finding confirms that the incorporation of modified zeolite particles did not negatively affect the adhesion performance of the paint system. However, the blistering test results were unfavorable for all paint formulations, indicating limitations in the resistance of the coatings under blistering conditions.

Cross Cut Test: Cross-cut adhesion tests were carried out in accordance with the EN ISO 2409 standard to evaluate the bonding strength between the paint layers and the PVC surfaces. The test results demonstrated that all specimens showed excellent adhesion performance. No peeling, cracking, or coating delamination was observed on any of the tested surfaces, indicating strong interfacial compatibility between the coating and the

substrate. It was also noted during the application and testing stages that paints containing modified zeolite exhibited higher density, which resulted in increased coating thickness compared to the reference paint without additives. Despite this increase in thickness, no adverse effects such as surface cracking or mechanical damage were detected. All coatings formulated with modified zeolite additives maintained their structural integrity throughout the testing process.

Heat Build Up Tests: The heat build-up (HBU) test results revealed that the variation in surface temperature did not exceed 5% for any of the coatings containing modified zeolite additives. This indicates that the incorporation of modified zeolite materials had a limited but stable influence on the thermal behavior of the coated surfaces. The detailed results of the heat build-up tests are presented in Table 1.

Table 1. HBU test results for Zn, Mg, La modified zeolites in 10, 50 and 100 µm particle size

	Particle Size (µm)	HBU Temperature (°C)
Reference with virgin painting	-10	55
Mg Modified	50	53.5
Mg Modified	100	53.9
Mg Modified	10	54.3
Zn Modified	50	53.7
Zn Modified	100	54.0
Zn Modified	10	54.2
La Modified	50	53.2
La Modified	100	53.6
La Modified		53.8

Overall, the HBU test results suggest that the addition of modified zeolites with different particle sizes slightly improved the surface heat management performance of the coatings. Although the enhancement was modest, the presence of modified zeolite particles contributed to a more consistent thermal response under the applied test conditions.

Boiling Tests

Boiling tests were conducted on PVC profiles coated with paints containing modified zeolite particle additives to evaluate their resistance to moisture and elevated temperatures. After completion of the boiling test, the surfaces of the coated profiles were examined in accordance with the EN 12206-1 standard. Visual inspection revealed the formation of bubbles on the painted surfaces. The observed blistering behavior is

considered expected, as similar bubble formation was also detected on profiles coated with virgin paint formulations without any additives. Based on these observations, it was concluded that the moisture and temperature resistance of the coating system itself is insufficient to fully meet the requirements specified in the EN 12206-1 standard. FTIR Results

The small peak that can be observed in all the samples around the wavenumber 3600, is a representation of the H_2O presence in the samples [17]. There is not any significant difference in the height of that peak between the modified and the unmodified samples, so the water absorbance does not change in the modification process. The second peak that can be observed in all the samples around 1630 cm^{-1}, refers to the water molecules connected with Na and Ca [18]. Asymmetric and the symmetrical stretching vibrations of Si-O-Si and Si-O-Al are being expected to be seen in the wavenumber number ranges 1200-950 cm^{-1} and 800-600 cm^{-1} respectively. The largest peak in the first range and the vibrations in the second one can be seen in Figure 2 [17, 19]. In the La modification, the peak that represents the presence of the Si-O bond is notably different than the unmodified sample, which can be seen in Figure 2, may indicate the reduction of Si-O bonds to allow the formation of the new bonds. Reduction of the Si in this specific modification compared to other ones can also be seen in Table 2. Characteristic peak ofzeolite around 1000 cm^{-1} remained the same in Mg and Zn modified samples, this indicates the preservation of the zeolite structure.

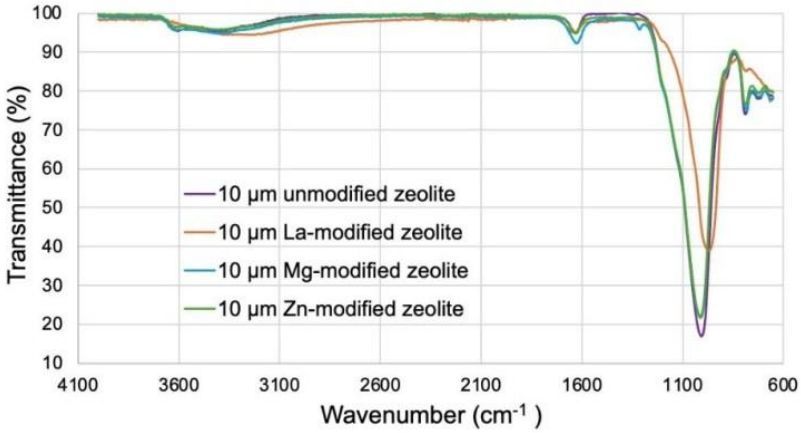

Figure 2. FTIR data for unmodified zeolite and La, Mg, Zn modified zeolite (10 µm)

SEM-EDS Results

Uniform particle size and homogeneous structure can be seen in the lanthanum (III) nitrate modified zeolite and roughly in the magnesium chloride modified zeolite. These properties can make them better options for obtaining a homogeneous paint formulation that can protect the surface evenly. Their structure can be seen in the SEM images given in Figure 3. Particle sizes obtained in this analysis differs from predictions. Size reduction of particles is observed, it can be said that because of that, surface area is increased, and intracrystalline diffusion path length is reduced [20].

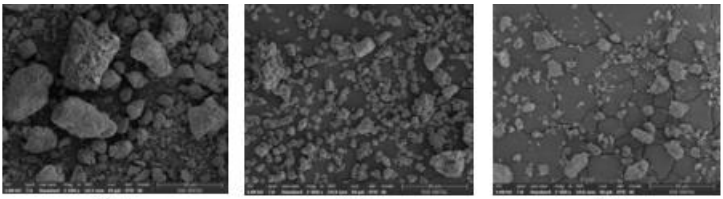

Figure 3. SEM images of Zn (1), La (2), Mg (3) modified natural zeolites of 50μm

The chemical composition of the unmodified zeolite used in this research is given as SiO_2 = 66-69, Al_2O_3 =11-12, Fe_2O_3 = 1.0-1.7 , TiO_2<0.1, MgO = 1, CaO = 2, Na_2O = 0.5 K_2O =3-3.5, BaO<0.1, SrO<0.1[21]. In addition, the results of the EDS analysis are given in the Table 2, which allows us to compare the natural zeolite with the modified ones. Presence of exchanged ions in the modified zeolites' composition is a proof of the successful completion of the modification processes.

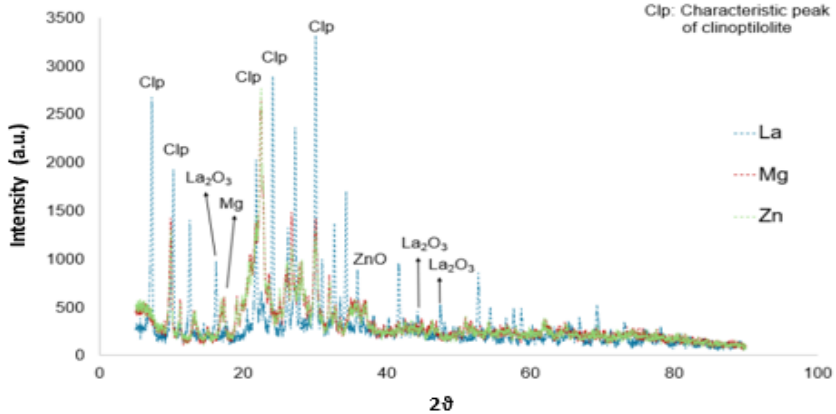

Figure 5. XRD data modified zeolites (10 µm)

As seen in Figure 5, new peaks were observed compared to unmodified zeolite data given in Figure 4 at angles such as 48.7°, 44°, and 15.7° in the lanthanum-modified zeolite structure. These peaks prove the presence of the La_2O_3 structure [23].

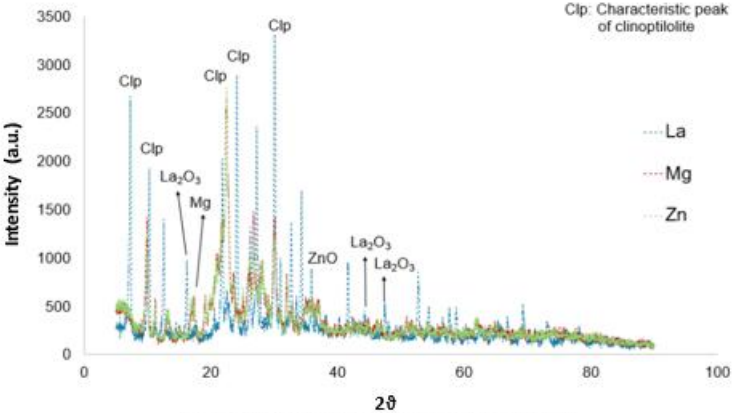

Figure 5. XRD data modified zeolites (10 µm)

As seen in Figure 5, new peaks were observed compared to unmodified zeolite data given in Figure 4 at angles such as 48.7°, 44°, and 15.7° in the lanthanum-modified zeolite structure. These peaks prove the presence of the La_2O_3 structure [23].Furthermore,

the characteristic peaks of clinoptilolite, peaks 9.9° and 24°, were preserved. Therefore, lanthanum was successfully integrated into the structure of clinoptilolite. In magnesium chloride modification process clinoptilolite's characteristic peaks preserved but some peak intensity values changes and shifts, indicating a change in the crystal structure. The reason of this is the magnesium ions enters the lattice structure of the clinoptilolite and the partial deterioration of the clinoptilolite structure happens, this results in a decrease in the refraction of light in XRD [24]. In addition, the formation of new peaks around 15° and 18° indicates that magnesium has hydrate and hydroxide phases [25]. Similar peak shifts and changes in intensities were observed when clinoptilolite was modified with zinc. As mentioned above, these are caused by the disruption of the crystal structure and the change in the diffraction of light because of the zinc ion entering the lattice surface. Also, new peaks occurring at 31.7° and 34° prove the presence of ZnO [26]. Data gained from the Figure 8, prove that the modification changes the structural and chemical properties of zeolites. So as a result, all three modifications were successful.

4. CONCLUSION

Traditional UV stabilizers (such as TiO_2) being effective only in white paint and offering limited thermal stability makes the use of modified natural zeolites in this field, an innovative alternative. They may also be a better option in terms of higher protectiveness and environmental friendliness. The literature indicates that modified zeolites exert beneficial effects on UV stabilization and thermal resistance. Therefore, it can be expected that the modified zeolite added surface paint to reduce the yellowing and mechanical decomposition of PVC profiles. Consequently, lifespan of PVC can be increased by improving its durability with the implementation of modified zeolite added PVC surface paint so a positive contribution to environmental sustainability is projected. The coating developed in this study will provide a solution for the challenges faced in the PVC industry and potentially reduce the waste generation hence the need for excessive maintenance and replacement costs. Paint performance tests shows that the additive developed in this study when added to regular water-based PVC paint, it can stick to the PVC surface successfully even when the coating scratches with the external factors. Characterization tests done on the modified zeolite samples shows that the modification process were successful and SEM analysis shows that the La modified zeolite gives the most uniform sized and shaped particles compared to other samples. The UV- aging test in progress will eventually give the results that will ultimately provide the data necessary

for determination of the developed paint's protectiveness properties. Considering that the XRD, FTIR and SEM-EDS data verifies the modification processes and the paint tests showing that surface bonding between the samples and the paint are notably strong, the additive developed in this study can be further improved as a protective pigment to paints.

Acknowledgements

The authors acknowledge the financial support by the Ege Profil / Deceuninck Ind. & Trade Inc., for providing the samples used in this study and providing permission to use their testing devices and Scientific and Technological Research Council of Turkey (TUBITAK-2209 B) under project application number 1139B412402153.

References

[1] Tang CC, Chen HI, Brimblecombe P, Lee CL. Textural, surface and chemical properties of polyvinyl chloride particles degraded in a simulated environment. Mar Pollut Bull. 2018 Aug 1;133:392–401.

[2] Yu J, Sun L, Ma C, Qiao Y, Yao H. Thermal degradation of PVC: A review. Waste Management. 2016 Feb 1;48:300–14.

[3]. Liu Y, Zhou C, Li F, Liu H, Yang J. Stocks and flows of polyvinyl chloride (PVC) in China: 1980-2050. Resour Conserv Recycl [Internet]. 2020 Mar 1 [cited 2025 Mar 12];154. Available from: https://www.researchgate.net/publication/339604822_Stocks_and_flows_of_polyvinyl_chloride_PVC_in_China_1980-2050

[4]. Zhao E, Xiong X, Li X, Hu H, Wu C. Effect of Biofilm Forming on the Migration of Di(2-ethylhexyl)phthalate from PVC Plastics. Environ Sci Technol [Internet]. 2024 Apr 9 [cited 2025 Aug 27];58(14):6326–34. Available from: https://pubs.acs.org/doi/abs/10.1021/acs.est.3c09021

[5]. Lu L, Li W, Cheng Y, Liu M. Chemical recycling technologies for PVC waste and PVC-containing plastic waste: A review. Waste Management. 2023 Jul 1;166:245–58.

[6]. Lo BTW, Ye L, Tsang SCE. The Contribution of Synchrotron X-Ray Powder Diffraction to Modern Zeolite Applications: A Mini-review and Prospects. Chem [Internet]. 2018 Aug 9 [cited 2025 Apr 24];4(8):1778–808. Available from: https://www.cell.com/action/showFullText?pii=S2451929418301864

[7]. Li Y, Yu J. New stories of zeolite structures: Their descriptions, determinations, predictions, and evaluations. Chem Rev. 2014 Jul 23;114(14):7268–316.

[8]. Choi HJ, Yu SW, Kim KH. Efficient use of Mg-modified zeolite in the treatment of aqueous solution contaminated with heavy metal toxic ions. J Taiwan Inst Chem Eng. 2016 Jun 1;63:482–9.

[9]. Mastinu A, Kumar A, Maccarinelli G, Bonini SA, Premoli M, Aria F, et al. Zeolite Clinoptilolite: Therapeutic Virtues of an Ancient Mineral. Molecules 2019, Vol 24, Page 1517 [Internet]. 2019 Apr 17 [cited 2025 Mar 20];24(8):1517. Available from: https://www.mdpi.com/1420-3049/24/8/1517/htm

[10]. Rodríguez-Iznaga I, Shelyapina MG, Petranovskii V. Ion Exchange in Natural Clinoptilolite: Aspects Related to Its Structure and Applications. Minerals [Internet]. 2022 Dec 17 [cited 2025 Mar 19];12(12):1628. Available from: https://www.mdpi.com/2075-163X/12/12/1628/htm

[11]. Mohammadzadeh Kakhki R, Zirjanizadeh S, Mohammadpoor M. A review of clinoptilolite, its photocatalytic, chemical activity, structure and properties: in time of artificial intelligence. J Mater Sci [Internet]. 2023 Jul 1 [cited 2025 Mar 13];58(26):10555–75. Available from: https://link.springer.com/article/10.1007/s10853-023-08643-9

[12]. Korniy S, Danyliak MO, Zin I. Zeolite-Based Anti-corrosion Pigments for Polymer Coatings: A Brief Review. Advances in Polymer Technology. 2024;2024.

[13]. Chromium, nickel and welding. IARC monographs on the evaluation of carcinogenic risks to humans. International Agency for Research on Cancer [Internet]. 1990 [cited 2025 Mar 14];49:49–256. Available from: https://www.ncbi.nlm.nih.gov/books/NBK519250/

[14]. Li Q, Wang Y, Zhang S, Pang L, Tong H, Li J, et al. Novel fluorinated random co-polyimide/amine-functionalized zeolite MEL50 hybrid films with enhanced thermal and low dielectric properties. J Mater Sci [Internet]. 2017 May 1 [cited 2025 Mar 14];52(9):5283–96. Available from: https://link.springer.com/article/10.1007/s10853-017-0768-4

[15]. Ahmed NM, Emira HS, Selim MM. Anticorrosive performance of ion-exchange zeolites in alkyd-based paints. Pigment and Resin Technology. 2011;40(2):91–9.

[16]. Roselli S, Bellotti N, Deyá C, Revuelta M, Del Amo B, Romagnoli R. Lanthanum-exchanged zeolite and clay as anticorrosive pigments for galvanized steel. Journal of Rare Earths. 2014 Apr 1;32(4):352–9.

[17]. Madejová J. FTIR techniques in clay mineral studies. Vib Spectrosc. 2003 Jan 15;31(1):1– 10.

[18]. Mansouri N, Rikhtegar N, Ahmad Panahi H, Atabi F, Shahraki BK. Porosity, characterization and structural properties of natural zeolite - Clinoptilolite - As a sorbent. Environment Protection Engineering [Internet]. 2013 Jan 1 [cited 2025 Aug 8];39(1):139– 52.

Available from:
https://www.researchgate.net/publication/260158127_Porosity_characterization_and_structural_properties_of_natural_zeolite_-_Clinoptilolite_-_As_a_sorbent

[19]. Król M, Koleżyński A, Mozgawa W. Vibrational Spectra of Zeolite Y as a Function of Ion Exchange. Molecules 2021, Vol 26, Page 342 [Internet]. 2021 Jan 11 [cited 2025 Aug 8];26(2):342. Available from: https://www.mdpi.com/1420-3049/26/2/342/htm

[20]. Tao Y, Kanoh H, Abrams L, Kaneko K. Mesopore-modified zeolites: Preparation, characterization, and applications. Chem Rev [Internet]. 2006 Mar [cited 2025 Aug 12];106(3):896–910. Available from: https://pubs.acs.org/doi/full/10.1021/cr040204o

[21]. Gördes Zeolite Material Safety Data Sheet. 2013 Jul.

[22]. Pekcioğlu ŞY. Investigation of factors that influence the preparation of zeolite modified anticorrosive paint [Internet] [Master's thesis]. Ege University; 2019 [cited 2025 Aug 15]. Available from: https://hdl.handle.net/11454/68266

[23]. Mustofa K, Yulizar Y, Saefumillah A, Apriandanu DOB. La2O3nanoparticles formation using Nothopanax scutellarium leaf extract in two-phase system and photocatalytic activity under UV light irradiation. IOP Conf Ser Mater Sci Eng [Internet]. 2020 [cited 2025 Aug 8];902(1). Available from:
https://www.researchgate.net/publication/346458638_La_2_O_3_nanoparticles_formation_using_Nothopanax_scutellarium_leaf_extract_in_two-phase_system_and_photocatalytic_activity_under_UV_light_irradiation

[24]. Akyalcin S, Akyalcin L, Ertugrul E. Modification of natural clinoptilolite zeolite to enhance its hydrogen adsorption capacity. Research on Chemical Intermediates [Internet]. 2024 Mar 1 [cited 2025 Aug 8];50(3):1455–73. Available from:
https://www.researchgate.net/publication/377727130_Modification_of_natural_clinoptilolite_zeolite_to_enhance_its_hydrogen_adsorption_capacity

[25]. Munusamy TD, Sarmin S, Ong HR, Gan WT, Hong CS, Khan MMR. Catalytic performance and antimicrobial activity of Mg(OH)2/MgO colloidal nanoparticles in alkyd resin nanocomposite derived from palm oil. Polymer Bulletin. 2020 Sep 1;77(9):4571–86.

[26]. Singh Saini G, Kumari M, Magdaline Eljeeva Emerald F, Singh Saini G. International Journal of Statistics and Applied Mathematics 2023; SP-8(3): 630-634 Investigating structural changes of ZnO nanoparticles using powder X-ray diffraction over 6 months. Maths. 2023;8(3):630–4.

Experımental Investigation of Thermoplastic Composite-Based Sandwich Panels Under Static And Impact Loading

Murat YAZICI[1] [0000-0002-8720-7594], Momen ELBHNASAWI[2] [0009-0001-4216-0243], Yalçın BOZTOPRAK[3] [0000-0003-1714-7394]

[1]Applied Mechanics and Advanced Materials Research Group (AMAMRG) Lab., Automotive Eng. Dep., Bursa Uludağ University, Bursa 16059, Türkiye

[2]Applied Mechanics and Advanced Materials Research Group (AMAMRG) Lab., Automotive Eng. Dep., Bursa Uludağ University, Bursa 16059, Türkiye

[3] Marmara University, Technology Faculty, Metallurgy and Materials Department, İstanbul 34854, Türkiye

myazici@uludag.edu.tr

Abstract. Thermoplastic composites provide elevated specific strength and modulus, in addition to benefits like recyclability and ease of fabrication. This study examines sandwich panels made of woven unidirectional (UD) glass fiber/polypropylene (GF/PP) face sheets and circular cell polypropylene (PP) cores. The mechanical performance of these sandwich panels was assessed using experimental and computational methods under static and impact loading conditions. Face sheets were produced from plain woven GF/PP UD tapes compressed at 185°C in a mold, resulting in a final thickness of 0.25 mm and a fiber volume fraction of around 65%. The sandwich core was fabricated by PP using an extrusion mold. In this study, the primary aim was to design an optimum electric vehicle battery box with increased resistance to static and impact loads. Three-point bending and penetration tests were performed to assess performance under static and dynamic impact loading. The findings indicated that thin woven composite sheets reduced the penetration depth of steel tips by more than 50% and increased the bending resistance of the circular cell polypropylene core by more than 40%. energy absorption under impact increased from 4.2 J to 37.33 J highlighting the superior damage tolerance provided by the sandwich configuration."

Keywords: Thermoplastic composites, Glass fiber/Polypropylene, 2D woven continuous tape, circular cell PP core

1. Introduction

Composite sandwich structures have gained significant attention in various engineering applications due to their remarkable properties, including a high strength-to-weight ratio, excellent energy absorption capabilities, and versatile applications in lightweight structural components. These structures typically consist of two thin but stiff face sheets and a lightweight core, making them highly efficient in terms of mechanical performance. They are used extensively in aerospace, automotive, and construction industries, where minimizing weight while maintaining structural integrity is a critical requirement. The sandwich configuration enhances the section modulus of the structure, providing high bending stiffness and superior energy absorption characteristics, making them ideal for impact-resistant applications [1-2].

Among the various types of composite materials, thermoplastic composites have emerged as a promising alternative to thermoset composites due to their recyclability, ease of processing, and superior damage tolerance. Thermoplastic composites also offer the advantage of being capable of fast, high-throughput manufacturing, which is a major consideration in industries that require cost-effective production methods [3]. Notably, polypropylene (PP) has become one of the most widely used thermoplastics for composite sandwich structures. It offers several benefits, including low density, good chemical resistance, and compatibility with fiber reinforcement. When reinforced with glass fibers, PP-based composites provide enhanced mechanical properties, including high in-plane stiffness and strength, while retaining the inherent toughness and impact resistance of the thermoplastic matrix [4-5].

The core material in a sandwich structure plays a pivotal role in its overall performance, particularly with respect to energy absorption during impact events. Recent advancements in core material design have focused on optimizing geometric configurations to enhance the structural integrity and impact resistance of the sandwich panels. For instance, honeycomb, foam, and circular-cell core structures are popular choices for achieving lightweight yet durable designs. Studies have shown that cores with circular-cell geometries, in particular, offer superior energy dissipation during impact events and prevent catastrophic core collapse, making them ideal for applications where both strength and impact resistance are crucial, such as in electric vehicle battery enclosures [6-7]. The combination of high-strength, lightweight face sheets and optimized core configurations has positioned thermoplastic composite sandwich panels as a leading solution for a wide range of engineering challenges.

Recent developments in thermoplastic composites, particularly in glass fiber-reinforced polypropylene (GF/PP) materials, have furthered their applicability in engineering structures. The integration of continuous glass fibers within the PP matrix has demonstrated significant improvements in both mechanical performance and sustainability. These materials are increasingly being used in industries such as automotive, where the need for lightweight, impact-resistant components is paramount. Moreover, the recyclability of GF/PP composites aligns with the growing demand for sustainable and environmentally friendly materials in manufacturing processes [8-9].

This study focused on the fabrication and mechanical performance of thermoplastic composite sandwich panels made from woven GF/PP face sheets and a polypropylene circular-cell core. The sandwich panels were subjected to experimental tests, including three-point bending and impact penetration tests, to evaluate their mechanical properties under dynamic loading conditions. By assessing the bending stiffness, impact resistance, and failure modes of the sandwich panels, this study aims to provide a comprehensive understanding of the mechanical behavior of thermoplastic composite sandwich structures.

The results are expected to contribute valuable insights into optimizing the design of these materials for lightweight, high-performance applications, particularly in the transportation sector, where both strength and weight reduction are key considerations.

2. Materials and Methods

2.1. Materials

The sandwich panels developed in this study consisted of glass fiber/polypropylene (GF/PP) woven tape face sheets and a circular-cell polypropylene (PP) core. Unidirectional GF/PP tapes with a fiber volume fraction of 60% were used. Each UD tape had a thickness of 0.35 mm and consisted of E-glass fibers embedded in a polypropylene matrix. The tapes were arranged in 0° and 90° orientations to form a plain-woven configuration, providing balanced stiffness in both principal directions. Extrusion-molded PP with a circular-cell geometry (average cell diameter 5 mm, wall thickness 1.25 mm) was used as a core. The average core thickness was 17.3 mm (±0.1 mm). The PP matrix has a 0.90 g/cm³ density, 1.5 GPa tensile modulus, and 35 MPa tensile strength. E-glass continuous fiber filament has a 2.54-2.6 g/cm3 density, 2500 MPa tensile strength, 70 GPa tensile modulus, and 3% elongation at break.

thickness was 17.3 mm (±0.1 mm). The PP matrix has a 0.90 g/cm³ density, 1.5 GPa tensile modulus, and 35 MPa tensile strength. E-glass continuous fiber filament has a 2.54-2.6 g/cm3 density, 2500 MPa tensile strength, 70 GPa tensile modulus, and 3% elongation at break.

2.2. Fabrication of Woven GF/PP Face Sheets

UD GF/PP tapes were cut and laid in alternating 0°/90° orientations to create a balanced woven structure. The performance was consolidated using a hydraulic hot press at 185 °C, applying 1 MPa pressure for 10 minutes. This ensured complete matrix melting and strong

bonding at tape crossovers [3]. The resulting plates (two plies per face sheet) had a consolidated thickness of 0.70 mm.

Figure 1. GF/PP woven plate.

2.3. Sandwich Panel Production

The sandwich panels were fabricated by placing one woven GF/PP plate on each side of the polypropylene circular-cell core, followed by consolidation in a hot press. The layup sequence consisted of a face sheet, the circular-cell core, and a second face sheet. The fabricated sandwich panels were first cut into the required dimensions using a precision waterjet cutting machine to ensure clean edges and avoid inducing thermal or mechanical damage to the core and face sheets. For the three-point bending tests, rectangular specimens with dimensions of 200×50 mm were prepared. For the impact penetration tests, square

specimens measuring 75×75 mm were extracted from the same panels. The assembly was heated to 180 °C to soften the polypropylene in both the face sheets and the surface of the core, then pressed at 300 KPa for 10 minutes to achieve melt fusion. After pressing, the panels were cooled under pressure to prevent warping and ensure dimensional stability. The final panels had an average thickness of approximately 20.1 mm, consisting of two 0.70 mm face sheets and a 17.3 mm core, with an additional melt layer formed during consolidation.

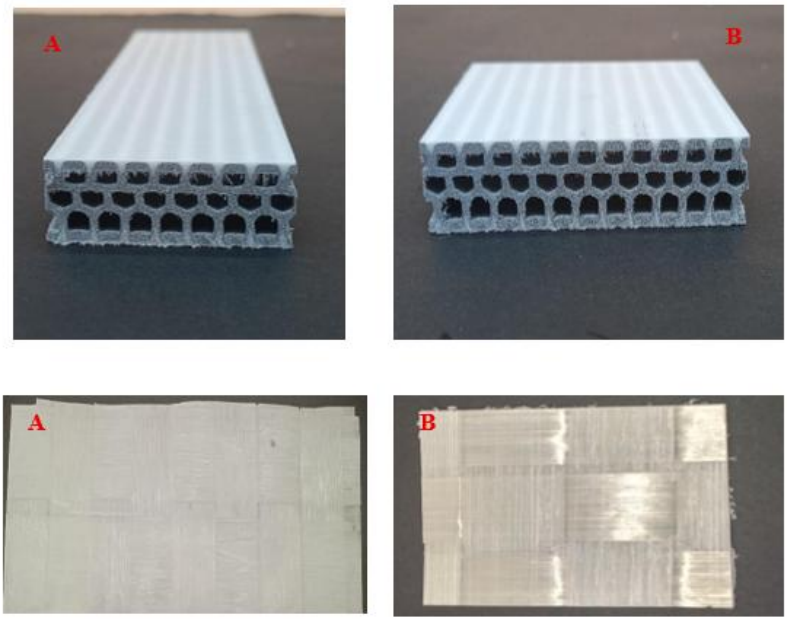

Figure 2. A) 3 Point-Bending specimen after cutting B) Penetration specimen after cutting.

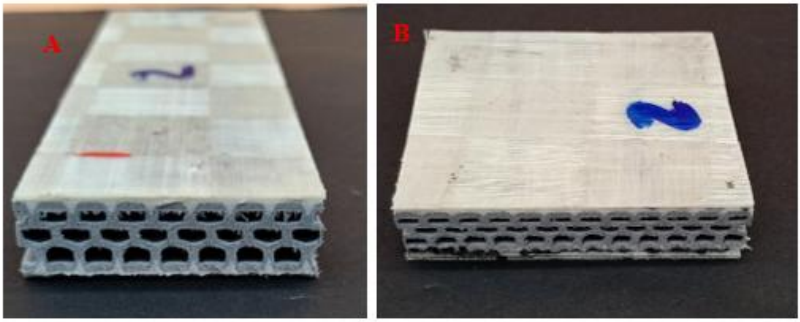

Figure 3. A) Sandwich panel specimen for 3-point bending test B) Sandwich panel specimen for impact penetration test

2.4. Mechanical Testing

Two types of mechanical tests were performed: three-point bending and impact penetration tests. The three-point bending test was conducted in accordance with ASTM D7250, using a support span of 150 mm, specimen length of 200 mm, and specimen width of 50 mm. The average specimen thickness was 20.1 mm. For the impact penetration tests, square specimens measuring 75 × 75 mm with the same average thickness were prepared. These tests were designed to evaluate the flexural rigidity and impact resistance of the sandwich structures, simulating potential loading conditions in applications such as electric vehicle battery enclosures.

The impact experiments were carried out using a specially designed pneumatically controlled impact system, which enables controlled and repeatable impact loading under various test conditions. The setup allows for adjustments in tip geometry (e.g., hemispherical and conical tips) and support configurations, thereby enabling the assessment

of different failure modes. Additionally, a high-speed camera system was employed during testing to capture the deformation and failure progression of the specimens in real time, providing valuable insights into energy absorption mechanisms and localized damage development.

Figure 3. Test setup

3. Results and Discussion

3.1 Impact Penetration Test Results

Penetration resistance was assessed by comparing the composite sandwich panels against the raw polypropylene core. As summarized in Table 1, the composite panels demonstrated a significant increase in load-bearing capacity and energy absorption.

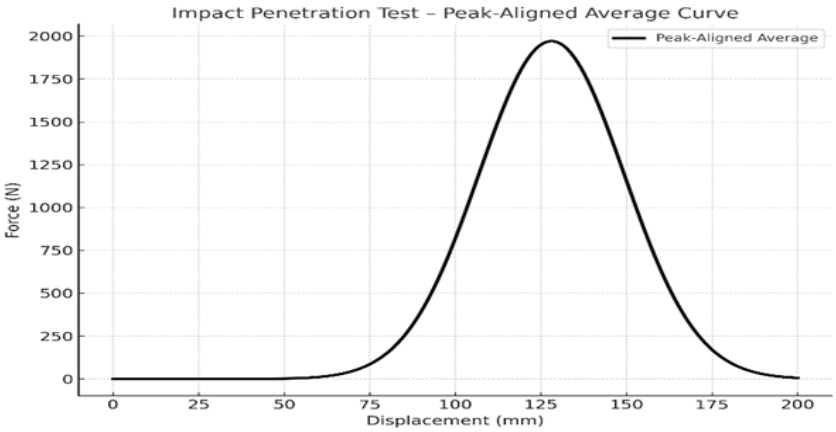

Figure 4. Representative Peak-Aligned Average Force Displacement Curve for Sandwich Panels under Impact Penetration

Table 1. Average penetration performance of sandwich panels

Parameter	Raw PP Core (Avg.)	Composite Sandwich (Avg.)	Improvement
Maximum Force (N)	930.4 ± 12.5	1971.0 ± 35.4	+111.8%
Absorbed Energy (J)	4.2 ± 0.8	37.33 ± 6.05	+788.8%

The representative force–displacement curve indicates an initial linear elastic region followed by a progressive damage phase, reflecting stable resistance. The maximum force of 1971 N and the absorbed energy of 37.33J demonstrate that the panels can effectively withstand localized impacts without catastrophic failure. As observed in Figure 6A, the impactor head was stopped by the woven GF/PP face sheet, preventing damage to the polypropylene core. In contrast, the raw core material exhibited a brittle response. As shown in the newly added Figure 6B, the raw polypropylene core shattered catastrophically upon impact. This failure mode results from the high calcite filler content, which limits the material's ability to dissipate energy through plastic deformation.

Figure 5. The composite penetration specimen after the test.

sheets and the top face of the core. In **Figure 7,** we can see that the core got completely shattered. The synergistic action between the woven GF/PP face sheets and the circular-cell PP core thus enhanced both load-bearing capacity and energy dissipation, validating their suitability for impact-resistant applications. The specimen after impact, captured by the high-speed camera, further illustrates the impact event's effects.

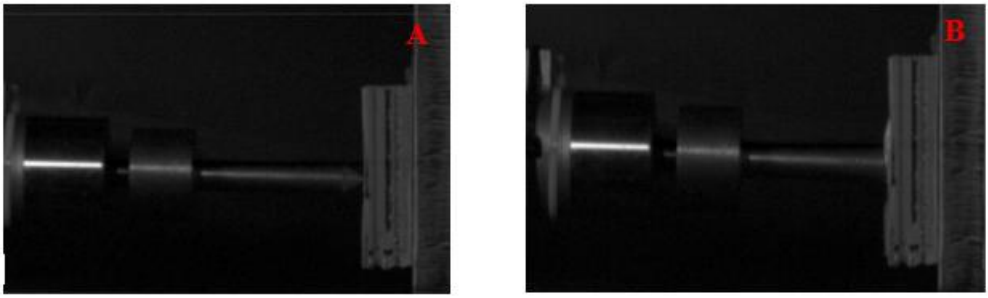

Figure 6. A) Specimen at the Exact Impact Moment. B) Specimen After the Impact. Captured by a high-speed camera.

Figure 7 Raw core penetration specimen after the impact.

3.2 Three-Point Bending Test Results

Flexural performance was evaluated by comparing the flexural performance of the raw core material in accordance with ASTM D7250. The composite panels achieved a much higher peak force due to the reinforcement of the woven face sheets.

Table 2. Average bending performance of raw vs. composite sandwich panels.

Material	Maximum Force (N)
Raw Material	**930.4**
Composite (avg.)	**1276.7**
Improvement	**+37.2%**

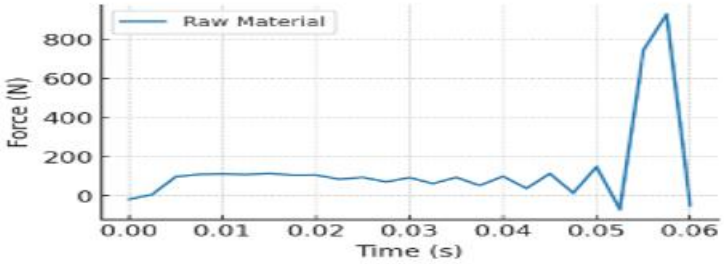

Figure 7. Average force–displacement curve for raw core material.

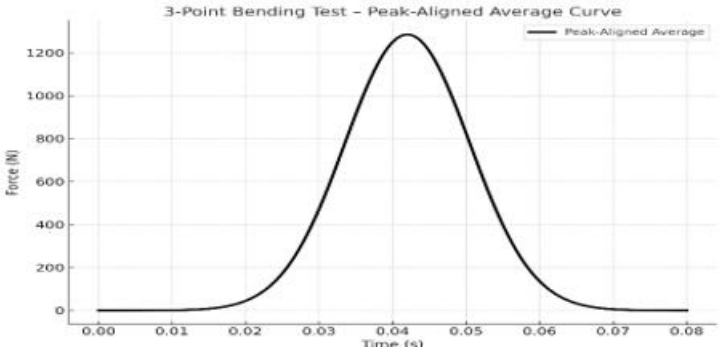

Figure 8. Representative peak-aligned average force–time curve for composite sandwich panels under three-point bending.

Figure 8 illustrates the superior stiffness of the sandwich configuration. The composite sandwich panels exhibited a 37.2% increase in bending strength compared to the raw polypropylene core, with an average maximum bending force of 1276.7 N. The face sheets improved stiffness and delayed crack initiation, while the PP circular-cell core

provided support and stability during deformation. As we can see in **Figure 9** in the composites the face sheet didn't break while the core got broken both composite and raw. The brittle behavior of the PP core (High Calcite filler) caused it to separate from the surface plates, especially during 3-point bending, and the dynamic bending behavior of the sandwich material remained limited. **Figure 10** illustrates the high-speed camera impact moment.

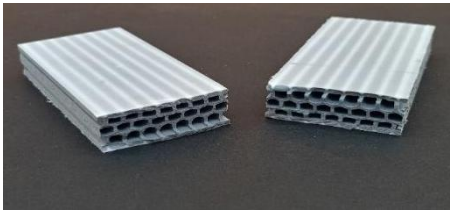

Figure 9. The 3 Point-Bending specimens after the test A) Composite sandwich. B) Raw core.

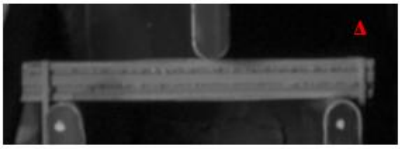

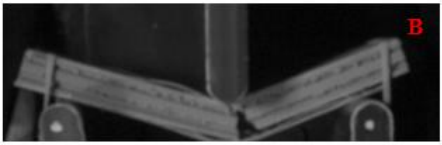

Figure 10. A) Exact Impact Moment Captured by High-Speed Camera. B) Specimen After the Impact (Captured by High-Speed Camera).

3.3. Morphological Failure Analysis

Digital microscopy was used to examine the failed specimens. Figure 11 reveals the microscopic damage mechanisms that enabled high energy dissipation:

- **Fiber-Matrix Debonding**: Extensive separation between the continuous glass fibers and the PP matrix was observed in the impact zone.
- **Localized Delamination**: Separation between the woven $0^\\circ/90^\\circ$ layers allowed the face sheets to absorb significant energy before the impactor reached the core.
- **Ductile vs. Brittle Contrast**: While the raw core shattered into multiple fragments (Figure 7), the composite panels localized the damage to the skin, keeping the circular-cell core largely intact.

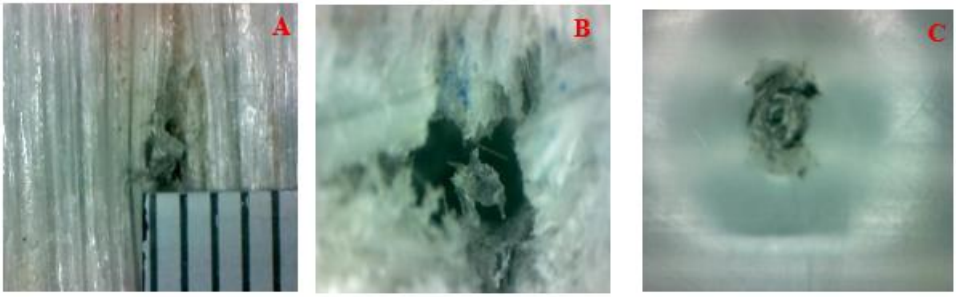

Figure 11 Penetration specimens under microscope. A) Face sheet damage size (1 mm) B) Face sheet fiber damage. C) Core top layer damage.

Digital microscopy revealed that enhanced energy absorption is primarily driven by inter-laminar delamination and fiber-matrix debonding within the woven face sheets. While the raw polypropylene core exhibited brittle fracture and catastrophic shattering, the composite skins localized the impact energy, maintaining structural integrity through controlled microscopic failure modes.

4. **Conclusion**

This study investigated the fabrication and mechanical performance of thermoplastic sandwich panels composed of woven GF/PP face sheets and circular-cell PP cores. The results of the experimental program demonstrated that the developed panels possess excellent resistance to both impact penetration and impact flexural loading. Under penetration tests, the panels sustained an average maximum force of approximately 1971 N and absorbed nearly 37.3 J of energy, highlighting their ability to withstand localized impact without catastrophic failure. Similarly, the three-point bending tests showed a 37.2% increase in bending strength over the raw polypropylene core, with the composite panels reaching an average maximum force of 1276.7 N. The brittle behavior of the PP core managed the whole composite bending failure.

The mechanical response of the panels was characterized by progressive and stable damage mechanisms, including fiber–matrix interactions, localized core indentation, and delayed cracking in the woven face sheets. These mechanisms contributed to significant energy dissipation and structural reliability, underscoring the advantage of combining woven GF/PP face sheets with circular-cell PP cores. Beyond their mechanical performance, the panels also offer a sustainability advantage, as the fully thermoplastic configuration ensures recyclability and compatibility with industrial-scale processing.

Overall, this study validates that the designed sandwich panels provide a balanced combination of lightweight construction, high strength, and energy absorption. These characteristics make them promising candidates for advanced structural applications, particularly in the field of electric vehicle battery enclosures and other protective lightweight systems where impact penetration and impact flexural resistance are critical.

References

[1] Gao, X., Zhang, M., Huang, Y., Sang, L., & Hou, W. (2020). Experimental and numerical investigation of thermoplastic honeycomb sandwich structures under bending loading. *Thin-Walled Structures*, 155, 106961. https://doi.org/10.1016/j.tws.2020.106961

[2] Chen, L., Wang, J., Nie, S., Pan, X., & Du, B. (2024). High-temperature effect on continuous glass fiber reinforced polypropylene multilayer composite and corrugated sandwich panels. *Chinese Journal of Aeronautics*, 38, 103210. https://doi.org/10.1016/j.cja.2024.08.041

[3] Türkoğlu, İ. K., Bayram, T., & Yazıcı, M. (2024). Mechanical properties of 3D printed continuous carbon fiber/polypropylene lattice core composite sandwich structure. *Uludağ University Journal of The Faculty of Engineering*, 29(3). https://doi.org/10.17482/uumfd.1497273

[3] Ragupathi, B., & Balle, F. (2024). Characterization of glass-fiber reinforced thermoplastic composite after ultrasonic reconsolidation. *European Journal of Materials*, 4(1), 2313316. https://doi.org/10.1080/26889277.2024.2313316

[4] Guo, D., Li, Y., Wang, W., Zhu, K., & Liu, H. (2025). Study on the preparation of fully thermoplastic composite sandwich structure by non-isothermal molding process and its bending properties. *Journal of Composite Materials*, 59(10), 1331–1349. https://doi.org/10.1177/00219983241313298

[5] Sadiq, M. A., & Kovács, G. (2025). Optimization of composite sandwich structures: A review. *Machines*, 13(7), 536. https://doi.org/10.3390/machines13070536

[6] Lin, Y., Xiao, C., Li, H., Zhang, X., Hou, Y., & Tao, J. (2024). Flexural and low-velocity behavior of GFPP/DP980 honeycomb sandwich structure inspired by fiber metal laminates. *Polymer Composites*. https://doi.org/10.1002/pc.29315

[7] Islam, A., Ferdous, W., Burey, P., Nahar, K., Yan, L., & Manalo, A. (2025). Polymer composite sandwich panels composed of hemp and plastic skins and composite wood, recycled plastic, and styrofoam cores. *Polymers*, 17, 1359. https://doi.org/10.3390/polym17101359

[8] Zhu, X., Xiong, C., Yin, J., Qin, Y., Sun, H., Cui, K., Zou, Y., & Deng, H. (2023). Three-point bending characteristics of all-composite sandwich panels with different core configurations. *Mechanics of Advanced Materials and Structures*. https://doi.org/10.1080/15376494.2023.2172237

Effect of Heating Rate During Curing on the Properties of the Composite Materials

Ferhat GÜL [1][0000-0001-9087-8236 – ORCID ID], Nisanur Gedik [1][0009-0007-1817-1755 - ORCID ID],

Furkan SAĞLAM [1][0009-0006-6027-0880 - ORCID ID] Melike GEDİK [2,3][0009-0009-4221-7690 - ORCID ID]

[1] Gazi University, Faculty of Technology, Department of Metallurgical and Materials Engineering, Beşevler, Ankara, Türkiye

[2] Gazi University, Faculty of Engineering, Department of Chemical Engineering, Maltepe, Ankara, Türkiye

[3] Nurol Technology, Kazan, Ankara, Türkiye

fgul@gazi.edu.tr

Abstract: The curing cycle is a critical determinant in composite manufacturing, directly governing the mechanical integrity and performance of the final structure. While dwell temperature and duration are fundamental parameters, the heating rate is equally vital for optimizing production, product quality, and energy efficiency. This study investigates glass fiber-reinforced polymer composites fabricated via an autoclave system. Curing was conducted at a dwell temperature of 120 °C for 2 hours, comparing two distinct heating rates: 1 °C/min and 2 °C/min. The resulting laminates were characterized using Differential Scanning Calorimetry, tensile testing, three-point bending, and short-beam tests to evaluate the glass transition temperature, tensile strength, flexural strength, and Interlaminar Shear Strength. Mechanical test results showed that specimens cured at 1 °C/min exhibited higher tensile strength and elastic modulus. Increasing the heating rate to 2 °C/min led to noticeable reductions in flexural strength and flexural strain. In terms of interlaminar shear strength (ILSS), no significant difference was observed between the specimens, although a marginally higher ILSS value was recorded for the composites cured at the higher heating rate.

Keywords: Composite materials, heating rate, mechanical properties

1. Introduction

Composite materials are classified primarily by their matrix material: polymer, ceramic, or metal. Due to their many superior properties, such as low density and high mechanical strength, polymer matrix composites are widely used across sectors, including defense, aerospace, automotive, energy, marine, biomedical, construction, furniture, and sports [1–4]. In the aerospace field, by using carbon and other fiber-reinforced composites, many desirable properties such as high specific strength, fuel economy, corrosion and fatigue resistance, and radar absorption can be achieved [5–8]. For example, carbon fiber-reinforced polymers (CFRPs) began to be used in aerospace in the 1960s. Owing to their high specific strength and stiffness, they have been widely adopted in aircraft components, thereby contributing to weight reduction [9]. During the production of composite materials, curing evaluation is crucial for optimizing curing efficiency. Glass transition temperature measurements are commonly used to determine the degree of cure [10]. The curing process affects the degree of cross-linking in thermoset polymers and influences the glass transition temperature (Tg), which, in turn, alters the material's thermal and mechanical properties [11]. Inadequate resin flow during the molding process or inappropriate curing conditions may cause porosity. Therefore, curing in an appropriate temperature range is recommended [3]. However, not only curing temperature and duration but also the heating rate during curing are considered important factors affecting product quality [4].

On the other hand, a high heating rate during curing has been reported to cause significant distortion in the manufactured composite part [12]. The curing of aerospace composites, is time-consuming and energy-intensive particularly when performed with methods such as autoclaves, ovens, and heated presses, By using the Direct Electrical Curing (DEC) method, improvements in energy efficiency, precise control of curing temperature, a lower void ratio compared to oven curing, and, at the same time, higher heating rates during curing can be achieved. In this method, the set temperature and the control temperature progress almost in parallel, as shown in Figure 1 [13]. Warnock et al. aimed to reduce internal stresses by controlling excessive heat and to ensure low viscosity and high flowability of the resin in the production of thick-section composite panels. According to the study, rapid heating made the resin more fluid but led to higher heat generation, whereas slow heating reduced heat generation but also decreased resin flowability. The applied method was reported to result in lower porosity and better consolidation [14]. In the study by ElKhoury and Berg on carbon fiber-reinforced thermoset resin composites, isothermal curing and stepwise curing at different heating rates were applied. As shown in Figure 2, the glass transition temperatures of the materials varied with the applied curing method. In isothermal curing, the glass transition temperature showed only a slight variation, except at 140 °C. In

contrast, during stepwise curing at different heating rates, this temperature increased continuously, attributed to the volatility of the hardener [15]. In DSC studies by Zhu and colleagues on the curing kinetics of E-glass/epoxy prepreg composites using 7901 toughened resin, the peak temperatures were 139 °C, 154 °C, and 160 °C at heating rates of 5, 10, and 15 °C/min, respectively [16]. Voto et al. proposed a two-stage curing profile for very thick laminates to limit overheating and reduce curing time. In the first stage, lower T1 temperatures of 110–130 °C were suggested, followed by a main curing temperature T2 of 180–200 °C in the second stage, with a low heating rate of around 2 °C/min. Accordingly, no overheating (overshoot) was observed in the 2 mm-thick laminates, and it was determined that the main curing temperature, T2, had a more pronounced effect on the curing time. Although the overheating threshold was not exceeded in the 20 mm-thick laminates, in some cases, increasing the T1 temperature was necessary, thereby reducing curing time by 18%.

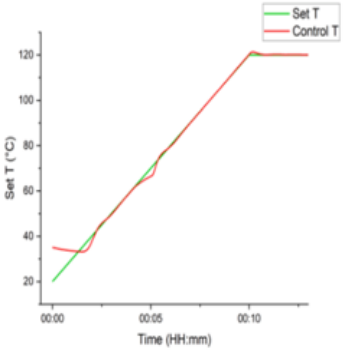

Figure 1. Change the inset and control temperatures due to direct electric (resistance) heating at a heating rate of 10 °C/min. [13].

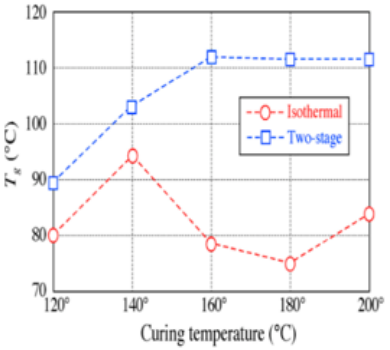

Figure 2. Glass transition temperatures of isothermally and two-stage cured resins. [15].

For 50 mm laminates, the overheating threshold was exceeded and the two-stage method was insufficient, so a three-stage method was proposed [17]. In a study conducted by Herring and Fox using the Quickstep method, it was shown that surface porosity decreased with decreasing heating rate and increasing pressure, as illustrated in Figure 3. As shown in Figure 4, increasing the heating rate accelerated cross-linking of the G83C resin, narrowed the process window, restricted resin flow between layers before curing, and affected surface quality [18]. It was understood that the heating rate affects the applied curing method and that different curing processes may yield different effects. Similarly, Davies et al. reported that, with increasing heating rate, the time for the resin to reach its minimum viscosity decreased. As seen in Figure 5, this duration was about 60 minutes at a heating rate of 2 °C/min, while at 15 °C/min it dropped to as little as 10 minutes [19]. In the study by Dong et al., prepregs made of T800 carbon fiber with 60% fiber volume fraction and a specially developed out-of-autoclave epoxy were used, with dry fibers left in the center for air evacuation. Two heating rates, 1.5 °C/min and 5 °C/min, were applied, with an initial cure at 120 °C for 1 hour and a final cure at 180 °C for 2 hours, to investigate their effect on the degree of cure. As shown in Figure 6, although slow heating achieved a slightly higher cure in the initial stage, the difference was slight, and in both cases, the resin was fully cured at the end of the final curing. Fast heating delivered the same curing quality in less time, resulting in 35% energy savings and greater efficiency [20].

In a study by Yong et al., DMA, TMA, and DSC methods used for Tg measurement were compared, and it was determined that Dynamic Mechanical Analysis (DMA) was able to determine the glass transition temperature (Tg) much more accurately compared to Thermomechanical Analysis (TMA) and Differential Scanning Calorimetry (DSC) [10].

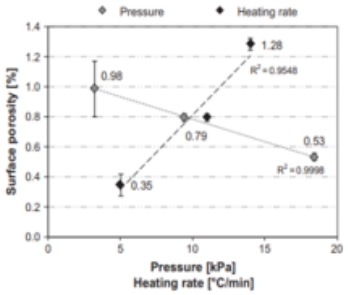

Figure 3. Effect of pressure and heating rate on the surface porosity of the composite [18].

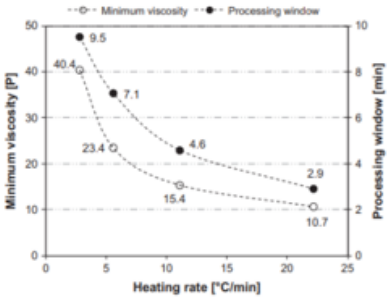

Fig. 4. Effect of heating rate on the minimum resin (G83C) viscosity and the process window [18]

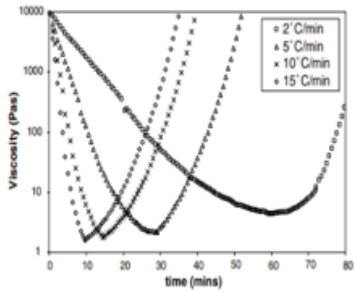

Figure 5. The variation of the viscosity of 6376 resin with respect to the heating rate. [19]

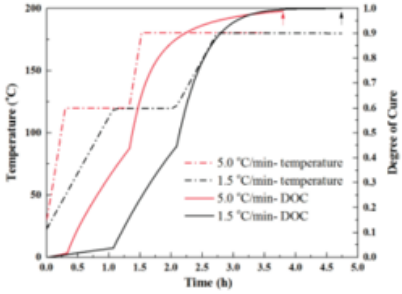

Figure 6. Degree of cure depending on heating rate and cycle time [20]

Kim and Lee investigated the curing characteristics of S-glass fiber/polyester composites at heating rates of 0.5, 1.0, and 2.0 °C/min using dynamic DSC (Differential Scanning Calorimetry). They found that curing started at 110 °C and ended at 180 °C, and that these temperatures increased with increasing heating rate, delaying resin curing kinetics [21]. In the study conducted by Chang et al. using unidirectional carbon fiber-reinforced epoxy prepregs, it was reported that composite material properties varied depending on curing parameters, and that optimal properties were obtained under 0.6 MPa pressure, 160 °C for 2 hours of curing time, and a heating rate of 1.5 °C/min [22].

There are a limited number of studies investigating the effects of curing temperature and time, as well as the heating rate during curing, on product properties and interlaminar shear strength in composite production [13–17, 23–25, 19, 22]. In this study, the aim is to investigate the effect of heating rate during the curing process on the tensile and flexural

strengths, as well as the interlaminar shear strength, of composite materials produced using glass fiber-reinforced polymer matrix prepreg and the autoclave curing method.

2. Experimental Result and Discussion

In this study, the variations in tensile, three-point bending, and interlaminar shear strength of composite specimens produced by the prepreg lay-up method using E-glass prepreg were investigated at different heating rates. The materials used in this study are given in Table 1. The samples were cured in an autoclave at 120°C for 2 hours at two different heating rates. In this study, E-Glass 163 gsm Plain fabric Epoxy 40% RC prepreg was removed from the cold storage and brought to room temperature before being cut to 40 cm x 40 cm dimensions on a ply cutting machine. After a release agent was applied to the glass plates to be laid, a specified period elapsed, and the laying process began. Two prepregs were cut to appropriate dimensions and laid in the same direction (0°/90°) with 22 layers, leaving no gaps between them, and vacuum bagging was performed. To improve adhesion between prepreg layers and eliminate voids, a 0.85 bar vacuum was applied for 15 minutes. Using an Akarmak brand autoclave, one laminate was cured at a heating rate of 1 °C/min and the other at 2 °C/min, both at 4 bar pressure and 120 °C for 2 hours. After cooling down to 50 °C, the laminates were removed from the autoclave. The produced composites were first visually examined and then inspected ultrasonically. Test samples were prepared by CNC cutting. DSC analysis was performed using a TA Instruments SDT 650 Simultaneous DSC/TGA device and Trios V5.7.0.56 software at heating rates of 1 ˚C/d and 2 ˚C/d up to 350 ˚C. Specimen dimensions for tensile, three-point bending, and inter-laminar shear strength tests are given in Table 2.

Table 1. Materials Used in the Production of Composite Specimens

Materials	Properties
E Glass Prepreg	12k 420 gsm 2x2 Twill Epoksi % 40 R-C
Mold Release Agent	Loctite 770 NC Frekote
Breather	Airweave N10
Release film	Airtech A4000R
Vacuum bag	Wrightlon® 5400
Sealant tape	Airtech AT200Y
Vacuum port	Airtech VAC VALVE 406TF
Thermocouple	K tipi
Adhesive	Araldite 2014-2
Glass Fiber–Epoxy Composite Tabs	-

Table 2. Specimen Dimensions and Test Conditions

Test Performed	**Specimen Dimensions**
Tensile Test	2,8 mm x 25mm x 250 mm
Three-Point Bending Test	2,8 mm x 12,7mm x 125 mm
Interlaminar Shear Test	2,8 mm x 6,8 mm x 18 mm

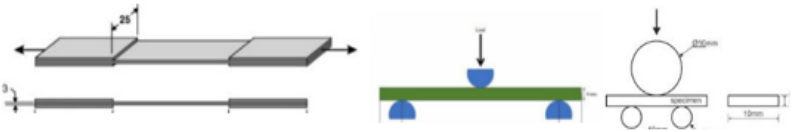

Figure 7. Tensile, three-point bending, and interlaminar shear test specimens

Glass fiber-reinforced polymer matrix composite materials were subjected to mechanical testing at 24 °C and 44% relative humidity. A 100 kN capacity Shimadzu universal testing machine was used for tensile, three-point bending, and interlaminar shear strength tests. Tensile specimens, prepared according to the dimensions given above and in accordance with ASTM D 3039, were tested at a strain rate of 2 mm/min. Five specimens were tested for each material group, and the average values were reported. For the three-point bending test, specimens were tested using the same universal testing

machine at a strain rate of 1 mm/min, with a support span of 51 mm, in accordance with ASTM D 790. For the Interlaminar Shear Strength (ILSS) test, specimens were prepared according to ASTM D2344 and tested at a strain rate of 1 mm/min with a support span of 12 mm.

3. Experimental Result and Discussion

In this study, the effects of different heating rates on the final curing behavior and mechanical properties of glass fiber-reinforced epoxy-based composites were experimentally investigated. First, DSC analyses were performed on the cured specimens, and the DSC outputs are presented in Figure 8. The heat flow–temperature curves shown in the figure indicate that the characteristic event in the low-temperature region is sensitive to the heating rate. According to the onset values provided by the software, the onset temperature was 113.3 °C for the specimen cured at 1 °C/min, while it was 116.7 °C for the specimen cured at 2 °C/min.

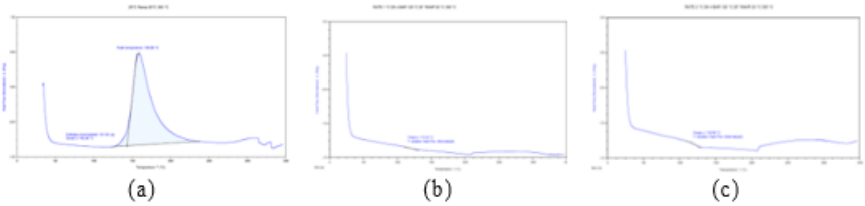

Figure 8. DSC curves of the (a) uncured prepreg and composites cured at heating rates of b) 1 °C/min and c) 2 °C/min

The stress–strain curves obtained from the tensile tests are shown in Figure 9. Accordingly, the average tensile strength and elastic modulus vary with heating rate, as illustrated in Figure 10. The study results indicate that reducing the heating rate during curing significantly improves the mechanical performance of composite specimens. Compared with the specimens cured at 2 °C/min, those cured at 1 °C/min demonstrated increases of approximately 8% in tensile strength and 7.9% in elastic modulus.

Based on the tensile test results, the standard deviations were 17 and 22, respectively, indicating that specimens produced at a lower heating rate yielded more consistent tensile test results. These findings suggest that a slower heating rate allows the resin to flow more effectively and fill voids more completely.

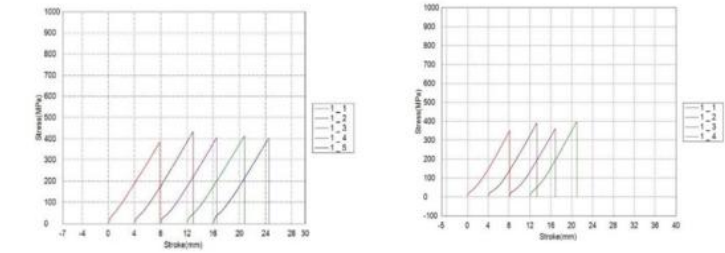

1 °C/min (b) 2 °C/min.

Figure 9. Stress–strain values of the composites cured at the different heating rates

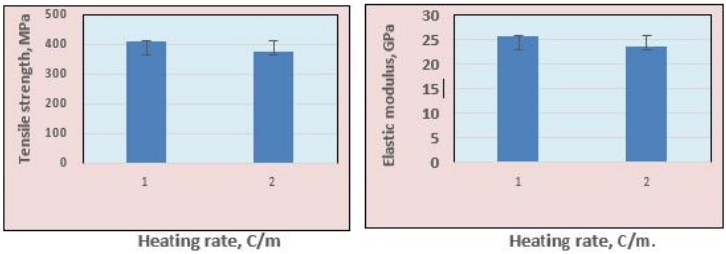

Figure 10. Tensile strength and elastic modulus values of the composites

Previous studies have shown that mechanical test results in composite materials are related to the extent of curing [15]. On the other hand, by maintaining the processing window for a more extended period, a more homogeneous bond at the fiber–matrix interface is expected to form, leading to improved mechanical properties [26,14,15]. ElKhoury et al. reported that a degree of cure of at least 95% is required; otherwise, the resin system exhibits low yield stress, reduced modulus, and decreased toughness, which can lead to early failure and poor adhesion [15]. Along with tensile properties, changes in heating rate also led to a significant increase in flexural strength, as measured by the three-point bending test. As shown in Figure 11, the force values obtained from specimens cured at 1 °C/min were higher than those from specimens cured at 2 °C/min. The average flexural strength was 458 MPa for the 1 °C/min specimen, compared to 419 MPa for the 2 °C/min specimen. The maximum flexural strains were 0.034% and 0.029%, respectively, indicating greater deformability in the specimen cured at the lower heating rate.

The maximum flexural stress and strain were also higher at the lower heating rate. A slower heating rate is believed to better control resin viscosity, ensuring complete fiber wetting, which in turn increases both flexural strength and interlaminar shear strength [27, 28].

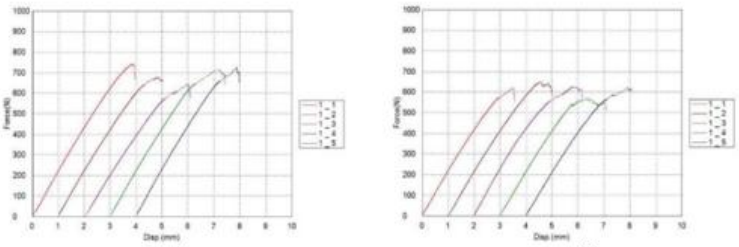

(a) (b)

Figure 11. Force–displacement curves obtained during the three-point bending test of composites cured at heating rates of 1 °C/min (a) and 2 °C/min (b)

The interlaminar shear strength (ILSS) of composite materials is presented in Figures 12 and 13. They indicate that an increase in the heating rate during the curing of composite materials causes a slight rise in interlaminar shear strength.

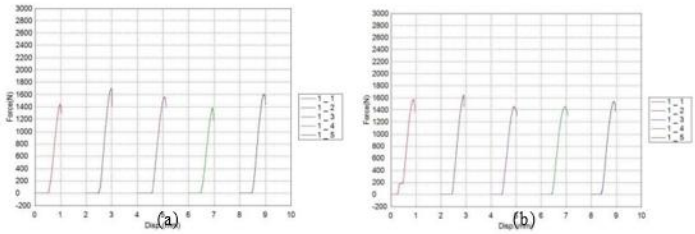

Figure 12. a) ILSS test graphs of composites cured at heating rates of 1 °C/min and 2 °C/min

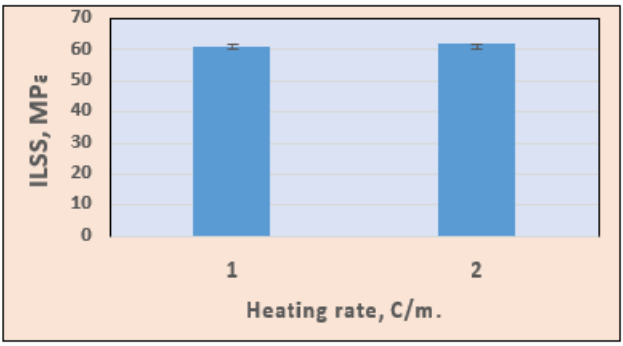

Figure 13. ILSS values of composites cured at different heating rates

4. Conclusion

Using E-glass reinforced epoxy prepreg material, specimens cured in an autoclave at 120 °C for 120 minutes were investigated to evaluate the effect of heating rate on DSC data, tensile strength, three-point bending strength, and interlaminar shear strength (ILSS). The following results were obtained:

- DSC analyses for both specimens showed similar thermal transition profiles at different heating rates. The glass transition temperature was determined to be

113.32 °C for the specimen cured at 1 °C/min and 116.7 °C for the specimen cured at 2 °C/min.

- Tensile test results indicated that the composite specimens cured at a heating rate of 1 °C/min exhibited approximately 8% higher tensile strength and elastic modulus compared to those cured at 2 °C/min.

- Increasing the heating rate from 1 °C/min to 2 °C/min resulted in decreases of approximately 8.5% in flexural strength and 14% in flexural strain.

- For interlaminar shear strength (ILSS), no significant difference was observed between the two materials, although specimens cured at 2 °C/min showed a slightly higher value by 1.8%.

Acknowledgments

We would like to sincerely thank Nurol Teknoloji and Mr. Burak Mert for their support in the composite preparation stage, as well as CES Kompozit and Mr. Eralp Akgün for their contributions to the testing process.

References

[1] Raju, A., & Shanmugaraja, M. (2021). Recent researches in fiber reinforced composite materials: A review. Materials Today: Proceedings, 46, 9291-9296.

[2] Chairi, M., El Bahaoui, J., Hanafi, I., Cabrera, F. M., & Di Bella, G. (2023). Composite materials: A review of polymer and metal matrix composites, their mechanical characterization, and mechanical properties. Next Generation Fiber-Reinforced Composites-New Insights.

[3] Ekuase, O. A., Anjum, N., Eze, V. O., & Okoli, O. I. (2022). A review on the out-of-autoclave process for composite manufacturing. Journal of Composites Sci-ence, 6(6), 172.

[4] Karaçor, B., & Özcanlı, M. (2021). Different curing temperature effects on mechan-ical properties of jute/glass fiber reinforced hybrid composites. International Journal of Automotive Science and Technology, 5(4), 358-371.

[5] Akın, M. (2018). Co-cured manufacturing of advanced composite materials using vacuum assisted resin transfer molding (Master's thesis, Middle East Technical University (Turkey)).

[6] Kumbhare, N., Moheimani, R., & Dalir, H. (2021). Analysis of composite structures in curing process for shape deformations and shear stress: Basis for advanced optimi-zation. Journal of Composites Science, 5(2), 63.

[7] Manral, A., Ahmad, F., & Sharma, B. (2019). Advances in curing methods of rein-forced polymer composites. Reinforced polymer composites: processing, characteriza-tion and post life cycle assessment, 77-104

[8] Abliz, D., Duan, Y., Steuernagel, L., Xie, L., Li, D., & Ziegmann, G. (2013). Curing methods for advanced polymer composites-a review. Polymers and Polymer Compo-sites, 21(6), 341-348.

[9] Ogugua, C. J., Anton, S. V., Tripathi, A. P., Larrabeiti, M. D., van Hees, S. O., Sinke, J., & Dransfeld, C. A. (2023). Energy analysis of autoclave CFRP manufacturing using thermodynamics based models. Composites Part A: Applied Science and Manufacturing, 166, 107365

[10] Yong, A. X., Sims, G. D., Gnaniah, S. J., Ogin, S. L., & Smith, P. A. (2017). Heating rate effects on thermal analysis measurement of T g in composite materi-als. Advanced Manufacturing: Polymer & Composites Science, 3(2), 43-51.

[11] Kumar, D. S., Shukla, M. J., Mahato, K. K., Rathore, D. K., Prusty, R. K., & Ray, B. C. (2015, February). Effect of post-curing on thermal and mechanical behavior of

GFRP composites. In IOP conference series: materials science and engineering (Vol. 75, No. 1, p. 012012). IOP Publishing.

[12] Perrin, H. F., D'Acunto, A., & Martin, P. (2010). Warpage of flat composite part induced by liquid resin infusion (LRI) processes.

[13] Collinson, M. G., Swait, T. J., Bower, M. P., Nuhiji, B., & Hayes, S. A. (2023). Development and implementation of direct electric cure of plain weave CFRP compo-sites for aerospace. Composites Part A: Applied Science and Manufacturing, 172, 107615.

[14] Warnock, C., & Briggs, T. (2016). Cure Cycle Development and Qualification for Thick-Section Composites (No. SAND2016-1048C). Sandia National Lab.(SNL-CA), Livermore, CA (United States).

[15] ElKhoury, L., & Berg, J. C. (2022). The effect of curing schedules on fiber-matrix adhesion in carbon fiber–epoxy resin composites. Journal of Composite Materi-als, 56(5), 699-712.

[16] Zhu, L., Wang, Z., Rahman, M. B., Shen, W., & Zhu, C. (2021). The Curing ki-netics of e-glass fiber/epoxy resin prepreg and the bending properties of its prod-ucts. Materials, 14(16), 4673.

[17] Voto, G., Sequeira, L., & Skordos, A. A. (2018, June). Heating rate limits in fast cure processing of thick carbon fibre laminates. In Proceedings of the ECCM—18th European Conference on Composite Materials, Athens, Greece (pp. 24-28).

[18] Herring, M. L., & Fox, B. L. (2011). The effect of a rapid curing process on the surface finish of a carbon fibre epoxy composite. Composites Part B: Engineer-ing, 42(5), 1035-1043.

[19] Davies, L. W., Day, R. J., Bond, D., Nesbitt, A., Ellis, J., & Gardon, E. (2007). Effect of cure cycle heat transfer rates on the physical and mechanical properties of an epoxy matrix composite. Composites science and technology, 67(9), 1892-1899.

[20] Dong, A., Zhao, Y., Zhao, X., & Yu, Q. (2018). Cure cycle optimization of rapidly cured out-of-autoclave composites. Materials, 11(3), 421.

[21] Kim, H. G. and Lee D. G. (2002). Dielectric cure monitoring for glass/polyester prepreg composites. Composite structures, 57(1-4), 91-99.

[22] Chang, T., Zhan, L., Tan, W., & Li, S. (2017). Optimization of curing process for polymer-matrix composites based on orthogonal experimental method. Fibers and Pol-ymers, 18(1), 148–154.

[23] Khan, L. A., Kausar, A., & Day, R. J. (2017). Aerospace composite cured by quickstep and autoclave processing techniques: Evaluation and comparison of reaction progress. Aerospace Science and Technology, 65, 100-105.

[24] Patel, A., Kravchenko, O., & Manas-Zloczower, I. (2018). Effect of curing rate on the microstructure and macroscopic properties of epoxy fiberglass composites. Poly-mers, 10(2), 125.

[25] Schlimbach, J., & Ogale, A. (2011, May). Quickstep: beyond out of autoclave curing. In Proceedings of the International SAMPE Technical Conference, Long Beach, CA, USA (pp. 23-26).

[26] Rusnáková, S., Krššák, P., & Ružbarský, J. (2024). Experimental Study on the Optimization of the Autoclave Curing Cycle of a Polymer–Matrix Composite for Improved Mechanical Properties. Polymers, 16(6), 1179.

[27] Miller, S. G. (2019). Evaluation of temperature gradients during cure of a thick carbon fiber/epoxy composite. NASA Technical Reports.

[28] Tang, W., et al. (2022). Multi-objective optimization of curing profile for auto-

clave processed composites. Composite Structures, 279, 114795. https://doi.org/10.1016/j.compstruct.2021.114795

[29] Beaumont, PWR Kompozit Malzemelerin Yapısal Bütünlüğü ve Kompozit Yapıların Uzun Ömürlü Uygulanması, Uygulamalı. Kompozisyon. Malzeme. 2020, 27, 449–478.

[30] Jones, R. M. (1999). Mechanics of Composite Mater. (2nd ed.). Taylor & Francis. [31] Talreja, R., & Singh, C. V. (2012). Damage and Failure of Composite Materials. Cambridge University Press

[32] Liu, Y., Xie, J., Chen, X., Zhang, J., Wan, M., Sun, Z., & Yang, C. (2025). Characterization of progressive damage behaviour and failure mechanism of carbon fiber reinforced composite laminates. Scientific Reports, 15, Article 13791.

[33] Basavaraj, Y., & Raghavendra, H. (2014). Experimental and numerical study of the influence of volume fraction on tensile and flexural strength of E-Glass epoxy Cross Ply Laminates. Int. J. Mech. Ind. Technol, 2(1), 39-44.

[34] Lee, S. G., Oh, D., & Woo, J. H. (2021). The effect of high glass fiber content and reinforcement combination on pulse-echo ultrasonic measurement of composite ship structures. Journal of Marine Science and Engineering, 9(4), 379.

[35] Tan, K. S., Guo, N., Wong, B. S., & Tui, C. G. (1995). Comparison of Lamb waves and pulse echo in detection of near-surface defects in laminate plates. NDT & E Inter-national, 28(4), 215-223.

[36] Nsengiyumva, W., Zhong, S., Lin, J., Zhang, Q., Zhong, J., & Huang, Y. (2021). Advances, limitations and prospects of nondestructive testing and evaluation of thick

composites and sandwich structures: A state-of-the-art review. Composite Struc-tures, 256, 112951.

[37] Mehdikhani, M., Gorbatikh, L., Verpoest, I., & Lomov, S. V. (2019). Voids in fiber-reinforced polymer composites: A review on their formation, characteristics, and effects on mechanical performance. Journal of Composite Materials, 53(12), 1579-1669.

Development of Fragment-Resistant Wall Against Explosion Effects Using Composite Technology by Recycling Plastic Waste

Cihangir Cebeci[1], Mahmut Uğur,[1] Ece Yaralı[1], Gözde Bostancı[1]

[1] Fiberr Fiber Reinforced Resin , Tirkeş, Sok No: 499/2, Saruhanlı/Manisa 45800, Türkiye AS,0009-0006-3116-4982

Mahmut.Ugur@fiberr.com.tr

Abstract: The increasing security needs in public buildings, military facilities, and communal living spaces necessitate the use of materials resistant to fragment impact that may occur as a result of potential explosions. The weight and cost of metallic and ceramic-based materials make it essential to develop lightweight, durable, and low-cost alternatives.The long-term presence of plastic waste in nature significantly harms ecosystems by degrading soil, water, and air quality; low recycling rates make the reuse of this waste a critical priority. In Turkey, the recovery of recycled materials is still at a low level and their use in the field of composites remains limited.This study aims to develop innovative new technologies that will convert recycled plastic-based composites into low-cost, environmentally friendly structural elements by subjecting them to dynamic load testing. With the methods developed, the project will produce lightweight and portable ballistic-resistant composites that offer environmental benefits and serve as an important model in this field.The components of the composite material, reinforcement ratios, and process parameters are optimized to maximize ballistic performance, and material prototypes are tested by customizing them according to various needs. Within the scope of the project, composite mixtures are created by blending recycled thermoplastic-based materials (PP and HDPE) containing varying ratios of short glass fibers and quartz sand in a screw extruder. Extruder parameters (temperature, time, etc.) are analyzed and optimized through systematic R&D approaches. The resulting mixtures are placed into cold press molds and shaped into structural block (brick) forms under pressure. The developed composite panels and structural blocks will be subjected to 1.1 g fragment (V50, FSP) tests in accordance with the NIJ 0101.06 standard. In addition, the samples will be examined through mechanical tests, thermomechanical tests, fracture surface analyses, and microstructural imaging.The developed materials will be applicable in the production of protective systems for military and civilian buildings, police stations, and trenches.

Furthermore, the production of domestic structural systems aimed at increasing safety in high-risk facilities such as explosive or hazardous chemical manufacturing plants will also become possible.

Keywords: Composite material, thermoplastic, fragment impact, protective shield, recycling, sustainability

1. Introduction

In recent years, increasing security requirements, particularly in public buildings, military facilities, and densely populated areas, have made it essential to employ construction materials resistant to fragment effects that may occur as a result of explosions. Traditional protective materials such as lead, steel, and ceramics provide high strength but have significant limitations in practical applications due to their heavy weight, toxic properties, and high costs [2].These drawbacks highlight the urgent need for lighter, more economical, durable, and environmentally friendly alternatives.

Meanwhile, plastic waste poses a serious environmental challenge as it remains in nature for long periods without decomposing, thereby degrading soil, water, and air quality and causing permanent damage to ecosystems. The low recycling rates of plastics further exacerbate this problem, making their reuse a critical requirement within the framework of sustainability and circular economy. In this regard, the utilization of recycled plastics in composite material technologies offers both environmental and economic benefits. Composites not only provide advantages such as light weight, high strength, and design flexibility but also reduce the carbon footprint when produced with recycled content, thus contributing to sustainable development goals.

A review of the literature shows that layered and hybrid composite structures can achieve ballistic resistance comparable to or even higher than that of conventional metal-based materials, while maintaining lower density [3]. In particular, the combination of high-performance fibers such as Kevlar, glass, and carbon in specific arrangements has been shown to significantly enhance energy absorption capacity [3]. Furthermore, surface modifications and binder systems (e.g., silane treatment, PP-g-MA, epoxy) play a decisive role in mechanical and ballistic performance [5]. Sandwich structures incorporating lightweight core materials such as aluminum foam demonstrate remarkable deformation behavior under blast loading, offering advantages for explosion-resistant designs. Additionally, composites reinforced with recycled plastics and natural fillers have emerged as promising alternatives from a sustainability perspective [4], as they combine low density,

good thermal insulation, and sufficient mechanical properties for use in the construction sector.

Although these studies demonstrate significant progress in ballistic protection, energy absorption, and sustainability, comprehensive research on transforming recycled plastic waste directly into structural blocks with ballistic resistance remains limited. In particular, optimizing matrix-to-reinforcement ratios, processing parameters, and recycling approaches to develop environmentally friendly yet high-performance construction materials constitutes a major gap in the literature. This study aims to address these shortcomings by developing a new generation of low-cost, lightweight, and fragment-resistant composite building blocks.

2. Materials and Methods

In this study, an innovative composite formulation was developed by utilizing recycled thermoplastic wastes (PP and HDPE) blended with short glass fibers and quartz sand as reinforcing agents. The primary objective was to design a lightweight, high-strength, and blast/fragment-resistant structural block, suitable for both civilian and military applications, while promoting sustainability and circular economy principles.

2.1 Material Preparation

Recycled plastic wastes were collected, sorted, cleaned, and converted into granules. These plastic granules were mechanically characterized to determine their thermal, chemical, and mechanical properties. Based on these evaluations, polypropylene (PP) and high-density polyethylene (HDPE) were selected as matrix materials. Short glass fibers and quartz sand were incorporated at varying ratios to enhance the mechanical integrity, energy absorption capacity, and thermal stability of the composite.

2.2 Composite Formulation and Mixing

The selected materials were compounded in a single-screw extruder under optimized process parameters (temperature, residence time, and screw speed). The extrusion process ensured homogeneous dispersion of fibers and sand particles within the polymer matrix, preventing agglomeration and enhancing interfacial bonding.

2.3 Shaping and Consolidation

The extruded blends were placed into cold press molds and consolidated under controlled pressure to produce composite structural blocks in brick-like geometries. Process optimization was achieved through iterative R&D trials, where different formulations and pressing parameters were systematically varied to improve ballistic resistance and structural durability.

Injection Temperature (°C)	Optimum Filling Time (s)	Surface Quality (1=poor → 5=excellent)	Notes
220	28	2	Insufficient filling → voids and rough surface.
240	20	3	Filling improves; surface becomes smoother.
260	14	5	Homogeneous filling, smooth surface, low void content.
280	8	4	Fast filling; however, risk of thermal degradation exists.

Table 1: Optimum Filling Time and Surface Quality Based on Injection Temperature

Clamping Force (ton)	Void Ratio (%)	Surface Roughness Ra(μm)	Surface Integrity Evaluation
250 t	3,5	5,6	Weak – surface contains noticeable pores.
300 t	2,3	3,8	Moderate – improved but lacks full consolidation.
350 t	1,2	2,1	Very good – homogeneous, low void content, smooth
400 t	1	2	Good – slight material flash; mold wear may occur.

Table 2: Effect of Mold Clamping Force on Surface Integrity

2.4 Testing and Standardization

The produced composite samples were subjected to basic mechanical and thermomechanical tests to evaluate their structural performance. Prototype blocks were also prepared to assess fragment resistance. Ballistic tests were conducted using fragment-simulating projectiles (FSP), and the ballistic resistance was evaluated according to the V50 ballistic limit methodology defined in the MIL-STD-662F standard [1]. In addition, basic microstructural and fracture surface observations were performed to examine the behavior of the composite material after testing.

2.5 Innovation and Environmental Impact

The developed process not only ensures the upcycling of plastic wastes into high-value composites, but also contributes to cost reduction, carbon footprint minimization. By replacing heavy metallic/ceramic solutions, the produced blocks provide lightweight, eco-friendly, and transportable alternatives, setting a new benchmark for protective structures in both civilian and defense sectors.

3. Results and Discussions

Within the scope of this study, composite blocks were produced using a formulation consisting of recycled plastics, short glass fibers, and quartz sand. The total reinforcement content was determined as 70 ± 2 wt.%, verified through material proportion measurements during the mixing stage. Using extrusion and pressing techniques, the porosity ratio of the blocks was maintained below 5%, and a relatively homogeneous fiber distribution was observed in the produced samples.

Mechanical tests were conducted to evaluate the performance of the developed composite material. All tests were performed on five specimens (n = 5), and the results are reported as mean ± standard deviation. Tensile tests indicated high stiffness and strength values. Flexural tests resulted in a flexural strength of 72 ± 3 MPa, while compression tests showed a compressive strength of 152 ± 5 MPa. Impact tests yielded Charpy impact strength of 68 ± 4 kJ/m² and Izod impact strength of 65 ± 3 kJ/m². In addition, fracture toughness measurements showed a Mode-I interlaminar fracture toughness (GIC) of 2.1 ± 0.2 kJ/m², indicating stable crack propagation behavior.

Additional Performance Tests: Thermal resistance tests showed that the composite blocks remained stable under high-temperature conditions, while chemical resistance evaluations indicated robustness against water, acids, and other aggressive environments.

In conclusion, the fabricated prototype composite blocks successfully met the targeted performance criteria in ballistic, mechanical, and environmental durability. The optimized formulation and integrated production methods demonstrated that these blocks can serve as a strong and sustainable alternative to conventional security materials.

4. Conclusions

In conclusion, the produced prototype structural blocks were shown to meet the targeted performance criteria in terms of ballistic, mechanical, and environmental resistance, offering a strong alternative to conventional protective materials through optimized formulations and manufacturing methods. This study has demonstrated the applicability of recycled plastic-based composites in the security and defense sectors. When ballistic tests, mechanical performance evaluations, and microstructural analyses are considered together,

it is evident that the developed material provides a significant alternative from both an environmental and structural perspective. Compared to conventional metal-based solutions, these new composites are lighter, more portable, and cost-effective, making them strong candidates for the production of protective structural elements against blast and fragment impacts. Furthermore, the study highlights that plastic waste can be transformed into high value-added products through advanced recycling techniques, thereby contributing to environmental sustainability goals while also enhancing domestic production capacity.

Future studies will focus on exploring different reinforcement combinations, employing advanced modeling and design approaches for performance optimization, and scaling up to industrial manufacturing processes. In this context, the outcomes of the project are expected to move beyond laboratory-scale achievements and evolve into large-scale practical applications.

References

[1] U.S. Department of Defense, *MIL-STD-662F: V50 Ballistic Test for Armor*, Department of Defense Test Method Standard, 1997.

[2] Wang, J. (2017) Blast response of polymer-retrofitted masonry unit walls. *Composites Part B: Engineering,* 128, 174-171.

[3] Ustün, H. S., Toksoy, A. K., & Tanoğlu, M. (2022). Investigation of hybridization effect on ballistic performance of multi-layered fiber reinforced composite structures. *Journal of Composite Materials, 56*(15), 2411–2431.

[4] Gonzalez, L., & Martinez, R. (2023). Sustainable Applications of Recycled Plastics in Construction and Automotive Industries. *Journal of Sustainable Materials*, 47(1), 89-112.

[5] Tanoğlu, M., & Seyhan, A. T. (2003). Investigating the effects of a polyester preforming binder on the mechanical and ballistic performance of E-glass fiber reinforced polyester composites. *International Journal of Adhesion and Adhesives*, 23(1), 1-8.

Comparative Study on the Effect of Various Calcium Carbonates on the Properties of Solvent-Based Coatings

Dursun AYDIN[1][0009-0004-4254-0475– ORCID ID], Nilay GİZLİ[2][0000-0002-7591-1365- ORCID ID]

[1] Kansai Altan Boya Sanayi A.Ş., Quality Operation Department, Kemalpasa, Izmir

[2]Department of Chemical Engineering, Ege University, Izmir, Turkey

dursun.aydin@kansai.altan.com.tr nilay.gizli@ege.edu.tr

Abstract: Calcite (calcium carbonate, $CaCO_3$) is utilized in numerous applica-tions and is also preferred as one of the primary raw materials for paint produc-tion due to its various advantages. In paint production processes, it is known that the morphological and chemical structure of calcite can affect the desired crush-ing fineness of the paint, the homogeneous mixing of calcite in the paint (for-mation of agglomeration structures), and the agglomeration and aggregate for-mation of calcite in the paint and particle defect. Many properties, including dis-persion, morphology, structure, and particle size, are associated with the applica-tion of calcite particles in a composition. (Liu, Wang, Xiang, 2008) In this study, the effect of calcites with different morphologies on the performance of solvent-based primer paint was investigated. Calcites with different properties were first examined for their chemical composition and crystal structure using XRD, and their morphological properties were analyzed by SEM and BET analysis. In ad-dition, particle size distribution values were determined for each calcite sample. Then calcites with distinct chemical and morphological properties were incorpo-rated into solvent-based primer paint formulations. Nine distinct calcite samples from three different sources and six different calcite types were used in the labor-atory-based paint production process. The effect of different calcites on disper-sion quality and paint behavior was investigated. In addition, a study was con-ducted to determine how the type and amount of wetting agents affect the perfor-mance of the paint. A series of experiments were conducted on paint samples prepared with calcites of varying morphologies. The experimental parameters in-cluded density, grinding fineness, viscosity, hardness, gloss, surface application by spray method, applicator application to glass surfaces, and stability control. A study was conducted to determine the effect of different types of calcites on hardness, viscosity, and viscosity increase.

Keywords: Calcium Carbonates, Solvent-Based Coatings, Calcium Carbonates Morphology

1 Introduction

Calcium carbonate (CaCO3), one of the most abundant minerals, constitutes approxi-mately 4% of the Earth's crust and exists in three distinct forms: aragonite, vaterite, and calcite (Liu et al., 2008). Calcite is one of the main raw materials for paint production and is used for purposes such as adding viscosity to paint and optimizing costs. Calcite is a rhombic-structured limestone that is ground to create this mineral powder, which is a common filler in the paint industry (Tunçgenç, 2004). Many polymer composites use calcite as a filler because it is inexpensive, readily available, nontoxic, tasteless, and nonirritating (Ersoy et al., 2021) With a Mohs hardness of 3, a refractive index of roughly 1.70, and a density of over 2.7 g/cm3, calcite is a valuable and inexpensive industrial mineral that is frequently used as a ground form in a variety of industries, including plastic, paper, and paint (Ulusoy et al., 2023). In paint production processes, it is known that the type and morphology of calcite have an impact on the dispersion quality and fineness of paint grinding. Several properties, including dispersion, mor-phology, structure, and particle size, are related to the use of calcite particles (Liu et al., 2008). The paint business requires a wide range of raw ingredients and is a very active industry in terms of advancements in formulation. Between 20% and 50% of the paint mix is made up of mineral additives. When compared to TiO2, which requires the em-ployment of many chemicals, the production method for calcite is likewise straightfor-ward. Thus, any potential replacement of calcite in the paint formulation with TiO2 will undoubtedly have benefits for the environment as well as the economy (Karakaş, F., and M. S. Çelik. 2012). Although some properties of calcite such as particle size distri-bution and refractive index are not comparable in quality to TiO2, calcite can improve the distribution of TiO2 via its interaction with TiO2 particles (Karakas¸ 2012). The paint's gloss, opacity, viscosity, and storage stability, on the other hand, are all impacted by the pigment dispersion condition (Ersoy at.al, 2021).

Calcite offers many advantages in the paint industry. These include strengthening prop-erties, controlling viscosity, reducing costs by reducing titanium dioxide consumption, increasing opacity thanks to its high whiteness, providing gloss to paints, and prevent-ing the flow of film paints by imparting viscosity to paints.

In this study, the effects of calcites with different morphologies and particle size distributions on the rheological properties and overall performance of a solvent-based primer paint were investigated. Paint formulation was prepared using resin, fillers (calcite and other fillers), pigment, solvent and additives. Paint production was conducted under laboratory conditions using nine different calcite samples obtained from six calcite types and three different sources. The experimental study was conducted through three main approaches and plans were established. Firstly, the effect of different calcites on the performance and behavior of the paint was investigated. In the second test plan, different wetting agents were incorporated into the paint formulation to examine their influence on the dispersion quality and overall performance of the paint. Lastly, the amount of the selected wetting agent was increased to assess the impact of the amount of wetting agent on the overall paint system. Two different types of wetting agents were employed in the paint formulations. The first type acts as a bridge between the pigment and the binder by absorbing onto the pigment surface thereby preventing the pigments settling. Its mechanism of action resembles that of a rheological modifier although its steric effect is lower compared to polymeric dispersing agents. The second wetting agent provides uniform equal electrical charge to pigment particles preventing the co-flocculation of pigments that are differently charged. In summary, differences in calcites particle sizes and morphology can considerably influence the hardness of the paint, viscosity and the rate of viscosity increase.

2 Materials and Methods

2.1 Paint Raw Materials

Calcium carbonate

Nine distinct calcite samples from three different sources and six different calcite types have been used in the laboratory-based paint production process. The mean particle size of calcite samples used in this study varied from 9.04 to 15.20 µm at D99. Particle size distribution values are given in Table 1.

Table1. Particle size distribution of calcite samples

	D10 µm	D50 µm	D90 µm	D99 µm	D100 µm
SAMPLE A	1.35	3.78	8.20	12.20	14.40
SAMPLE B	0.95	3.03	6.45	9.60	11.20
SAMPLE C	1.02	3.04	6.23	9.04	11.20
SAMPLE D	1.32	3.75	7.99	11.80	14.40
SAMPLE E	1.33	4.19	9.72	14.80	18.60
SAMPLE F	1.33	4.17	9.87	15.20	18.60
SAMPLE G	1.47	3.84	8.08	11.80	14.40
SAMPLE H	1.58	4.15	8.89	13.20	16.40

Other raw materials

Resin, fillers, pigment, solvent and additives have been used in the preparation of the paint formula. Each raw material for paint production has been supplied by leading companies in the industry.

2.2 Paint Formulation and Production

The paint was produced with a high-speed stirrer operating at 5,000 rpm. The same processing conditions were used for all laboratory-scale paint samples. It was intended that calcite variability was the sole factor influencing the behavior of the paint samples. The duration of the mixing process, the approximate dosage rate of the raw materials, and other pertinent factors were maintained constant for all samples. Firstly, the impact of various calcites on the paint's behavior and performance was examined. Different wetting agents were incorporated in to the paint formulation in the second test plan to investigate their effects on the paint's overall performance and dispersion quality. Paint production steps are given in Figure 1. Additionally, Figure 2 shows the images of the paint production stages.

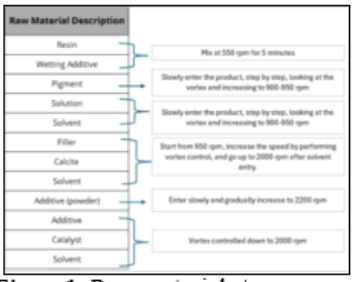

Figure1. Raw material steps

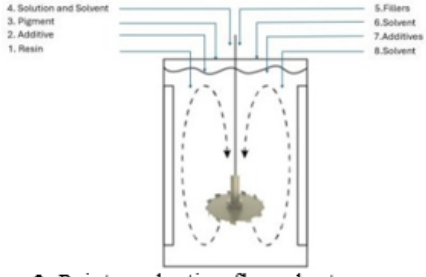

Figure 2. Paint production flow chart

The temperature of the product was also monitored during the paint preparation steps.

Figure 3. Images from paint production stages

1.3. Physical and Mechanical Properties of Paint Samples

The performance and behavior of paint samples produced with different calcites were investigated. Some evaluations were carried out to examine the effect of different cal-cites on the physical and mechanical characteristics of the paint.

Evaluations such as viscosity, glass surface evaluation, hardness of the paint film, gloss and spray application to the wooden surface were carried out. The amount of calcite in the paint formula remained constant and the solids content was adjusted to approxi-mately 77%

due to the different calcite types. Viscosity measurements were conducted on paint samples whose solids content was adjusted to the desired value in accordance with DIN 6 standards. Surface inspections were performed with a glass surface to de-termine the presence of any grain problems in the wet samples. Additionally, the hard-ness of the paint film was evaluated. Prepared paint samples were adjusted to the ap-plication viscosity and spray applied. After the paint film was cured, gloss measure-ments were taken. Figure 3.

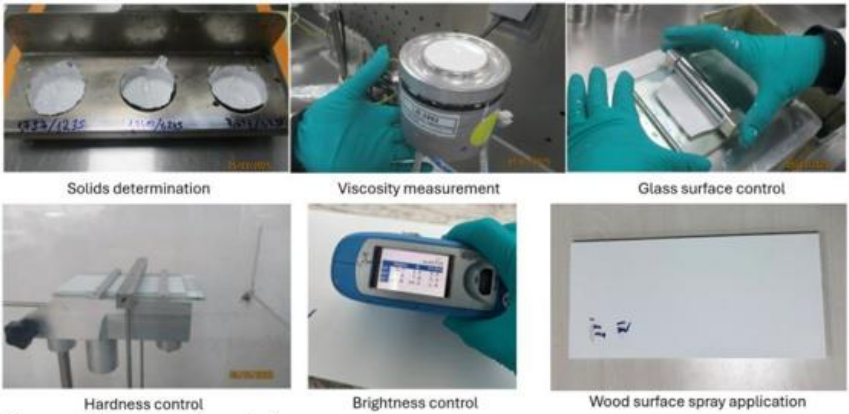

Figure 4. Images of controls

2.4 Characterization of Raw Material and Paint Analysis

Some analyses were made for the raw material (calcite) and the final product (paint) to determine the different behaviors of the produced paints. To understand the differences between calcite types, particle distribution, X-ray diffraction (XRD), Brunauer-Em-mett-Teller (BET) analysis, scanning electron microscopy (SEM) and SEM- EDX ele-mental analyses were performed. XRD analysis was performed on a Panalytical X'Pert Pro / Cu cathode ray tube / x'celerator detector device. Scanning speed is 0.016 de-grees/min. Measurements were made between 3 and 70 degrees. Evaluation was carried out using the Rietveld quantitative method using High Score Plus software. BET anal-ysis was performed on a Micromeritics TriStar II instrument. Degas temperature was 240°C and degas time was 24 hours. Pressure range (P/Po) was between 0 and 1. Anal-ysis temperature was 77 K. Rheology analyses were performed on the rheogram to un-derstand the differences in dye. Details regarding these analyses are discussed in the results and discussion section.

3 Results and Discussions

3.1 Characterization of calcium carbonate

SEM-EDX analysis EM images of calcite samples are given in Figure 4.

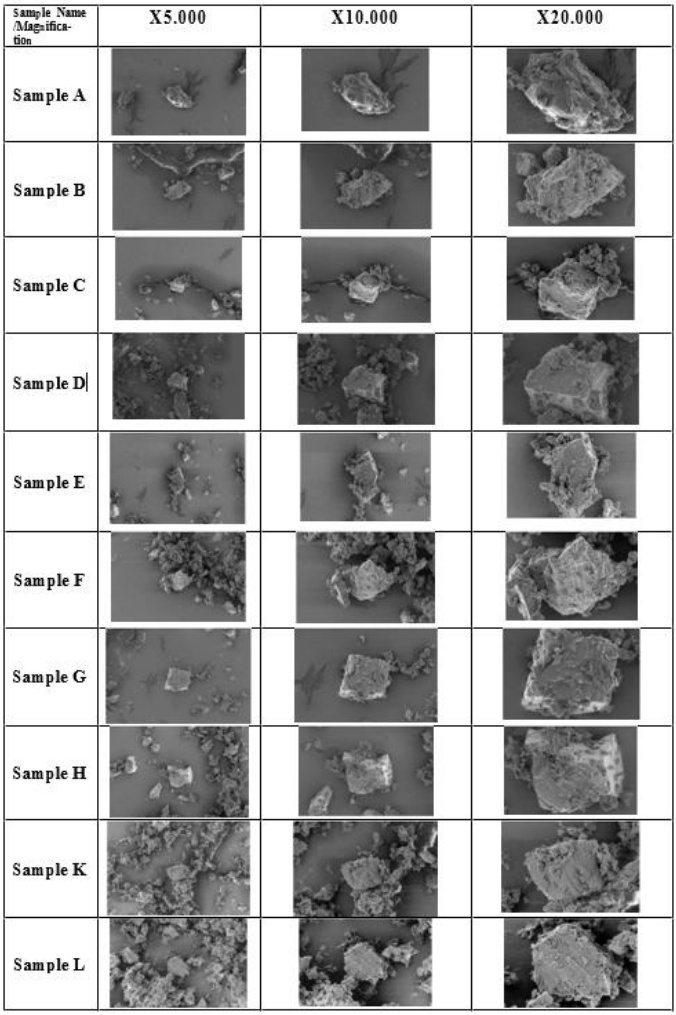

Figure 5. SEM imagines of calcite samples

Some differences can be observed in the SEM images of the calcite samples. Aggregate structures are observed in all calcite samples, although their intensity varies. The sam-ples with the highest concentration of aggregates are B, E, F, and K. Sample D can be observed to have the least aggregate structure. Samples A and B appear to have coarser grains compared to the other samples. Samples D, F, G, and H are observed to have sharper edges and more angular crystal structures. Crystals in samples K and L appear to be thinner, more layered, and more aggregated. Sample D is observed to have the lowest surface roughness, while sample A is observed to have the highest surface roughness.

SEM-EDX analysis was performed to detect impurities in calcite samples. Particle size analysis was not performed because sample K belongs to a different batch of product B, and sample L belongs to a different batch of product A. Therefore, the particle size distribution of sample K and product B, and sample L and product A, are expected to be similar.

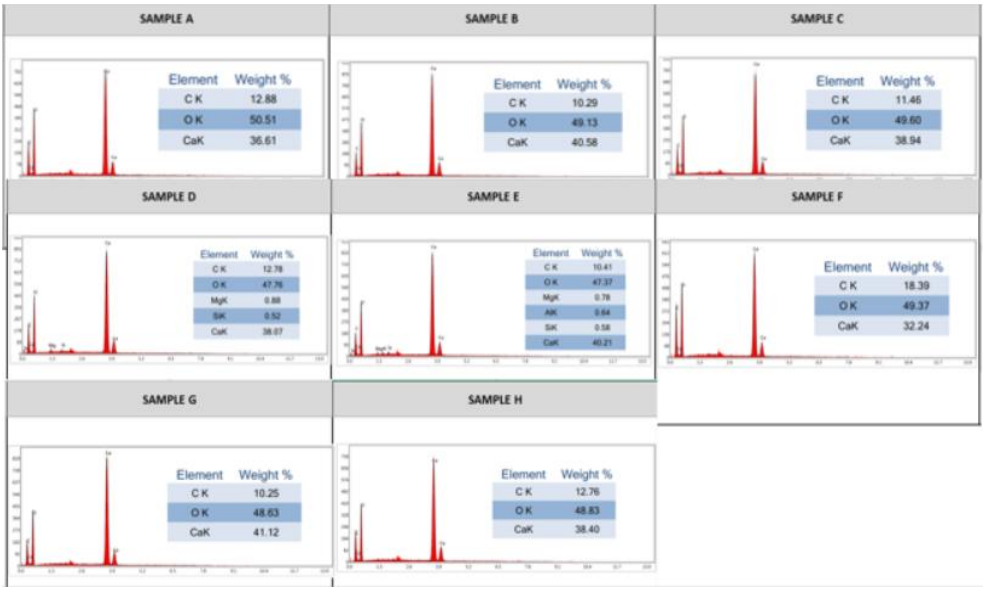

Figure 6. EDX results of calcites

A summary table of SEM-EDX results is given in **Table 2.**

Table2. Summary table of SEM-EDS analysis results of calcite samples.

SAMPLE NAME	C K (%)	O K (%)	Ca K (%)	Mg K (%)	Si K (%)	Al K (%)
A	12.88	50.51	36.61	-	-	-
B	10.29	49.13	40.58	-	-	-
C	11.46	49.6	38.94	-	-	-
D	12.78	47.76	38.07	0.88	0.52	-
E	10.41	47.37	40.21	0.58	0.58	0.64
F	18.39	49.37	32.24	-	-	-
G	10.25	48.63	41.12	-	-	-
H	12.76	48.83	38.40	-	-	-

Ca, C and O are the dominant elements in all samples, which are consistent with the calcite character. If we rank the calcite purity by looking at the calcium ratio, the rank-ing is G, B, E, C, H, D, A, F, respectively. Sample F contains a remarkably high carbon (18.39%) and low calcium (32.24%) content. This indicates that this sample has the highest impurity content among the samples, and the impurity content of sample F was remarkable. Mg, Si, and Al were detected in samples D and E. This suggests the pres-ence of dolomite ($CaMg(CO_3)_2$) contamination or a mixture of clay minerals (contain-ing Si and Al). These impurities may negatively affect the color, durability, or disper-sion properties of the paint.

X-ray diffraction (XRD)

In this study, XRD analysis was performed to obtain information about the chemical composition and crystal structure of the material. XRD results are given in Figure 6.

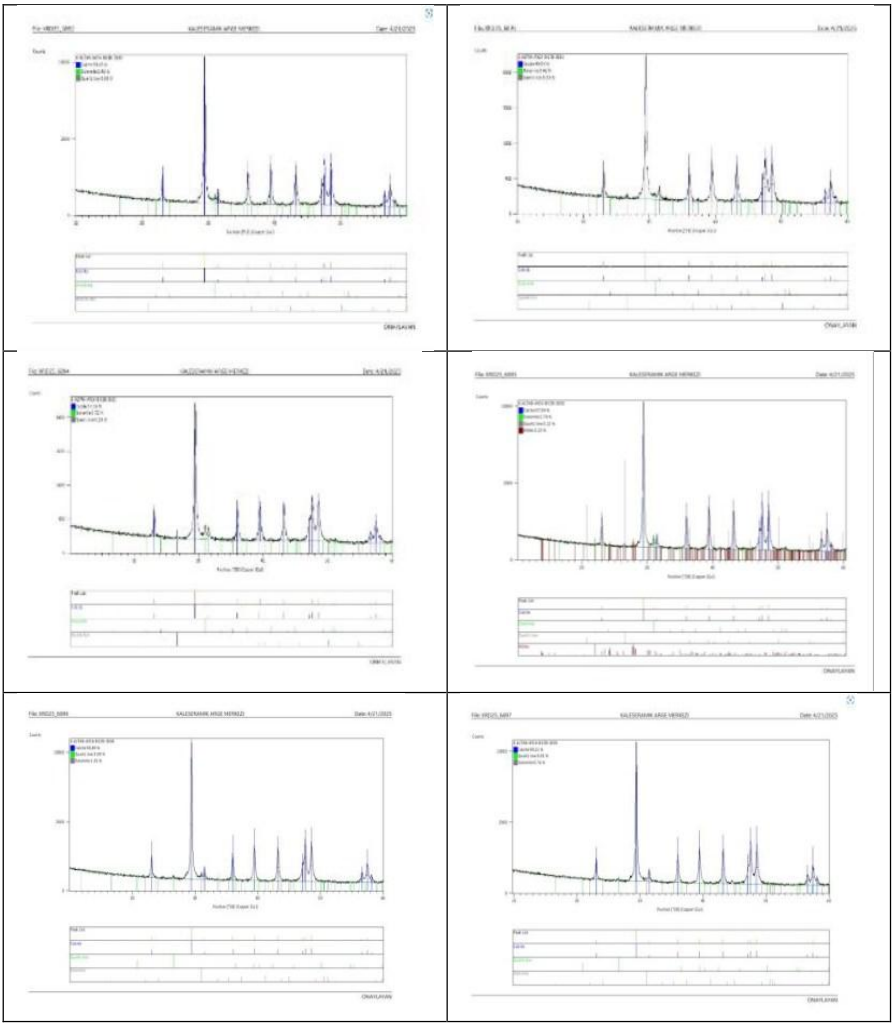

Figure 7. XRD analysis graph of calcite sample

The positions and intensities of the XRD peaks correspond to the calcite ($CaCO_3$) min-eral, which has a rhombohedral crystal system. Low amounts of dolomite and quartz are observed in all calcite samples. The samples' excellent quality, good crystallinity, and fine grain size are indicated by the sharp and narrow Bragg peaks (Marshall et al., 2024). Considering calcite (CaCO3) has a trigonal crystal structure and is a member of the hexagonal crystal system, the XRD peak analysis verified the presence of calcite in all samples (Sun et al., 2014).

N_2 Adsorption Analysis

Brunauer Emmett Teller (BET) surface area values of calcite samples obtained from N_2 adsorption isotherms are tabulated on Table 3.

Table3. N2 adsorption analysis results of calcites

Sample Name	BET Surface Area (m^2/g)	Sample Name	BET Surface Area (m^2/g)
A	1.6240	F	2.3202
B	3.5486	G	0.9842
C	0.8506	H	-1.0532
D	2.6820	K	2.2649
E	3.3682	L	-0.4469

3.1.4 Investigation of the rheological behavior of the paint

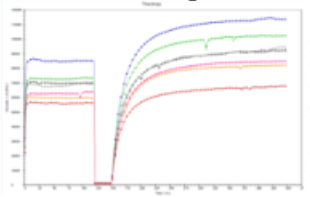

Figure 8. Time vs Viscosity diagram

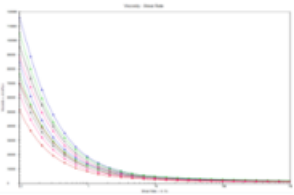

Figure 9. Shear Rate vs Viscosity diagram

The rheological behavior of the paint samples was investigated. As seen in Figures 7 and Figure 8, although the viscosities of the paint samples differ, their rheological be-havior is similar. Although the shape and particle size of calcites used as fillers in alkyd-based paint systems may affect rheological qualities, this effect seems to be limited on a macro scale when the entire formulation and filler volume are kept constant. This work shows that the alkyd resin phase mostly controls the system rheology due to the similar

behavior of the time-viscosity and shear rate-viscosity curves of paints made with calcites of various morphologies and particle sizes. It is believed that this mecha-nism is preserved since the effective volume fractions of the filler particles under con-stant PVC circumstances are similar.

3.2 Effect of various calcium carbonates on the paint performance

Three main approaches were used to conduct experimental study, and plans were es-tablished. First, the impact of various calcites on the paint's behavior and performance was examined. Different wetting agents were added to the paint formulation in the sec-ond test plan to investigate their effects on the paint's overall performance and disper-sion quality. Finally, to evaluate the effect of the wetting agent amount on the entire paint system, the amount of the chosen wetting agent was increased. The results of each study are given in Table4, Table5 and Table6, respectively. Paint samples made with various calcites were examined for performance and behavior. To investigate how var-ious calcites affected the paint's mechanical and physical properties, a few tests were conducted. Paint film hardness, viscosity, solid matter, grinding fineness, density, brightness, glass surface control, viscosity increase rate control and spray application to the wood surface were among the controls that were implemented.

Effect of Calcite (First test plan results)

Table 4. Solid Matter and Hardness results in first test plan

Calcite Samples	Solid Content Amount (%) 1h 120°C	Hardness Test with Per-soz 90µ Applicator and Glass Surface, 50°C 2h
A	77.50	123
B	77.69	110
C	77.89	118
D	77.93	115
E	77.76	105
G	77.25	141
H	77.32	115

The solids of all paints produced with calcite samples are similar. This similarity was deliberately adjusted during the experimental plan. The input quantities of all other raw materials, including calcite, were kept constant during the preparation of the paint formulas. The theoretical calculations and the solids calculations obtained after formula production are observed to be parallel. Because the solids measurements of all paint samples are precise, and although the paint is expected to be homogeneous, due to its colloidal structure, slight differences after the decimal point are considered normal. Therefore, the results can be considered similar.

Post-application hardness checks on paint samples revealed that sample G differed from the other samples and was higher. A difference of 5-10 units between the other samples can be considered similar. The high hardness of sample G can be explained by the purity of the calcite sample. SEM-EDX results indicate that sample G has the high-est Ca content. Unlike samples D and E, no impurities were observed in sample G, and sample G had the highest Ca content.

evaporation parameters during and after the paint production stage, as well as the evap-oration of the solvent during mixing. The viscosity results of the paint samples show differences. These differences may be due to several factors. All raw material inputs except calcite are the same. Therefore, there are two parameters that can affect viscos-ity. The first is the differences in the particle distribution and structure of the calcite. The second parameter is the effect of process parameters in the paint production pro-cesses. Process parameters were kept identical for all paint productions. Therefore, the effect of process parameters is ignored. At this point, the differences in viscosity due to differences in calcite were evaluated based on solvent evaporation parameters during and after the paint production stage. Except for Sample B, the differences in viscosity between four and ten seconds in the paint samples are not significant differences. These differences can be considered similar due to repeatability and oscillations during the measurement processes.

The viscosity of the paint samples was measured again at two-week intervals. The primary reason for this measurement is that particles within the paint tend to aggregate over time, and these aggregated particles accumulate at the bottom. Although the par-ticles are thought to be coated with wetting agents, they form agglomerations under the influence of physical forces. These agglomerations increase the paint's viscosity. There-fore, a time-dependent viscosity increase is observed.

As shown in Table 1, samples B and C have the lowest particle size distribution. Sample E has the highest particle size distribution. It can be said that the viscosity of the paint sample coded E is higher than the other paint samples due to its higher particle size. After four weeks, sample E has the highest viscosity.

Although the particle size distribution of sample B was similar to sample C, its vis-cosity was found to be much lower. After four weeks, their viscosities reached a similar point. The reason for this was investigated. Theoretically, the lower viscosity of sample B, while all parameters were the same, can only be explained by one reason. The sudden drop is suspected to be due to the solvent being added more rapidly during the viscosity adjustment phase of sample B compared to other paint production methods.

Table6. Percentage of viscosity increase of paint samples in first test plan

Calcite Samples	Percentage of viscosity increase between the first measurement and the measurement after 2 weeks (%)	Percentage of viscosity increase between the first measurement and the measurement after 4 weeks (%)
A	110.7	Measurements could not be taken because it showed thixotropic behavior.
B	63.5	150.0
C	35.2	70.1
D	29.7	72.3
E	35.3	80.0
G	42.9	64.6
H	3.6	35.7

Viscosity development is found to be substantially correlated with the BET surface area and BJH pore surface area of the calcites when paints made with all pro-duction parameters held constant and just the kind of calcite changed are assessed collectively. Although acceptable viscosities were originally obtained, the alkyd resin adsorbed more into the calcite surface and pores in samples B, D, and E, which have the largest BET surface area (particularly B and E). This led to notable increases in viscosity in the second and fourth weeks.

The quick increase in viscosity over time and the development of a thixotropic structure in sample A demonstrate that the porous struc-ture is at least as important in rheology as BET in samples with high pore surface area (BJH), even if the BET value is substantially lower (such as samples A and C). In con-trast, the viscosity increase was more controlled and stable in samples G and particu-larly H, which have low BET and BJH values, and the resin-filler interaction remained restricted. Overall, the findings unequivocally demonstrate that viscosity stability in paint systems is not exclusively dependent on the BET surface area; rather, the total active surface area and pore structure of the calcite should be taken into account jointly, and that calcites with a high surface/pore area carry a risk of increased viscosity and rheological stability over time.

A time-dependent viscosity increase was observed in all paint samples. The theoret-ical basis for this phenomenon was investigated. The product formula contains alkyd resin. Due to the unsaturated fatty acids in their structure, alkyd resins oxidize over time, forming O–O radicals and partially cross-linking molecules, resulting in an in-crease in molecular weight. This, in turn, causes an increase in viscosity. The second factor is the adsorption of the resin by calcite. The resin chains adsorb onto the filler surface, reducing the free movement of the resin. Viscosity increases with the agglom-eration of calcite particles and other powdered materials within the product.

The third factor is solvent adsorption and the change in the effective solvent ratio over time. Aromatic solvents adsorb onto calcite surfaces, creating a solvent-poor environment. Furthermore, some solvent evaporates during paint handling. An increase in viscosity is expected due to the amount of evaporated solvent and the solvent adsorption by the fillers. The mechanism by which calcite increases paint viscosity is as follows. In sol-vent-based paint, the interaction between particles results in a semi-easy-flowing parti-cle network due to reduced free solvent volume and solvent/resin adsorption. Calcite particles can come close together in dispersion, forming weak agglomerations or phys-ical networks. This structure impedes solvent flow and limits the free movement of resin chains, increasing viscosity.

Table7. Grinding Fineness, Density, Brightness and Paint control on glass surface with 120µ applicator application results of paint samples

Calcite Samples	Grinding Fineness (µ)	Density (g/cm^3)	Bright-ness 60° (Gloss)	Paint control on glass surface with 120µ applicator application
A	50-60	1.59	8.1	OK
B	60	1.59	8.1	OK
C	50-60	1.60	8.5	OK
D	60	1.60	7.3	OK
E	60	1.58	7.2	OK
G	50-60	1.59	8.4	OK
H	60	1.59	7.5	OK

The D99 particle sizes of the calcite samples varied between 9 and 15 microns. The crushing fineness of the paint samples was observed to be in the range of 50-60 microns. Based on the test results, this difference was not considered a qualitative difference and was interpreted as similar. The densities of all paints were similar. Although numerical differences were observed in the gloss results, there were no visible differences. The numerical differences in gloss are believed to be due to the whiteness of the calcite samples. Inspections on the glass surface revealed that all paints exhibited similar be-havior and no particle problems.

Preliminary results from the first test plan indicate that trace differences in paint hardness are observed under conditions where all parameters and raw materials used remain constant except calcite. Calcite type was found to influence to hardness of the paint. Noticeable variations in viscosity of paint samples were also recorded among samples produced with different calcite types. However, the crushing fineness and den-sity results were similar across all samples and only slight difference were noted in the gloss measurements.

An increase in efficiency and mechanical resistance can be observed with in-creasing calcite content in the paint (Kartal, 2024). In this study, the amounts of calcite used in the paint formulation are fixed. The reason for the differences in the hardness of the paint samples can be explained by the fact that the grain size of the calcite sam-ples affects the hardness of the paint (Ersoy at all, 2021). The increase in viscosity over time can be explained by the agglomeration of particles within the paint due to physical forces, leading to an increase in viscosity. The time-dependent increase in viscosity of the paint can be caused by polymer bridges that form between the TiO2 particles coated with high-density polymer, contrary to the steric repulsion effect, leading to agglomer-ation. This results in an increase in viscosity (Karakaş, 2011). It is observed that there is a linear trend in the values of calcite amount differences (Karakaş, 2011).

To evaluate viscosity stability of the paints, two measurements were taken at different time intervals. The rate of viscosity increases varied among the paint samples. Sample A exhibited the highest rate of viscosity increase showing thixotropic behavior in the second measurement), while sample H exhibited the lowest increase rate.

Effect of wetting agent (Second test plan results)

Table8. Solid Matter and Hardness results in the second test plan

Calcite Samples	Solid Matter Control 1h 120°C	Hardness Test with Persoz 90µ Applicator and Glass Surface, 50°C 2h
E	77.94	108
L	77.01	126
K	77.99	106

As in the first test plan, the solids were kept constant in the second test plan. The hardness values of samples E and K are similar. The hardness result of sample L was found to be higher than the other two samples.

Table9. Viscosity results of paint samples in the second test plan

Calcite Samples	Viscosity Control (initial control) DIN6, 20°C 125-150	Viscosity Control (After 2 weeks) DIN6, 20°C 125-150	Viscosity Control (After 4 weeks) DIN6, 20°C 125-150
E	192	217	230
L	183	195	197
K	162	182	186

It was observed that the viscosity results of samples E, L and K were different. In the second test plan, a different wetting agent was used than in the first. The effect of this wetting agent

on viscosity and its effect on the increase in viscosity over time were also investigated. The mechanism of the wetting agent in the first test plan is as follows: It acts as a bridge between the pigment and the binder by enveloping the pigment/filler surface, preventing pigment sedimentation. The mechanism of this wetting agent is more similar to a rheology additive. Its steric effect is not as high as that of polymeric dispersing agents. In the second test plan, the wetting agent's mechanism is as follows. It provides equal electrical charge to the pigments, thus preventing the flocculation of unequally charged pigments. It also wets the powders thoroughly and prevents other pigments or calcite particles from coming together. The important issue in this test plan is to examine the viscosity increase with time when the wetting agent is changed.

Table10. Percentage of viscosity increase of paint samples in the second test plan

Calcite Samples	Percentage of viscos-ity increase between the first measurement and the measurement after 2 weeks (%)	Percentage of viscosity increase between the first measurement and the measurement after 4 weeks (%)
E	13.0	19.8
L	6.6	7.7
K	12.4	14.8

The wetting agent used in the second test plan was found to exhibit better perfor-mance in increasing viscosity over time. In the first test plan, the rate of increase in viscosity in the fourth week was between 35% and 150%, while in the second test plan, the rate of increase in viscosity was approximately 8% to 20%. The reason for this is that the wetting agent surrounds the powder structures, resulting in more stable samples, and it appears to have a more positive effect on the increase in viscosity over time.

Table11. Grinding Fineness, Density, Brightness and Paint control on glass surface with 120µ applicator application results of paint samples in the second test plan

Calcite Samples	Grinding Fineness (µ)	Density (g/cm3)	Brightness 60° (Gloss)	Paint control on glass surface with 120µ applicator application
E	60	1.59	9.3	OK
L	60	1.59	8.7	OK
K	60	1.60	9.9	OK

As in the first test plan, the grinding fineness, density, gloss and glass surface control results are similar in the second test plan.

In conclusion, paint samples prepared using different types of wetting additives were evaluated. Comparing the results of paint sample E from the first test plan reveals that changes in wetting additives lead to a noticeable difference in viscosity, gloss, and vis-cosity increase rates.

Effect of amount of wetting agent (Third test plan results)

Table12. Solid Matter and Hardness results in the third test plan

Calcite Samples	Solid Matter Control 1h 120°C	Hardness Test with Persoz 90µ Applicator and Glass Surface, 50°C 2h
E	77.03	118
L	77.01	110
K	77.07	116

The solids matter results in the third test plan are similar to those in the other two test plans. Hardness results are similar.

Table13. Viscosity results of paint samples in the third test plan

Calcite Samples	Viscosity Control (initial control) DIN6, 20°C 125-150	Viscosity Control (After 2 weeks) DIN6, 20°C 125-150	Viscosity Control (After 4 weeks) DIN6, 20°C 125-150
E	81	82	93
L	72	73	85
K	71	72	79

In the third test plan, the viscosity results were significantly lower than in the other two test plans. When pigment surfaces are not sufficiently wetted, aggregates and agglomerates form due to Van der Waals attraction between particles. These large clumps impede flow in the system, increase viscosity, and increase mechanical energy requirements. As the wetting agent/dispersant increases, pigment surfaces are better coated, and these clumps are separated. Consequently, smaller particles are formed, flow is facilitated, and viscosity decreases. Therefore, the low viscosity in this test plan is in line with theory.

Table14. Percentage of viscosity increase of paint samples in the third test plan

Calcite Samples	Percentage of viscosity increase between the first measurement and the measurement after 2 weeks (%)	Percentage of viscosity increase between the first measurement and the measurement after 4 weeks (%)
E	1.2	14.8
L	1.4	18.1
K	1.4	11.3

Although the time-dependent viscosity increase rate is similar to the numerical val-ues in the second test plan, the viscosity measurement results after four weeks are much lower than those in the other two test plans. Because the amount of wetting agent is high, the particles in the product are abundantly surrounded by wetting agent, and floc-culation tendency is low.

Table15. Grinding Fineness, Density, Brightness and Paint control on glass surface with 120µ applicator application results of paint samples in the third test plan

Calcite Samples	Grinding Fineness (µ)	Density (g/cm3)	Brightness 60° (Gloss)	Paint control on glass surface with 120µ applicator application
E	60	1.57	13.0	OK
L	60	1.57	13.3	OK
K	60	1.58	147	OK

As in the first test plan, the grinding fineness, density, gloss and glass surface control results are similar in the third test plan. In this test plan, gloss results are higher than in the other two test plans. The primary reason for the increased gloss of the paint as the wetting

agent amount is the improved pigment and filler dispersion quality and the re-duced surface roughness.

In conclusion, in the third test plan, the amount of wetting agent selected in the sec-ond test plan was increased to evaluate its effect on the overall paint system. The results showed a significant decrease in the viscosity of the paint samples. A noticeable in-crease in gloss results was observed with the increase in the wetting agent amount. The rate of increase in viscosity of the paint samples was found to be more stable and less pronounced compared to the other two test plans. Solids, density, and crushing fineness were similar to the results in the other test plan.

4 Conclusions

This study investigated the effects of different calcite types on paint performance and behavior. Several controls were conducted based on studies conducted by producing paint formulations from calcite samples. It was observed that parameters such as vis-cosity, gloss, hardness, and viscosity increase over time were affected by calcite differ-ences. However, no visible differences were observed in grinding fineness, density, or glass surface. Calcite generally has the effect of increasing the hardness of the paint, but this effect depends on grain size and purity. Differences in viscosity between paint samples can be explained by differences in particle size and morphology of the calcite used in the paint. The increase in viscosity over time can be explained by the agglom-eration of particles within the paint due to physical forces, leading to an increase in viscosity.

Based on research using paint formulas made from calcite samples, a number of controls were carried out. Calcite variations were found to have an impact on metrics such viscosity, gloss, hardness, and growth of viscosity over time. Nevertheless, there were no discernible variations in glass surface, density, or grinding fineness. Calcite increases the paint's hardness; nevertheless, this effect is dependent on the size and purity of the grain. Variations in the morphology and particle size of the calcite used in the paint can account for variations in viscosity between paint samples. The aggregation of particles within the paint as a result of physical forces can account for the increase in viscosity over time. In the findings phase, every study result was discussed. Through-out the whole test plan, the samples' viscosity growth rates were impressive. The cause of this was looked into.

The viscosity of each paint sample increased over time. The theoretical foundations of these phenomena were investigated. One part of the product's composition is alkyd resin. Because they include unsaturated fatty acids, alkyd resins oxidize over time, cre-ating O–O radicals and partially cross-linking molecules that increase their molecular weight. This leads to an increase in viscosity. The second factor is the absorption of resin by calcite. The resin's mobility is restricted by the adsorption of the resin chains onto the filler surface. Viscosity increases when calcite particles and other powdered minerals group together in the product. The third factor is the evolution of the effective solvent ratio and solvent adsorption. When aromatic solvents adsorb onto calcite sur-faces, a solvent-poor environment is created. Additionally, some solvent evaporates when paint is touched. An increase in viscosity is anticipated due to the quantity of vaporized solvent and the solvent adsorption by the fillers. This illustrates how calcite increases paint's viscosity. Particle interaction in solvent-based paint results in a semi-easy-flowing particle network due to reduced free solvent volume and solvent/resin adsorption. When calcite particles are scattered near one another, they can create phys-ical networks or weak agglomerations. By preventing solvent flow and limiting the free movement of resin chains, this structure raises viscosity.

Acknowledgements

We also thank Kansai Altan Boya Sanayi A.Ş company for providing infrastructure support.

References

[1]. Marshall, D. J., Hall, R., Anderson, M. R., Malik, O. A., Ahmed, M. U., Mansoob, M., ... & Yasin, H. SCIENTIA BRUNEIANA.

[2]. Sun, J., Wu, Z., Cheng, H., Zhang, Z., & Frost, R. L. (2014). A Raman spectroscopic comparison of calcite and dolomite. Spectrochimica Acta Part A: Molecular and Biomolecular Spectroscop y, 117, 158-162.

[3]. Kartal, İ., Boztoprak, Y., & Selimoğlu, H. Kalsit ve Çam Talaşi Dolgulu Polyester Matrisli Kompozitin Aşınma Özelliklerinin İncelenmesi. *Uludağ Üniversitesi Mühendislik Fakültesi Dergisi*, *29*(2), 583-594.

[4]. Ersoy, O., Fidan, S., Köse, H., Güler, D., & Özdöver, Ö. (2021). Effect of calcium carbonate particle size on the scratch resistance of rapid Alkyd-based wood coatings. *Coatings*, *11*(3), 340.

[5]. Karakaş, F., & Çelik, M. S. (2012). Effect of quantity and size distribution of calcite filler on the quality of water borne paints. Progress in organic coatings, 74(3), 555-563.

[6]. Liu, Q., Wang, Q., & Xiang, L. (2008). Influence of poly acrylic acid on the dispersion of calcite nano-particles. Applied surface science, 254(21), 7104-7108.

[7]. Ersoy, O., Güler, D., & Rençberoğlu, M. (2021). Effects of grinding aids used in grinding calcium carbonate (CaCO3) filler on the properties of water-based interior paints. Coatings, 12(1), 44.

[8]. Karakaş, Fatih (2011). Endüstrđyel Hammaddelerin Su Bazli Boyalarda İslev Mekanizması, Doktora Tezi. İstanbul: İstanbul Teknik Üniversitesi

[9]. Tunçgenç, M. (2004). Boya teknolojisine giriş. Akzo Nobel Kemipol AŞ.

[10]. Karakaş, F., & Çelik, M. S. (2013). Mechanism of TiO2 stabilization by low molecular weight

[11]. Ulusoy, U., Çayirli, S., Bayar, G., & Gokcen, H. S. (2023). Comparison of particle shape, surface area, and color properties of the calcite particles ground by stirred and ball mill. Minerals, 13(1), 99.

[12]. Ersoy, O., Fidan, S., Köse, H., Güler, D., & Özdöver, Ö. (2021). Effect of calcium carbonate particle size on the scratch resistance of rapid Alkyd-based wood coatings. Coatings, 11(3), 340.

Symposium & Workshops

6th International POLYMERIC composites

CONTRIBUTORS/DESTEKLEYENLER

SPONSORS/SPONSORLAR

İZMİR-TÜRKİYE

www.polymericcomposites.org